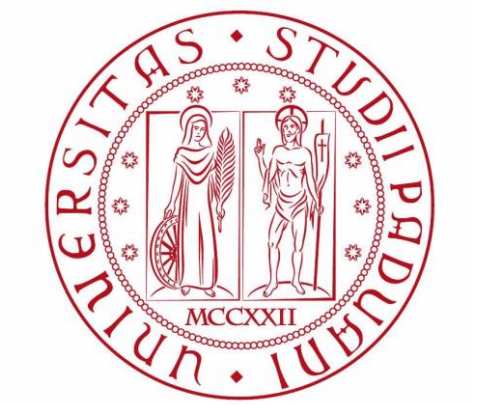

UNIVERSITÀ DEGLI STUDI DI PADOVA

Dipartimento di Geoscienze

Direttore Prof. Cristina Stefani

TESI DI LAUREA MAGISTRALE IN

GEOLOGIA E GEOLOGIA TECNICA

THE ALID VOLCANIC DISTRICT (ERITREA): REMOTE SENSING ANALYSIS AND PRELIMINARY CONCEPTUAL MODEL OF THE GEOTHERMAL RESERVOIR

Relatore: Prof. Antonio Galgaro

Correlatore: Dott. Andrea Ninfo

Laureando: Nicola Pirola

ANNO ACCADEMICO 2014/2015

Index

List of figures

Abstract

The principal aim of this work was to improve the characterization of Mt. Alid geothermal system (eastern Eritrea), considered the most favourable geothermal resource of the country. To conduct a detailed remote sensing analysis, a high resolution digital elevation model has been provided, the new ALOS DEM (courtesy of JAXA). Before its use, it required a validation process, using GCPs and other already validated data, such as SRTM. With the aid of different DEMs, Bing and Google high resolution images and processed Landsat 8 acquisitions, a remote sensing analysis has been conducted, in order to characterise geological, geomorphological and geostructural features of the Alid area and surrounding. Two main structural lineaments have been found: a NNW-SSE normal fault system, strictly related to the regional rift tectonic context, and a NE-SW trend with a dextral strike-slip component, related to the presence of the underlying shallow magma intrusion. The results obtained from the remote sensing approach have revealed that the crossing of the two fault systems caused the ascent of geothermal steam to the surface, since the position of fumarolic vents seems to be closely related. The mapping of geological units has brought the realization of and an updated and more accurate geological map of the Alid geothermal district. A preliminary fieldwork, aimed at validating the remote sensing analysis, was carried out in February 2015 and confirmed, to a first approximation, the validity of the mapping. An analysis on ASTER TIR images has also been conducted, to extract heat anomalies from processed thermal bands and measure the heat contribution due to the presence of surface geothermal manifestations. Normalized temperature has confirmed that thermal anomalies are related with fumaroles and has given us promising results for further detailed studies. An attempt to quantify the potential of the geothermal resource has been made. In cooperation with the IGG-CNR research institute of Florence, a first numerical model of the geothermal reservoir has been realized. Simulation results indicate a possible reservoir temperature of 260-270 °C, a pressure of about 50 bar and a vapour fraction of 0.7. These values are coherent with a dominant steam geothermal reservoir.

Introduction

The development of the energy sector is one of the principal objectives of the Eritrean country. In fact, at present, the electric power generation, mainly based on oil burning plants, is totally dependent on high-cost imported refined petroleum products from Yemen and Sudan.

Energy generation and demand has been growing continuously in the last years, but access to electricity for the population remains low, only 32%. For this reason the Ministry of Energy and Mines, in consultation with the Ministry of National development, created a long-term development program that gives particular attention to the use of alternative energies and the proper utilization of the existing energy resources. The major reforms include an expansion of electrification in rural areas by means of grid enhancing, a promotion of renewable energy technology, energy conservation and efficiency and liberalization of electricity Market and supply of oil products (Habtetsion & Tsighe, 2007; Yohannes, 2015). Since the energy consumption is rising exponentially, new alternatives in terms of energy supply are required in order to satisfy the increasing demand and to reduce the dependence on imported fossil fuels.

Considering the favourable geothermal context affecting the territories of the Eritrean lowlands, there is the concrete possibility to exploit this resource for electric power production and to meet the energy national demand. The East Africa region represents indeed one of the major world geothermal provinces as it hosts an important tectonic context: the East African Rift System (EARS). This structure is characterized by a thin continental crust and defines three main arms: the Red Sea Rift, the Gulf of Aden Rift and the East African Rift. The EARS crosses through several states, including Eritrea, Djibouti, Ethiopia, Kenya up to Mozambique. Estimated geothermal energy resource potential in the EARS is more than 15,000 MWe. Nevertheless, only Kenya and Ethiopia have installed a capacity of about 217 MWe. The other countries, including Eritrea, are only in a preliminary stage of exploration (Hochstein, 1999; Teklemariam, 2012; Omenda, 2013).

As a considerable portion of the State of Eritrea is located within the EARS, it is believed that the country is well endowed with geothermal resources, which can be exploited for energy production purposes. After a preliminary analysis, it seems that the Alid volcanic area is one of the highest geothermal potential areas of Eritrea and one of the most promising sites of the entire East African Rift as well.

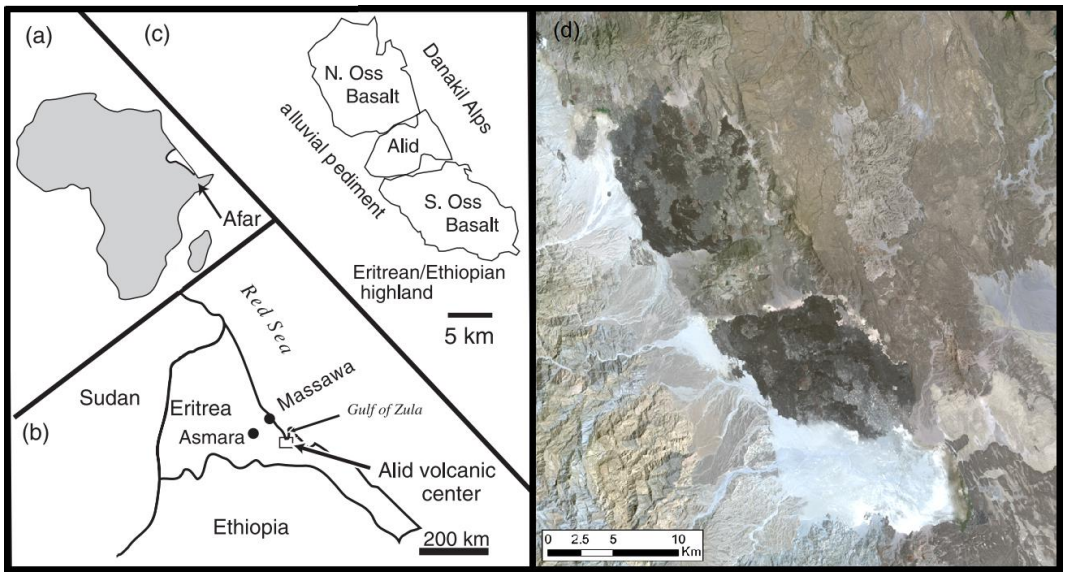

Figure 1. a) Position of Afar triangle and the Eritrean country; b) location of the Alid volcanic district; c) simplified geologic map of the Alid graben; d) Landsat 8 natural colour image of the study area (modified from Lowenstern et al., 2006).

Mt. Alid (700 m a.s.l.) is a volcano-like structure located in the Lowlands region of Eritrea, the northern portion of the Danakil depression (Figure 1). Due to the extensional tectonics, this location is rich in shallow geothermal manifestations, such as fumaroles, hot springs and pools. Previous investigations, including fluid sample geochemistry, suggest the presence of a vapour-dominated system with hydrothermal reservoir temperature between 250 °C and 300 °C (Clynne et al., 1996; Duffield et al., 1996; Lowenstern et al., 1999). Further geophysical studies located a high-resistivity zone at 2500 m b.s.l., on the south-west side of the mountain, which has been interpreted as the main source of geothermal steam (Teklesenbet, 2012; Yohannes, 2010).

Moreover, Alid is relatively close to the two main urbanized areas, where the energy demand is concentrated (90 km south east from Massawa and 130 km from the capital Asmara (Figure 1.b)**.**

This master degree Thesis is focalized on create a create a complete GIS database including digitalized and georeferenced available thematic maps, such as paper geologic maps, structural maps, MT and TEM soundings coordinates and the position of fumarole and thermal pools. With the combined use of DEMs, Landsat 8 data and aerial imagery, the final objective is to produce a detailed and updated geological map.

Another important analysis has been focused on ASTER thermal data, in order to detect shallow heat anomalies and obtain useful information for understanding hydrothermal circulation system that feeds fumaroles and thermal pools.

Besides the remote sensing activity, this Thesis aims to obtain a numerical model of the Alid geothermal system. Starting from all the data collected from the previous studies, such as geophysical campaigns and geochemical analysis, the natural-state condition of the geothermal reservoir have been simulate, to obtain information about temperature, pressure and steam fraction.

1. The East African Rift System

The East African rift system (EARS) is an intra-continental magmatic ridge system, assumed to mark the incipient plate boundary between the Somali and Nubian micro-plates and linked to the Afar-Red Sea-Gulf of Aden rift systems. As explained later in this chapter, it records all the different stages of evolution from rift initiation to break-up and embryonic oceanic spreading (Ebinger, 2005).

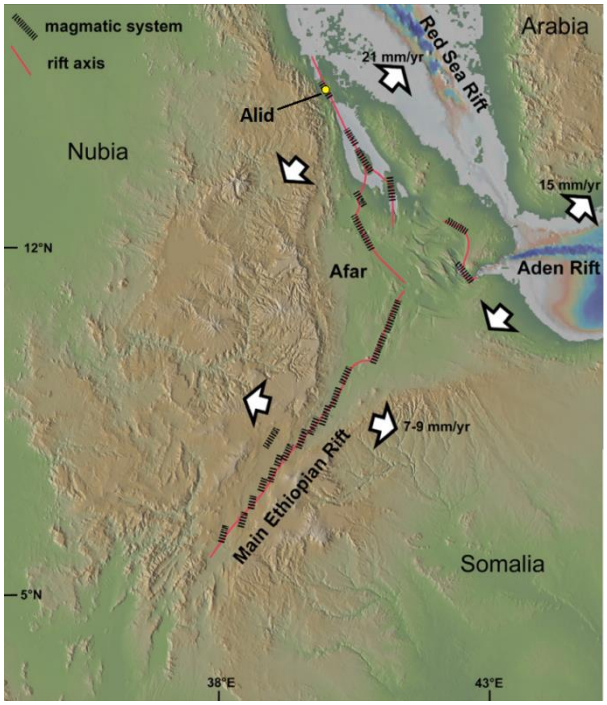

Figure 2. Main structures of the northern part of EARS: the white arrows show the spreading directions of the three main arms, with the relative spreading rate in mm/y.

1.1. Physiography

The EARS shows up at the surface as a series of several thousand km long aligned successions of adjacent individual tectonic basins (rift valleys), separated from each other by relative shoals and generally bordered by uplifted shoulders. Each basin is controlled by faults and forms a subsiding graben or trough, hundreds of kilometers long, a few tens kilometers wide, empty or filled with sediments and/or volcanic rocks. These successions of graben basins are generally bordered on two sides by a high relief, comprising almost continuous parallel mountain lines and plateaus, and sometimes volcanic massifs (Chorowicz, 2005).

The rift valleys form two main lines, the eastern and western branches of the EARS. A third, southeastern branch is in the Mozambique Channel. The eastern branch runs over a distance of 2200 km, from the Afar triangle in the north ending in the basins of the North-Tanzanian divergence in the south. The western branch runs over a distance of 2100 km from Lake Albert (Mobutu) in the north, to Lake Malawi (Nyasa) in the south

1.2. Tectonics

The morphotectonics of the EARS are under control of divergent movements, inducing localized extensional strain in the continental lithosphere. The brittle crust has reacted by faulting and subsidence, forming elongate, narrow rifts, while the lithospheric mantle is subjected to sharply defined ductile thinning, inducing the ascent of asthenospheric mantle.

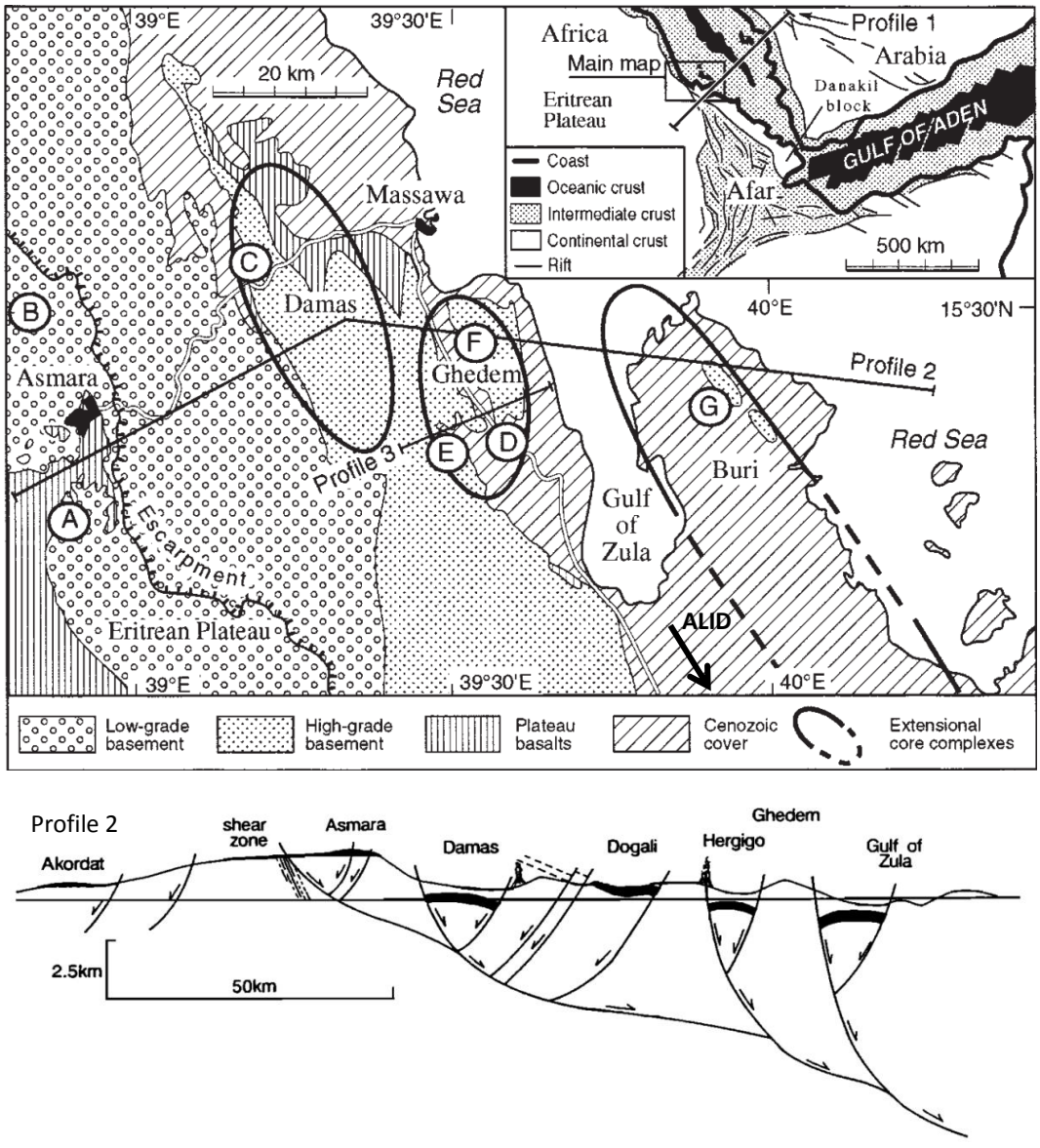

Figure 3. Simplified structural map and west-to-east sketch cross-section from Asmara to Gulf of Zula (Eritrea). Solid areas are laterite plus basalt cover.

The most characteristic features in the rift system are these narrow elongate zones of thinned lithosphere related to deep intrusions of asthenosphere in the upper mantle. These structures are expressed on the surface by thermal uplift of shoulders. On the surface, the main tectonic features are normal faults, but there are strike-slip, oblique-slip and sometimes reverse faults. Extension produces widespread open fractures, comprising tension gashes. Most of the fractures are syn-depositional and volcanism, when it occurs, is closely related to the tectonics.

When the vertical throw component is dominant, the faults are considered to be normal, generally are interpreted to be listric (Bosworth, 1985; Gibbs, 1990) and abruptly connected in depth with low-angle detachment levels (Figure 3). The largest faults are along one border of the graben basin and they are tens of km in length and have several km of vertical throw. These faults dip roughly 65° at the surface, are generally curved in plan view, penetrate the middle-lower crust and connect with the low-angle ductile–fragile transition zone at depth of 20–30 km.

1.3. Seismicity

The analysis of seismic data suggests that the East African rift system is a zone of diffuse shallow earthquakes. Seismicity occurs throughout the depth range 0–30 km and most earthquake hypocentres are located at a depth of 8–16 km, which coincides with the top of the middle-lower crustal extensive mafic intrusions. Hypocentre depths also increase with increasing distance from major volcanoes (Figure 4).

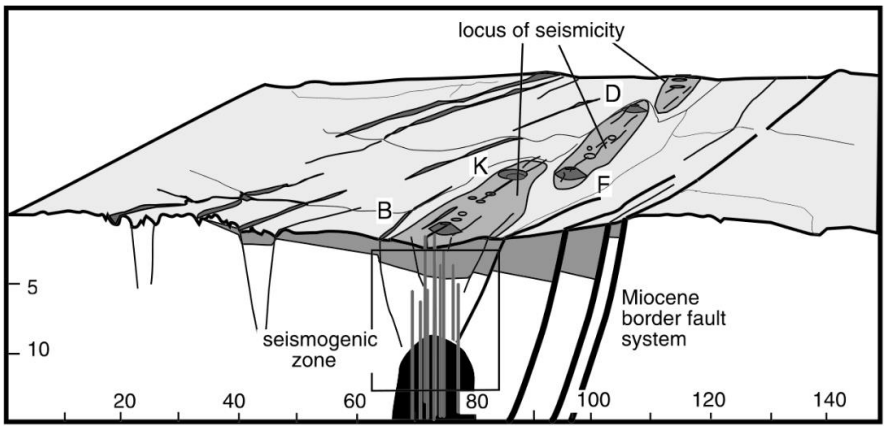

Figure 4. Cartoon sketch of the rift, showing the localization of seismicity in concomitance with magmatic intrusions (Keir et al. 2006).

The Western Rift is more active seismically than the Eastern Rift; while the epicentres are shallow in Afar and deeper in the southern part of the rift system. This seismic activity is usually represented by small to intermediate size events and focal mechanism studies show dominantly normal faulting, as shown in Figure 5 (Kebede & Kulhanek, 1992; Calais et al., 2008; Corti, 2009). Historical records spanning the past 150 years show that large magnitude earthquakes (over MN 6) are rare throughout the rift, although seismic analysis suggests a maximal expected magnitude of ~7, with a return period of about 80 years (Horsfetter and Beyth, 2003).

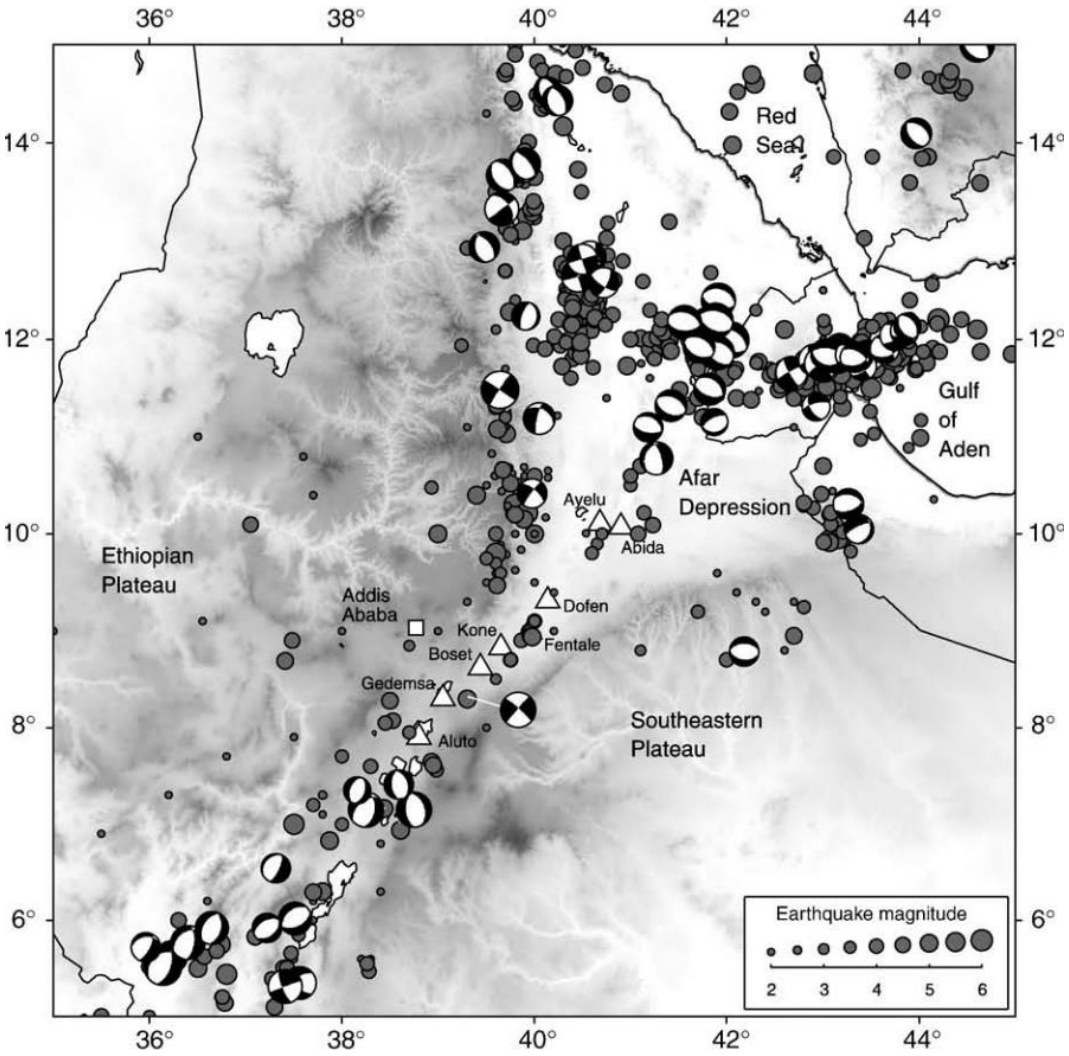

Figure 5. Earthquake distribution in the Afar Triangle and in the Ethiopian rift, from October 2001 to January 2003, and associated focal mechanisms (Corti, 2009).

Despite the widespread seismic activity, most of the extensional deformation (about 50%) seems to be accommodated aseismically (Hofstetter and Beyth, 2003). Data show that the seismic activity in the Northern and Central part of the EARS is typically localised within spreading segments, pointing to a close correlation between seismicity and alignments of Quaternary volcano-tectonic zones. However, major boundary faults are largely aseismic, although cluster of events may characterise the border escarpments in structurally complex region that still experiences some strain (Keir et al., 2006).

1.4. Volcanism

Cenozoic volcanism in the EARS is widespread in the north—especially eastern branch, but sparse in the south. Abundant volcanism in Northeast Africa is related to plume occurrence (Schilling, 1973; Schilling et al., 1992; Keller et al., 1994). Generally, volcanoes are rooted on open fractures such as tension joints, tail-cracks or tensional releasing bends. Magmas range from alkaline to hyperalkaline, and typically evolved from continental tholeiites rich in incompatible elements, through alkalic products to transitional magmas relatively low in incompatible elements (Baker et al., 1972).

Magmatism is linked with asthenospheric ascent, either under regional plume conditions, or local rift-related lithospheric mantle thinning. During lithospheric extension, largely related to dyking, diapiric ascent of a lherzolitic asthenospheric wedge leads to the generation of basaltic melts. Partial melting may occur at all levels within the diapir, producing magmas that are tholeiitic at shallow level, transitional at intermediate levels and alkaline at deeper levels (Kampunzu & Lubala, 1991; Mohr, 1992).

1.5. Rift evolution

The standard model for active rift formation involves lithospheric extension accompanied by upwelling of the underlying asthenospheric mantle. Decompression of the asthenosphere results in large volumes of magma formation. Further brittle extension of the crust results in down faulting and

formation of the graben. In the case of the EARS, extensions is more active in the north being more than 2cm/year in the Red Sea – Gulf of Aden, 1 mm/year in the Main Ethiopian Rift, and less than 1mm/year in the Kenya Rift and southwards. In response to the increased extension in the EARS, the Moho is at between 5 and 35 km along the axis of the rift (Omenda, 2013).

First rift manifestation is the formation of open fractures at 30 Ma in the Afar and Ethiopian plateau, due to hot spot activity, responsible for the emission of trap lava flows (Hoffman et al., 1997; Mège and Korme, 2004), accompanied by the initiation of three converging graben structures, forming a triple junction at lake Tana (Chorowicz et al., 1998). Rifting in the Gulf of Aden began at 29.9–28.7 Ma, and in the southernmost Red Sea at 27.5-23 Ma (Hughes et al., 1991). The Afar depression seems to have formed later in the Miocene. At 20 Ma, first volcanism appeared far more to the south at the future triple junction between the northern Kenyan, central Kenyan and Nyanza rifts (Pickford, 1982; Fitch et al., 1985). The main Ethiopian rift, located between these two nucleations, commenced after 11 Ma, later than early Miocene volcanic events in the Turkana region (Wolfenden et al., 2004).

The various rift segments are at different evolutionary stages, depending on the age of rift initiation and distance to the Eulerian pole. For a given age, length of normal faults, width of rift basins, relief of the uplifted rift flanks vary depending not on the age but on the stage of a rift segment. Different authors have been defined the stages of rift evolution (Chorowicz et al., 1987; Mondeguer et al., 1989; Hayward & Ebinger, 1996), which can be summarized as following:

a. Pre-rift stages (Figure 6.a) are characterized by the dominance of a horizontal distribution of earthquake epicentres movements, according to Chorowicz et al. (1987), and in the youngest propagating southern EARS the focal mechanisms of earthquakes are distinctly strike slip, responsible for high energy seismicity, formation of en-echelon tension gashes and dense distribution of small-throw strike-slip and oblique-slip faults, with a strike-slip stress-field. If volcanism occurs, it is mainly tholeiitic hyperalkaline. The morphology is that of topographic depressions characterized by swamps and shallow lakes, without

apparent uplifted shoulders. There is not yet a true graben, and the asthenospheric intrusions are discrete.

b. Initial-rift stage (Figure 6.b) is related to noticeable subsident and divergent movements, with frequent earthquakes, lesser fault density, mostly extensional oblique-slip faults, and tensional stress field. Volcanism, if existing, comprises contaminated alkaline magma. The basins are well defined with roll-over geometry in cross-section, pronounced shoulders, forming halfgraben structures. They are some tens of kilometers in length, 30-40 km in width, and separate from each other by transform, transfer or accommodation zones forming basement highs. The asthenospheric intrusions in the lithosphere are pronounced, causing negative Bouguer anomalies due to low density of the mantle plumes (Simiyu & Keller, 1997).

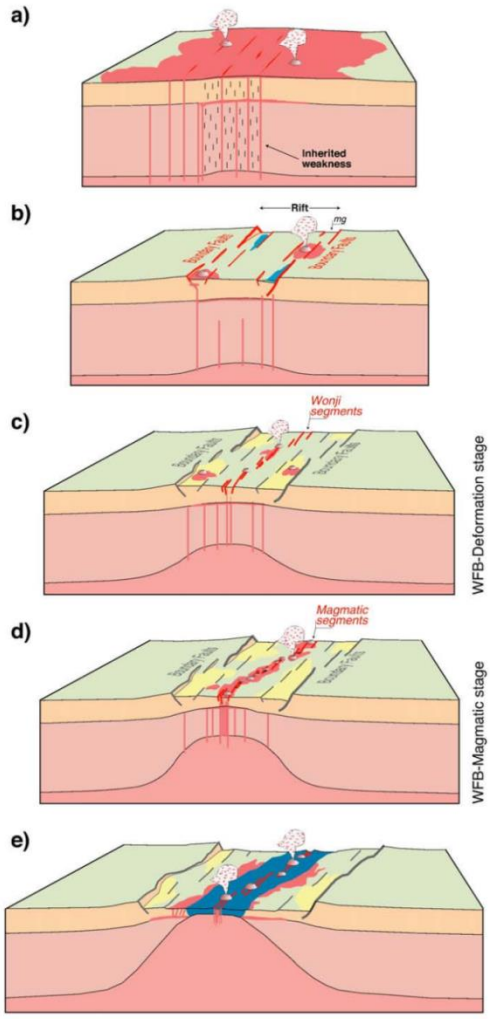

Figure 6. Schematic model of EARS evolution stages of the EARS evolution, from incipient rift to initial crust breakup (Modified after Ebinger, 2005).

c. Typical rift stage (Figure 6.c) has a very well defined rift valley and thick graben deposits, with frequent low-energy earthquakes. Tectonics is dominated by the effects of normal faulting, but most of the deformation is concentrated along the major faults bordering one side of each graben. Regional extensional movements are combined with local tension related to gravity induced deformation. The former shoals are buried; the originally separated individual basins now connected forming longer basins, often occupied by a great

lake. The shoulders are high, the negative Bouguer anomaly is steep and narrow, due to asthenospheric intrusion.

d. Advanced-rift stage (Figure 6.d) differentiates from the preceding by a larger regional negative Bouguer anomaly, with a contrasting narrow positive gravity anomaly in the middle, indicating the intrusion of dense material into the crust and considered as the first apparition of oceanic-type material (Baker and Wohlenberg, 1971; Simiyu & Keller, 1997). There are many large tension fractures giving way to differentiated alkaline volcanism. This situation essentially corresponds to the main Ethiopian rift.

e. Oceanic rift stage (Figure 6.e) is that of the Afar, with oceanic crust production and seafloor spreading. The tectonically and magmatically thinned lithosphere ruptures in the heavily intruded zones and new oceanic lithosphere is created. The thick piles of lavas in the magmatic segments load the weak plate, flexing it towards the new ocean basin to form seaward-dipping lavas (Ebinger, 2005).

1.6. Geothermal resources

Geothermal activity in the rift is manifested by the occurrences of Quaternary volcanoes, hot springs, fumaroles, boiling pools, hot and steaming grounds, geysers and sulphur deposits and is closely connected with magmatism. The association is related to the shallow hot magma bodies under the massifs, which are the heat sources.

In the Afar rift, where these manifestations are abundant and stronger, the crust is only 5 km thick, so extensive manifestations and high heat flux is due

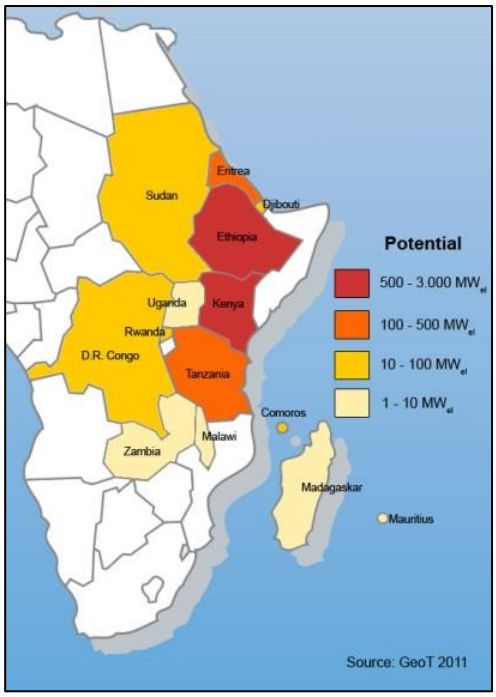

Figure 7. Geothermal potential of the East-African Rift Valley (http://www.geo-t.de/en/project-development/worldwide).

to a combination of mantle heat and magma bodies occurring at shallow depths. In the less magmatic western branch of the rift, where the activity is subdued and consists mainly on hot springs and fumaroles, heat sources could be combination of buried pluton and high heat flux associated with a thinned crust.

Detailed and reconnaissance studies of geothermal potential in Eastern Africa, based on the evaluation of local heat flux, indicates that the region has potential of over 15,000 MWe (Figure 7). Despite this potential, only Kenya and Ethiopia have active geothermal power plants of 209 MWe and 7.2 MWe, respectively (Omenda, 2013).

Precipitation rates are less than 0.2 mm/year in the low parts of northern Ethiopia, Eritrea, and Djibouti. Significant water infiltration occurs only over the flanks and shoulders of the rift at altitudes higher than 1700 m a.s.l.. This particular arid to semi-arid climate of the rift favors the development of two types of hydrothermal systems, namely steaming ground and advective. Steaming ground systems are associated with older volcanic dome complexes where heat transfers at shallow levels dominantly by steam. In advective systems, heat is swept from hot rocks within the rift by deeply penetrating groundwater (of meteoric origin) and the heat transfers to the surface by hot water mass transport only. Leaching of saline sediments may lead to the development of surface phenomena like the formation of thermal brine lakes (Hochstein, 1999).

There are at least 54 major geothermal systems along the 2000 km long eastern branch of the African Rift system. Heat discharged by each one of the 30 major hydrothermal systems is between 10 and 400 MWth, with the largest transfer occuring at Olkaria (Kenya).

In **Djibouti**, areas of strong manifestations are located within the Asal and Hanle rifts in the Afar Depression (Jalludin, 2010). According to a recent study conducted by Houssein and Axelsson et al. (2010), the geothermal potential in Djibouti is between 230-860 MWe.

In 1973 the United Nations Development Programme (UNDP) identified potentially significant exploitable geothermal resources in **Eritrea**. In 1995, with help of United States Geological Survey (USGS), the Alid geothermal district was

selected as the most promising area and detailed investigations have been suggested (Duffield et al., 1996). A detailed discussion about Alid's geothermal potential will be presented in Chapter 3.

In 1969 **Ethiopia** started a long-term geothermal exploration programme. Sixteen areas have been judged to have potential for high enthalpy geothermal power plants so far. In the mid-1980s exploration drilling were carried out at the Aluto-Langano geothermal field. Eight deep exploratory wells were drilled and four of them were found to be productive with a maximum geothermal reservoir temperature of about 350º C. During the early 1990s exploration drilling was also carried out at Tendaho and six wells confirmed the existence of a high temperature (270º C) reservoir. Finally, in 1998, the first 7.2 MWe pilot power plant was built in the Aluto-Langano field.

Geothermal manifestations in the **Kenya** rift include fumaroles, hot springs, spouting springs, hot and altered grounds and sulphur deposits. Fumaroles commonly occur on the mountains while hot springs and geysers are common on the lowlands. Sulphur deposits have been observed at several geothermal areas including Olkaria, Paka and Barrier volcanoes where it is indicative of the presence of a degassing magma body at depth. Olkaria has been chosen for electricity generation (130 MWe) while a pilot power plant has been built in Eburru (2.5 MWe). Both the Olkaria and Eburru geothermal systems are volcano-hosted resources, in which the heat source is associated with hot intrusive bodies under the volcanic complexes. Detailed investigations recently concluded in Menengai, Korosi, Pakaand Lakes Baringo and Bogoria geothermal prospects reveal the existence of possible high-potential geothermal systems (Omenda & Simiyu, 2015). It is estimated that over 3,000 MWe can be generated from Kenya geothermal systems (Omenda, 2013).

Geothermal exploration in **Tanzania** was carried out between 1976 and 1979. Reconnaissance studies for surface exploration were carried out in the north (near Arusha, Lake Natron, Lake Manyara and Maji Moto) and in the south (Mbeya region). Geothermal work in all locations in Tanzania is at the surface exploration stage. Two potential target areas for geothermal exploration are the Arusha

region, the Mbeya region and Luhoi location. Exploration campaigns conducted so far in Luhoi indicates the existence of a possible geothermal system with reservoir temperature greater than 200°C (Mnjokava et al, 2015).

In **Uganda,** geothermal activity is concentrated in the western rift valley. Geothermal manifestations in the form of fumaroles and hot springs occur along some of the border faults of the rift valley and within the volcanic fields. Fault controlled manifestations occur at Buranga as well as at Kibiro. Hot springs also occur in the Katwe-Kikorongo and Virunga volcanic fields where they are associated with the young volcanoes (Bahati & Natukunda, 2008). Reconnaissance surveys have been carried out on geothermal areas of Uganda since 1935 when the first documentation of hot springs was made (Bahati and Tuhumwire, 2002).

Geothermal activity in **Zambia** and southern **Democratic Republic of the Congo** occurs within the south-western rift. The geothermal manifestations occur at Kapisya that discharge 85 °C hot water. Other springs occur at Chinyunyu (60 °C) near Lusaka. A pilot geothermal power plant (200 KW) was built by the Italian government in 1987 nearby Kapisya hot springs. The plant was installed on the basis of limited exploration work, but it never became operational. A detailed scientific investigations was subsequently carried out both at Kapisya and Chinyunyu, which revealed that the geothermal systems could generate up to 2MWe using binary technology (Omenda, 2013).

2. Geology of the Study Area

Due to its extreme climate and the troubled political history of the Eritrean country, a detailed geological survey of the subsoil of the study area has not been done yet. Two exploration field trips have been done until now by the Italian explorer Marini (1901-1902) and by Duffield et al. (1996) of the USGS.

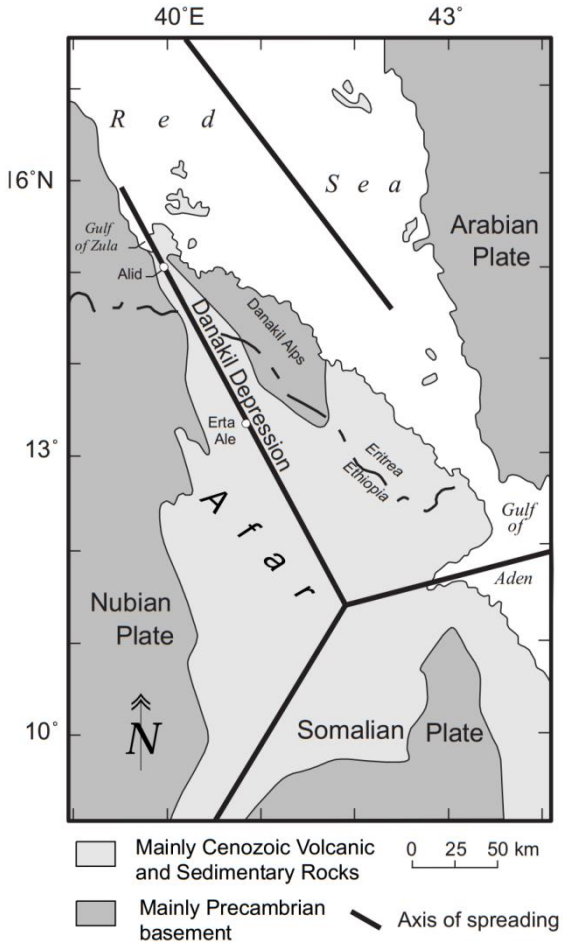

Figure 8. Simplified tectonic map of the Afar region. The Danakil depression, in which the Alid mountain is located, is strictly related to the Red Sea crustal extension (modified from Barberi & Vallet, 1977).

2.1. Regional tectonic setting

The Alid area lies right in the northern part of the Danakil depression, East African Rift, a zone characterized by crustal extension mechanisms related to the Afar tectonic triple junction (see figure 2.1), where three spreading ridges connect three divergent tectonic plates: the Nubian plate, the Somalian Plate and the Arabian Plate. The Danakil depression is a segment of the spreading system that has opened from the Red Sea (Barberi & Vallet, 1977).

The study area is located between the Nubian plate and the Danakil Alps (Figure 8) and it is bounded by two NW-SE deep-rooted normal faults, forming a depressed area which locally is named "Alid graben". The east-dipping western normal fault, which forms the Red Sea Escarpment, rises up from the graben up to 2500 m; the eastern topographic and structural boundary is a west-dipping, steep and 300 m high fault escarpment (Drury et al., 1994; Clynne et al., 1996).

A once-continuous basement terrain of Precambrian granitic and metamorphic crust was rifted apart when the Arabian Peninsula separated from Africa to form the Red Sea. Parts of this basement complex are widely exposed in a belt near and parallel to the Red Sea coast of the Arabian Peninsula and in the Eritrean and Ethiopian highlands southwest and adjacent to the Danakil Depression. Precambrian rocks also crop out in the Danakil Alps. (Duffield et al, 1996).

Crustal spreading along the Danakil Depression began in early Miocene, and soon thereafter a sequence of complexly interbedded volcanic, alluvial, shallow marine and evaporitic deposits began to accumulate along what evolved into the present graben. Quaternary volcanic deposits exposed in the depression today are mostly basaltic lava flows erupted from north-northwest-trending fissures oriented perpendicular to the direction of crustal spreading. Locally, basaltic shield volcanoes grew along the axis of the Depression. An example is the Erta Ale shield with its active summit lava lake, about 125 kilometers south-southeast of Alid. Elsewhere centers of silicic volcanism, such as Alid, formed within a regional background of pervasively basaltic volcanism (Duffield et al., 1996).

Due to the high rate of subsidence, the floor of the Danakil Depression has continued to drop and locally, where sedimentation rate is low or volcanism is scarce, it is below sea level. For example, the height of the salty plain between Alid and Erta Ale is 120 m b.s.l. and Giuletti Lake, just beyond Erta Ale, is about 70 m b.s.l. (Barberi et al., 1970).

2.2. Geology of Mount Alid and surrounding

Although previously described as a stratovolcano with a summit caldera (Barberi et al., 1970; C.N.R.-C.N.R.S, 1973), Alid is actually an elliptical structural dome (Figure 9), which rises 700 m above quaternary basalts that laps unconformably against the northern and southern flanks of the mountain (about 904 m a.s.l.). The summit region, an area measuring about 3 km by 2 km, is actually a huge collapsed zone about 200 m deep, formed after an explosive eruption.

The major axis of the mountain is 7 km, elongated in an ENE-WSW direction, perpendicular to the trend of the rift. The minor axis is about 5 km long, parallel to the graben (Clynne et al., 1996). The dome is most likely the result of a shallow intrusion of rhyolitic magma, as described in more detail in the next paragraph. The following is a brief description of the main rock types of the Alid area.

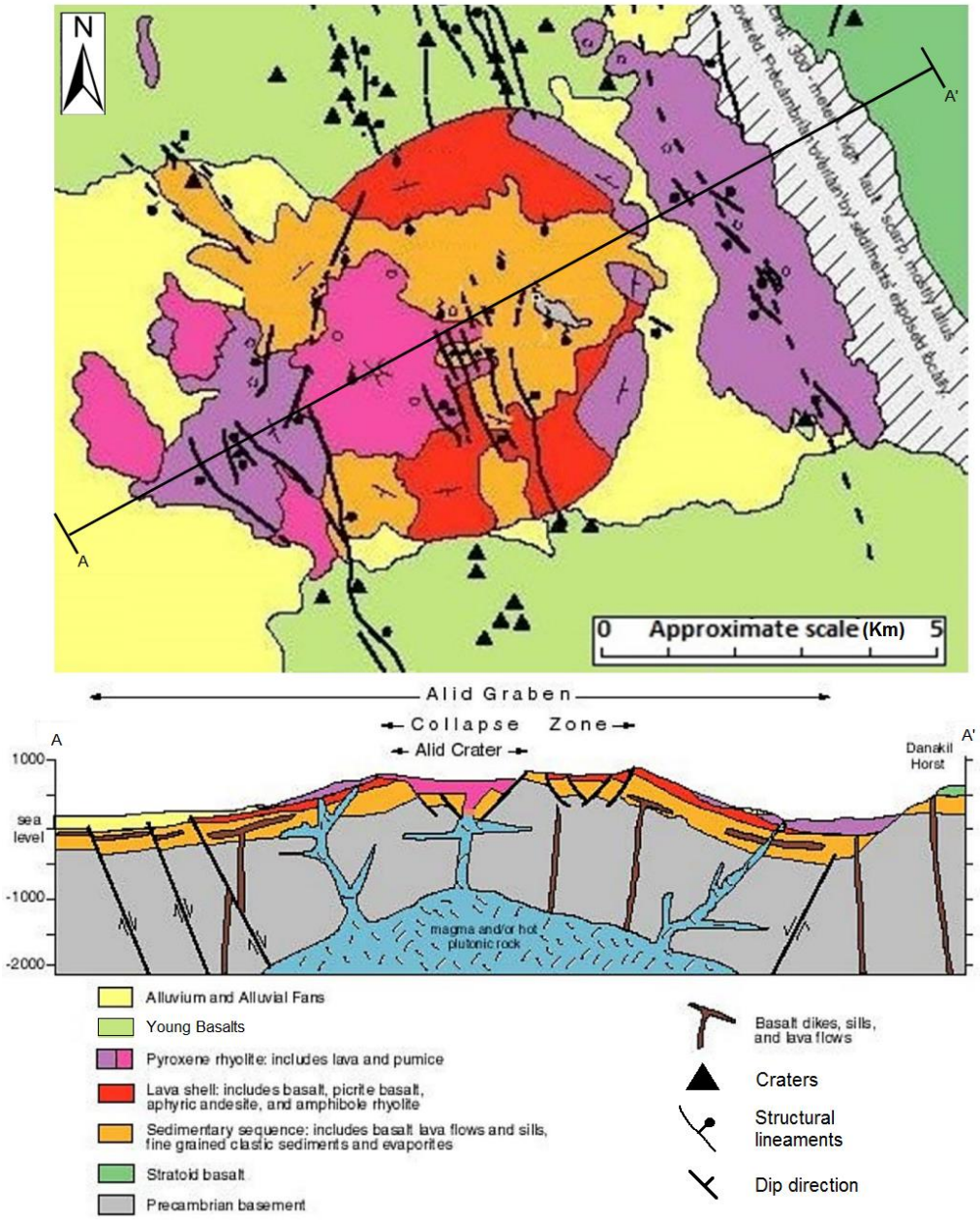

Figure 9. Simplified geologic map and schematic cross section of the Alid dome (modified from Duffield et al, 1996).

The oldest rock unit outcropping in the Alid graben is the **Precambrian Basement**, an inlier of quartz-muscovite schist and locally kyanite schist recognized for the first time by Dainelli and Marinelli (1912). It can be found in the Ilegedi thermal area, where intermittent streams have eroded overlying rocks (Figure 10), and locally at the base of the eastern fault scarp that forms the east side of the graben. The rock is cut by frequent aplite and amphibolite dikes, but also more recent (Tertiary?), nonamphibolitized mafic dikes are present in the schists.

Figure 10. The Ilegedi thermal pool outcropping in the altered Precambrian basement (Gersman, 2005).

On the top of the eastern horst of the Alid graben outcrops an extensive sequence of basalts lava, related to the **stratoid basalts** series of the Afar triangle (C.N.R.-C.N.R.S., 1973). Small remnants of the same kind of lavas are found a few kilometers to the northwest of Alid, interpreted as a faulted block partly buried by old alluvial fan deposits. Subaerial basalt flows in the upper part of the Sedimentary Sequence (see next) may be stratigraphically equivalent to stratoid basalt. Reported K-Ar ages for stratoid basalts, in the northwest sector of the Afar

region, ranges from about 24 Ma to 0.4 Ma. Near Alid, they may be about 1.2 Ma (Barberi and others, 1972; Zumbo and others, 1995).

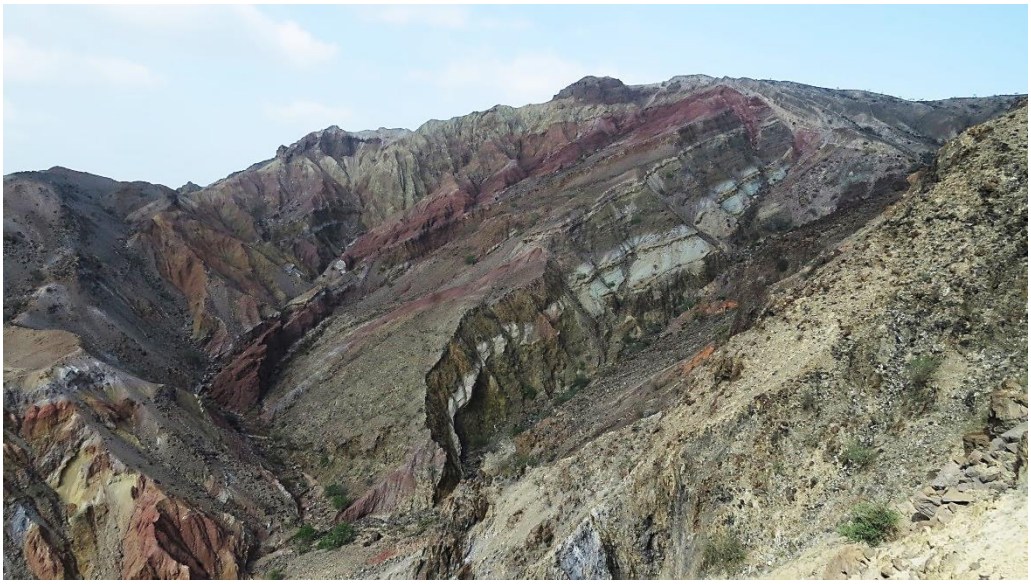

Figure 11. An outcrop of sedimentary sequence on the north-western flank of the mountain (source: Ghinassi, 2015).

An intercalated volcanic and sedimentary rock series unconformably overlies the Precambrian basement, the so-called **Sedimentary Sequence** (Figure 11) identified by Duffield et al. (1996). These rocks are exposed all over the upper part of Alid dome, on the north western side and on the southern flank of the mountain. The Sedimentary Sequence consists in three main rock associations. The older one is formed by pillow basalts, hyaloclastite and minor submarine debris flows; the intermediate part is made by thin-bedded, fine-grained shallow marine sandstone ; the most recent association is formed by subaerial basalt, interbedded tephra and aeolian sand deposits. On the lower flanks of the dome, strata dip steeply, about 65°, decreasing to about 20° in the upper part. All dips are outward radial and they are not primary, but due the uplift caused by a shallow magmatic intrusion. Instead, in the collapsed summit area, the Sedimentary sSquence displays considerable internal deformation: landslide blocks, small faults, block rotation and folding. The combination of sedimentary structures, marine fossils, and evaporites suggests that the original depositional environments

probably ranged from shallow subtidal through intertidal to the supratidal facies. The age of these deposits probably ranges of 200,000 to 300,000 years old: since basaltic rocks within the Sedimentary Sequence contains considerable non-radiogenic argon, it is not possible at the time to evaluate a better constrained age.

The outermost flanks of the dome consist of several tens of meters of basalt flows, picrite, aphyric andesite up to amphibole-bearing rhyolite flows and necks, forming a rock unit named **Lava Shell** (Figure 12). Flows lap conformably over the Sedimentary Sequence and low viscosity of basaltic magma precludes the possibility that these mafic lava flows were emplaced in their present steeply dipping orientations. Thus, the present steep dips of the rocks on the flanks of Alid dome indicate that doming occurred after the mafic Lava Shell flows had been emplaced. It is believed that the eruption of rhyolite began just before, or concurrent with, the initial growth of Alid structural dome. Radiometric dating made on a sample of Lava Shell basalt gave a fairly accurate age of 36,000 years. The stratigraphically oldest part of the Lava Shell yielded an age of about 212,000 years (Duffield et al., 1996).

Figure 12. An outcrop of the Lava Shell formation, in which the different rock composition is evident (source: Ghinassi, 2015).

Pyroxene rhyolite deposits are present in four different locations (Figure 13 and 14). It crops out in the eastern and the western flank of the mountain, along the base the large fault scarp that forms the eastern structural boundary of the graben, and, with a single lava flow which postdates the pumice deposits (described next), in the collapsed summit. All three groups of rhyolites are very sparsely porphyritic with 0.5 to 1 mm phenocrysts of alkali feldspar and less abundant clinopyroxene. Rhyolite lavas seem have the same age and they were formed during the first stages of the dome lifting: as a matter of fact, they appear slightly tilted. The estimated ages of these deposits are 18,000, 29,000, and 34,000 years old, respectively for the western, eastern and fault-scarp rhyolites (Duffield et al., 1996).

Figure 13. Flow banding in a rhyolite deposit (source: Ghinassi, 2015).

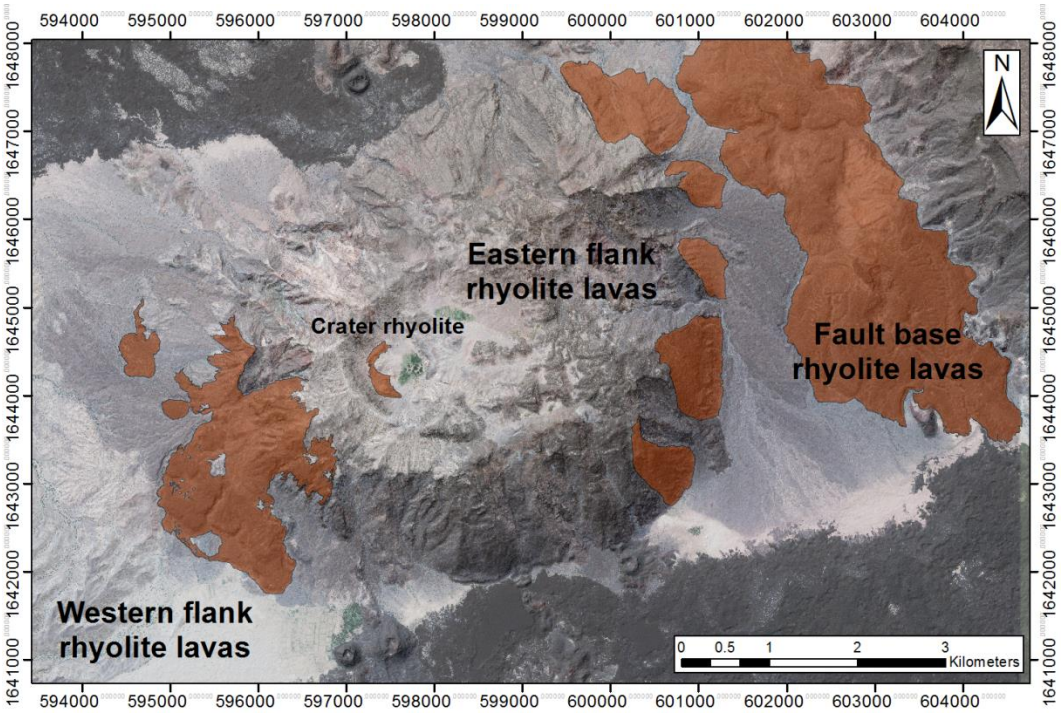

Figure 14. Satellite image of the Alid, in which the four different deposits of rhyolitic lava are highlighted.

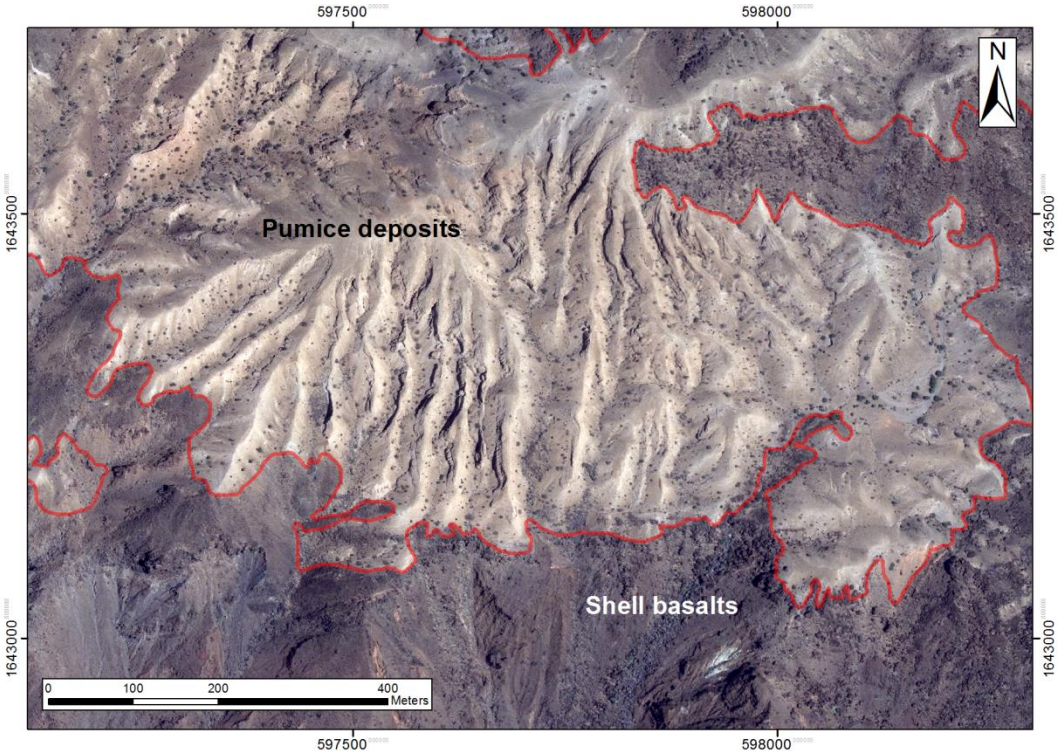

Figure 15. Bing image in which pumice deposit draping the crest of Mt Alid's crater have been bordered in red.

Pyroxene rhyolite pumice overlies the previous described unit (Figure 15). These effusions erupted during the formation of the Alid crater and emplaced as fallout (proximal) or pyroclastic flows (distal). This pyroclastic unit is the product of the youngest silicic volcanism occurred in the area and it is probably the best unit for the evaluation of the magmatic heat source which feeds the hydrothermal system. Pumice contains moderately abundant phenocrysts of alkali feldspar, less abundand clinopyroxene phenocrysts and sparse small quartz phenocrysts. A variety of xenoliths are also present in the pumice deposits (Figure 16), including fragments of amphibole rhyolite, picrite, but also quartz-muscovite and kyanite schists coming from the Precambrian basement. Granite blocks, up to 1 meter in size, of a medium-grained quartz-anorthoclase-clinopyroxene with a granophyric texture and miarolitic cavities are present as lithic fragments in the upper part of the pumice section. They are compositionally and isotopically nearly identical to its host rhyolite pumice and differs substantially from granitic rocks in the Precambrian basement. This kind of granite is interpreted to be the intrusive

equivalent of the pumice lava. Duffield et al. (1996) estimated an age of about 23,500 years for the most recent pyroclastic eruption, essentially coeval with the last rhyolitic deposit, which brought the granophyric xenoliths to the surface. Further analysis made by Lowenstern et al. (2006) on these rocks evaluated an age of 15,200 years.

Figure 16. A detail of the pumice deposit outcropping in Figure 15, in which xenoliths are found (source: Ghinassi, 2015).

Extensive **basaltic lava flows** cover the bottom of the graben, both to the north and south of Alid. Most of them are younger than the Alid dome and lap unconformably against the flanks of the mountain. Vents of these basalts are marked by scoria cones (Figure 17), aligned on a north northwest-trending fissures and normal faults with a few meters vertical offset. These structures reflect ongoing crustal extension across Alid graben. Basalts show a large variety of textures, from nearly aphyric to abundantly porphyritic. Phenocryst assemblages include olivine, olivine + plagioclase, olivine + clinopyroxene, and olivine + clinopyroxene + plagioclase. Basaltic tephra layers are common, especially near vents.

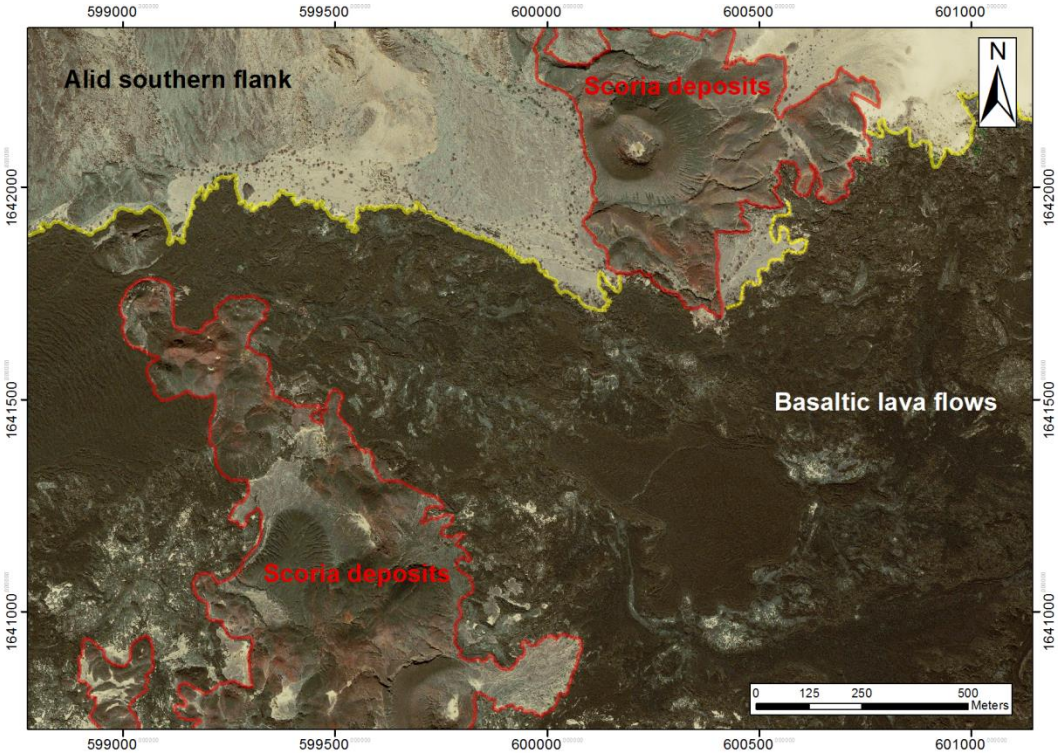

Figure 17. Bing image of the southern flank of Mt. Alid, in which scoria cones have been bordered with a red line and basaltic flows with a yellow line**.**

Fluvial deposits bury the outer margins of basalt fields, while aeolian sand partly covers the older flows (Figure 18). Basaltic flows deposits are mostly horizontal, deformed only close to the north northwest-trending fissure system. and likely help provide permeability to the Alid hydrothermal-convection system.

Figure 18. Contact between alluvial deposits and the recent basaltic flows (source: Duffield, 1996).

Open fractures dilation of Alid graben was used to estimate the minimum age of basalt flows. Since it is in the order of a few tens of meters, if the average rate of crustal spreading across the graben is the same of other incipient divergent plate-tectonic environments (about 2 cm per

year), the age should be less than 10,000 years. Further radiometric dating confirmed that these young basalts are Holocene in age (Duffield et al., 1996).

Three types of **alluvial deposits** are present: recent fluvial deposits, active alluvial fans and older alluvial fan deposits (oaf). Fans surrounding Alid dome contain predominantly volcanic lithologies from the Alid volcanic center, whereas those in adjacent areas have mostly basement lithologies. Older alluvial fans were deposited when the drainage base level was higher than today and are now being eroded. The prevailing granulometry is gravel.

2.3. Dome formation and magma evolution

How does a structural dome form in an environment of crustal extension? A likely answer is that a body of silicic magma intruded and collected within the upper crust and domed overlying rocks to form Alid structure (Figure 19). Structural doming caused considerable uplift of the shell and sedimentary units and consequently landsliding and collapse of the top of the mountain. This intrusion presumably formed and persisted at least until it partly erupted to produce the voluminous deposits of late Pleistocene rhyolite pumice. Blocks of granophyric and miarolitic granite in the pumice deposits are interpreted by Lowenstern et al. (1997) as the uppermost part of the shallow magma body that crystallized just prior to eruption of the pumice.

Figure 19. Image of the Alid dome taken from south-west (Duffield, 1996).

The intrusion is within the ranges of 2 to 5 km depth. The miarolitic texture in these clasts formed within this range, because the higher pressures associated with deeper levels tend to force fluid pockets closed during plutonic consolidation. Moreover, the granophyric texture implies rapid crystallization in a shallow magma body (Barker, 1970). The configuration of the dome itself provides compelling qualitative evidence of shallow depth to the source of the deformation. The dips, as steep as 65 degrees in strata on the flanks of the dome, could only result from a shallow source of deformation. A deep source would have produced a broad, low-amplitude upwarp, rather than small steep-sided uplift.

The onset of structural doming at Alid postdates about 36,000 years the age of a basalt flow stratigraphically high within the sequence of uplifted rocks (Duffield et al., 1997). Clinopyroxene-bearing rhyolite lavas erupted subsequent to the initiation of structural doming, and one of these lavas is dated at about 33.,000 years. The rhyolite pumice that unconformably overlies all dome-forming rock units is even younger and represents the final phase of the dome formation. It was dated by Duffield et al. (1997) at 23,000 years based on Ar–Ar geochronology. Lowenstern et al. (2006) indicate a slightly younger eruption age of about 15,000 years.

All analyzed volcanic rocks, both rhyolites and basalts, display considerable U/Th disequilibrium and ^{230}Th enrichment. The young basalts have high (^{230}Th/^{232}Th), whereas the older basalts and rhyolites have lower (^{230}Th/^{232}Th). This implies that the basalts and rhyolites may be closely related. The simplest explanation would be that the rhyolites are related to the basalts by simple crystallization and differentiation, consistent with linear trends for incompatible trace elements and the small shifts in radiogenic isotope composition from basalt to rhyolite (Lowenstern et al., 2006). The basalts themselves have ^{230}Th enrichment, which is consistent with the melting of an asthenospheric mantle source region and a garnet-bearing residuum that fractionates Th with respect to U (Asmerom, 1999; Bourdon & Sims, 2003).

3. Alid geothermal system

There is a lot of ground evidence of a shallow hydrothermal water circulation below the surface of Mt. Alid. The geochemical study of thermal vents conducted by Lowenstern et al. (1999) and the geophysical campaign made in 2008 by Eysteinsson et al. confirm that the presence of a high-temperature geothermal reservoir is very likely.

3.1. Shallow thermal manifestations

Fumaroles and boiling pools are distributed widely on the north half of Alid (Figure 20), suggesting that a hydrothermal system, which feeds the thermal manifestations, underlies much of the volcanic center. Between these, Darere, Ilegedi and As'ela are the most abundant vent areas and Ilegedi is the largest and most active. The estimated area of this shallow hydrothermal system is at least 10 km^2. All vent areas contain fumaroles at temperatures near the boiling point for their elevation.

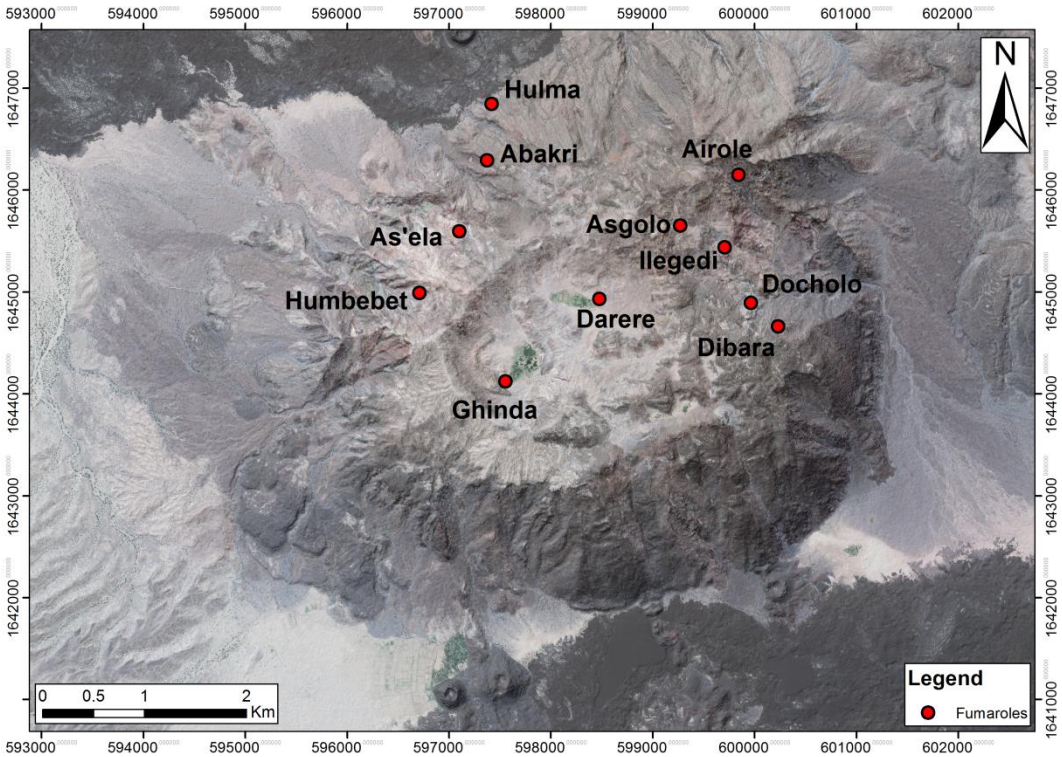

Figure 20. Satellite image in which Mt. Alid's fumaroles are pointed with the red dots.

The physical nature and geochemical environment of the hot springs and pools at these sites strongly suggest that the waters consist of mixtures of condensate of fumarolic steam mixed with cooler, shallow groundwater (Lowenstern et al., 1999).

Most of the thermal manifestations are located at elevations between about 460 and 600 m, though hot rock and steaming vents also are present as low as 225 m (Hulma) and slightly higher than 760 m (Airole). Fumarolic steams come up through rhyolite breccia (Abakri, As'ela, Darere), siltstones (Humbebet), and Precambrian basement rocks (Ilegedi). Therefore, location of the thermal features does not appear to be controlled by lithologic type or contacts between lithologic units. Instead, some fumaroles are aligned, suggesting some kind of structural control (see 6.6 for a complete analysis): Abakri, As'ela and Humbebet, on the north flank of the mountain, seems to have a NE-SW trend, roughly speaking, and Asgolo, Ilegedi, Docholo and Dibara a NW-SE trend.

Sample No^	ELG96-2	ELG96-3	ELG96-4	ELG96-5	ELG96-6
Location	Darere	Ilegedi No 1	As'ela	Ilegedi No 3	Abakri
Temp. (°C)*	95	95	95	84 (gas from bubbling pool)	94
CO_2 (mol%)[$]	97.93	95.53	98.20	95.89	98.86
H_2S (mol%)	0.219	0.876	0.749	0.662	0.143
H_2 (mol%)	1.093	2.498	0.503	2.624	0.605
CH_4 (mol%)	0.225	0.132	0.061	0.144	0.085
NH_3 (mol%)	0.128	0.389	0.004	0.005	0.095
N_2 (mol%)	0.412	0.598	0.473	0.653	0.209
O_2 (mol%)	0.0023	nd	nd	nd	0.0005
Ar (mol%)	0.0054	0.0126	0.0116	0.0140	0.0047
He (mol%)	0.00151	0.00047	0.00046	0.00073	0.00018
N_2/Ar	76.2	47.6	40.8	46.7	44.4
Gas/steam[†]	0.0448	0.0196	0.0259	1.701	0.0565
δD ‰ VSMOW	10	5	5	n.a.	−1
δ^{18}O ‰ VSMOW	−4.0	−0.9	−1.7	n.a.	−2.8
δ^{34}S ‰ CDT	−1.7	0.9	2.0	2.0	1.3
δ^{13}C ‰VPDB	−3.4	−3.4	−4.9	−3.3	−3.3
T Calc (DP) °C[@]	218	266	225	262	206
T Calc (H-Ar) °C	336	336	290	334	323

n.d. not detected; n.a. not applicable
[$] Gas concentrations in mole % of dry gas.
[†] Gas/steam ratio is moles total non-condensible gas divided by moles H_2O.

Figure 21. Gas samples of Alid fumaroles and their relative concentrations.

Thermal pools, derived from steam condensation, all have an acid-sulfate composition and contain little chloride (Clynne et al., 1996). They are highly evaporated and have relatively high total dissolved solids ranging from about 1500 to 2500 mg/kg. Their compositions seem mainly controlled by dissolution of the surrounding host rock by sulfuric acid, causing the alteration of feldspar to great quantities of clay minerals and release of cations into solution.

Gas samples from Alid fumaroles collected by Lowenstern et al. (1999) showed that they generally have more than 95% of steam (full concentrations in Figure 21). Gas/steam ratios do not necessarily reflect the compositions of deeper, hotter parent fluids: some steam may have condensed, causing the remaining steam to become enriched in non-condensable gas. With the exception of Hulma, most of the Alid fumaroles have roughly similar gas compositions. The non-condensable gas compositions of all samples range from 95.5-98.9 mol % CO_2, and H_2 is generally the next most abundant component (0.5-2.6 mol %). The Darere fumarole is enriched in He, which may come from radioactive breakdown of crustal components or could be provided by magmas coming from the upper mantle.

3.2. Reservoir temperature

Nine gas geothermometers were used by Lowenstern et al. (1999) to estimate geothermal fluid temperature from fumarole samples. The D'Amore & Panichi (1980) geothermometer, which utilizes the relative abundances of CH_4, CO_2, H_2S and H_2, indicated reservoir temperatures of 265 °C for Ilegedi, the largest and most active of the Alid geothermal manifestations. The H_2/Ar method outlined by Giggenbach & Goguel (1989), which is based on progressive dissociation of hydrogen from water with increasing temperatures (Argon is used to normalize the abundance of hydrogen, since it does not change significantly due to secondary processes), showed ratios consistent with very high temperatures, ranging from 290-336 °C. The CH_4/CO_2 and CO_2/Ar geothermometers (Giggenbach & Goguel, 1989) also indicated high temperatures, up to 340 °C for Ilegedi. Gases from Darere, As'ela and Abakri also hinted at consistent and high

temperatures of at least 210 °C, and generally much higher. For only one sample the estimated temperature was less than 200 °C, probably due to contamination of the samples by shallow groundwater and organically derived materials, which tend to force underestimations of the original reservoir temperatures.

Gas geothermometers therefore suggest a very high reservoir temperature, over 225 °C and probably over 300 °C.

3.3. Isotopic composition of thermal fluids

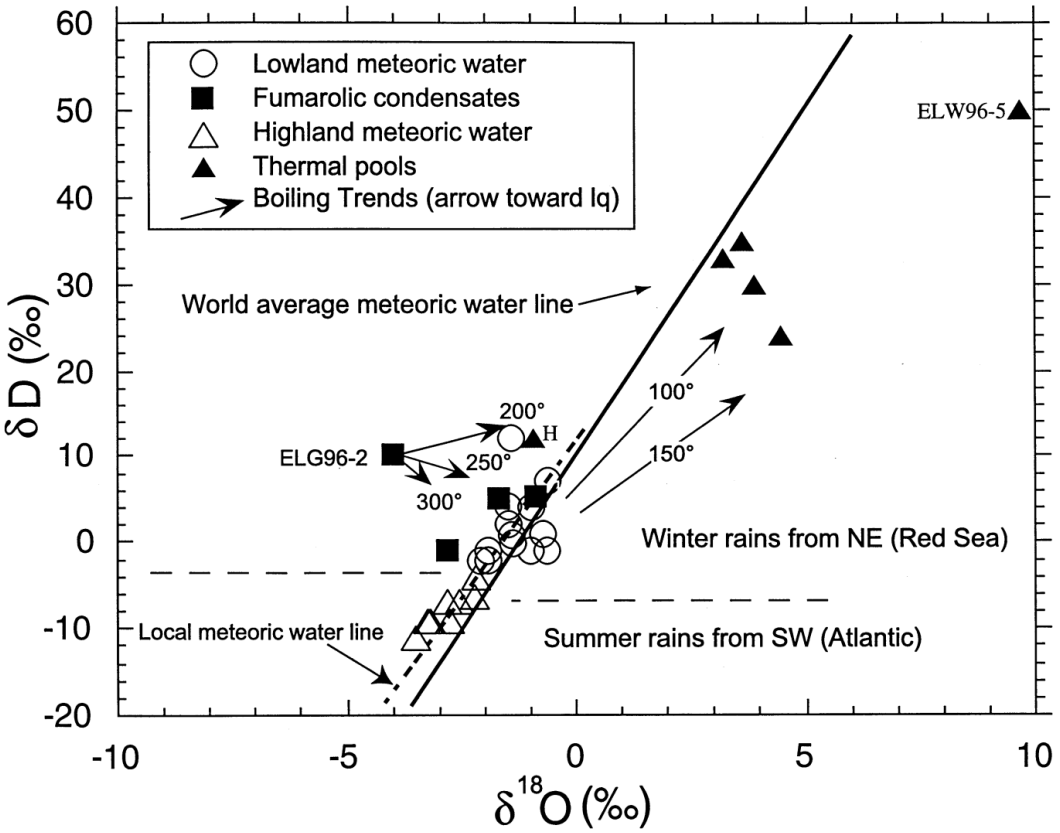

Figure 22. Stable isotope variation diagram for δO^{18} and δD in units of per mil (‰) relative to VSMOW.

The isotopic composition of Alid thermal water samples is generally very heavy (δD up to +51‰) with only one exception. As it is shown in Figure 22, their concentration plot below the world meteoric line. Their isotopic compositions are the result of high-temperature evaporation of relatively stagnant water bodies, made up by local groundwater mixed with steam condensate. These

pools are heated partly by condensation of steam that enters the pools from below, partly by heat transport by convection (like a heat pipe) and conduction from the underlying hydrothermal system. The higher values of $\delta^{18}O$, compared to the world meteoric line, are probably due to reactions between relatively stagnant and sometimes acidic pool water and Precambrian wallrock (Lowenstern et al., 1999).

The isotopic compositions of the condensed fumarolic steam samples all lie above the Global Meteoric Water Line (Figure xx), as expected (boiling solutions always produce steam that has a $\delta^{18}O$ value less than that of the coexisting liquid water). The steam could have been derived by high-temperature boiling of water that is isotopically similar to meteoric water that falls in the lowland region. The isotopic composition of the steam condensate also is compatible with a deep salty water reservoir. The isotopic data also indicates that the fumarolic steam could not have been derived from a boiling reservoir water that is isotopically similar to the highland meteoric water.

At this time it appears most likely that the reservoir waters within the Alid hydrothermal system are either groundwater that are recharged by winter rains that fall in the Eritrean lowlands, or by fossil Red Sea water, left over when the Red Sea filled the Danakil Depression, that may pervasively underlie freshwater lenses in the Danakil lowland region, due to the higher density (Lowenstern et al., 1999).

The $\delta^{13}C$ values of the Alid hydrothermal fluids varies from -3.3 to -4.9‰ VPDB, consistent with a magmatic source of CO_2 , possibly mixed with carbon from marine carbonate. It is believed that much of the CO_2 , S, and He emitted from Alid fumaroles are produced by degassing of the igneous body underlying Alid and its geothermal system.

3.4. MT-TEM geophysical survey

A geophysical survey of the Alid geothermal area was performed in 2008 in order to delineate the geothermal reservoir (Eysteinsson et al., 2010). Two main techniques were used: Transient Electro Magnetism (TEM) and Magnetotelluric (MT) resistivity soundings. A total of 67 TEM and 52 MT soundings were

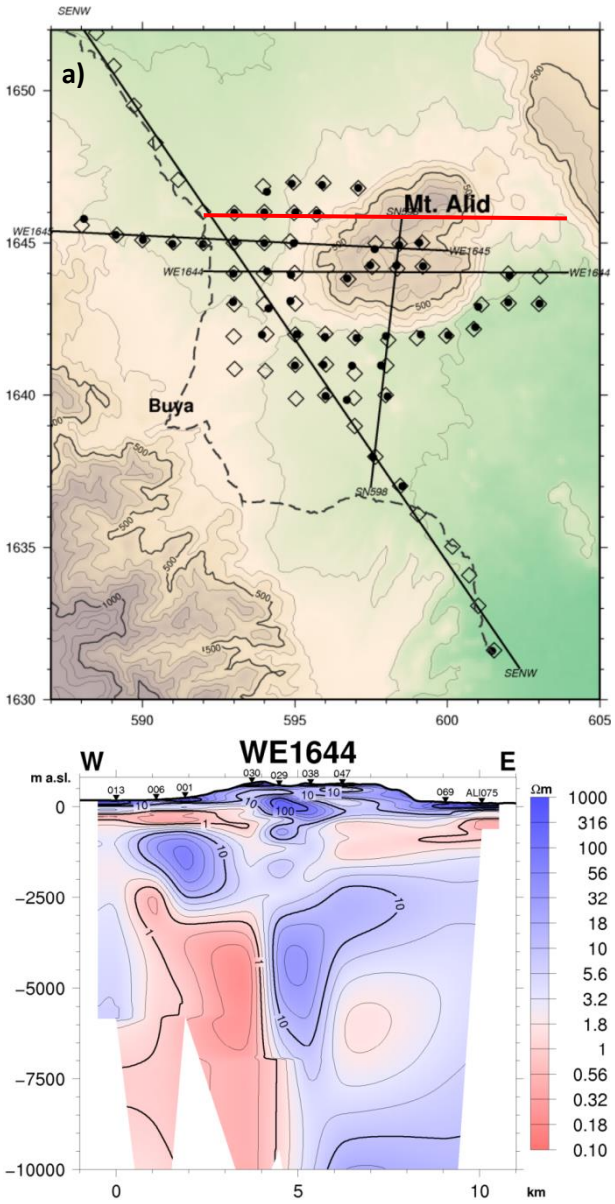

Figure 23. Resistivity cross section (relative to the red line on the map above), in which four resistive layers appear and the heat source seems to be confined on the western flank of the mountain (Eysteinsson et al., 2010).

performed in 24 days, covering the west flank and the top of the Alid mountain complex. There are four distinct resistivity layers which characterises the Alid underground, according to Teklesenbet (2012) (Figure 23):

- A thin high resistivity superficial layer, a few hundred meters thick, seen in most of the soundings, except in those on the top of mount Alid;
- A lower resistivity layer, which underlies the previous layer, also a few hundred meters thick;
- A high resistivity body, set below the western part of the volcano, approximately 3 km wide and with a NNW-SSE direction. It reaches the highest elevation at 2-3 km b.s.l. and extends down to a depth of about 7 km;
- Another low resistivity zone which extends into the deep crust.

A sharp boundary lineament was also found, at a depth interval of 500 m to 2 km and with a SW-NE trend, probably a vertical fault intersecting the geothermal reservoir which most likely controls the main upflow from the reservoir.

4. Modelling the geothermal system

Starting from the analysis of the USGS geological and geochemical campaign conducted in 1996 and the MT-TEM survey performed in 2008, a first attempt to identify the location and potential of the geothermal resource has been made. In cooperation with the IGG-CNR (Istituto di Geoscienze e Georisorse-Consiglio Nazionale delle Ricerche) research institute of Florence, the Alid subsoil has been simplified and schematized, assigning to every rock a specific thickness and proper hydraulic and thermal properties, in order to realize a numerical model of the geothermal reservoir, through the software PetraSim and the TOUGH2 code.

4.1. Reservoir identification

Resistivity data of the Alid subsoil was first interpreted by Teklesenbet (2012) following the Icelandic resistivity model, with the assumption that Icelandic basaltic crust is quite similar to the Afar Rift crust. Therefore, it was supposed that resistivity is mainly influenced by mineral alteration. In fact, all high temperature geothermal fields in Iceland show approximately the same structure, reflecting the hydrothermal alteration (Figure 24): a layer of resistive unaltered rocks outside the reservoir (50-100°C); a low-resistivity layer at the outer margins of the reservoir, where low-temperature zeolite and smectite alteration lowers the rock resistivity; an inner resistive core in the lower part, in which high-temperature alteration (more than 250 °C) brings about the formation of high-resistivity minerals like chlorite and epidote. The deep conductor was interpreted to be the heat source of the geothermal reservoir, as partial-melted have low resistivity values.

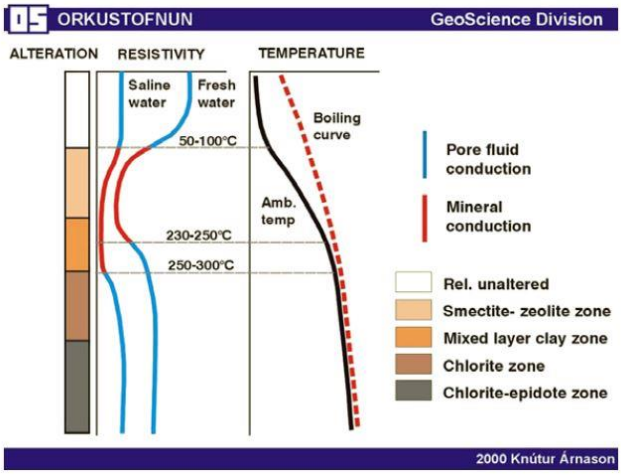

Figure 24. Icelandic interpretation of resistivity structure in high-temperature geothermal fields (Tsend-Ayush, 2006).

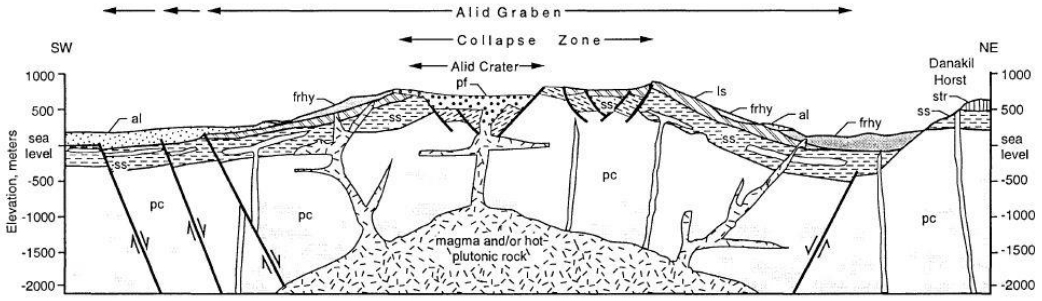

Figure 25. Simplified cross-section of the Alid volcanic complex (Duffield et al., 1996).

Teklesenbet's supposition, for which the Icelandic oceanic crust is comparable to the crust of the EARS is a strong assumption, hence it has been rejected and a new subsoil model has been made, in cooperation with Dr. Montanari and Dr. Montegrossi, from the IGG-CNR research institute. For this purpose, the schematic geological cross-section made by Duffield et al. (1996), albeit simplified, has assumed to be valid (Figure 25).

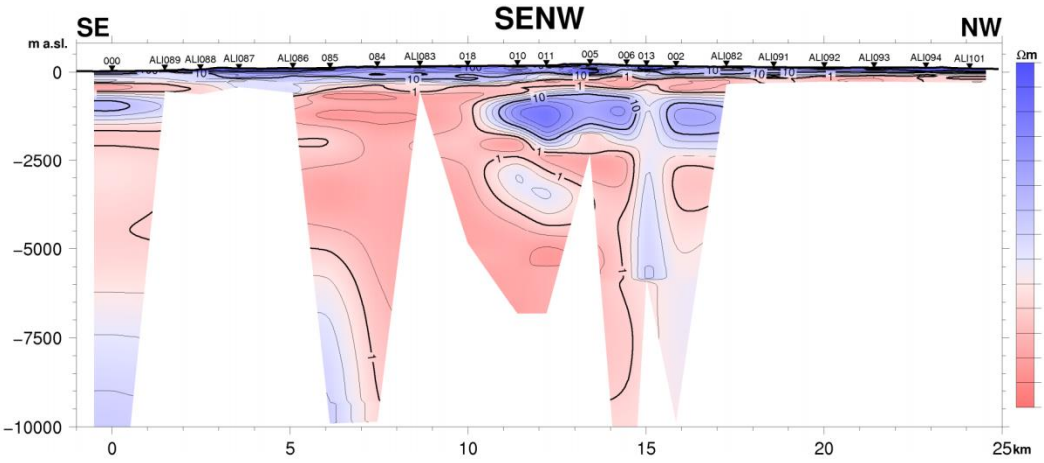

Figure 26. NW-SE resistivity cross-section. The geothermal reservoir is the blue, resistive zone at the centre **(**Eysteinsson et al., 2010).

The resistivity behaviour (see Figure 26) has been explained as following. The first resistive layer (about 50 m thick) is probably formed by unaltered basaltic lava flows and quaternary shallow-marine sedimentary deposits. The low resistivity layer below (few dozen meters thick) has been interpreted as the aquifer cited by Lowenstern et al. (1999) in their geochemical reconnaissance of Alid thermal water, probably laying in the sedimentary deposits or along the contact

between these rocks and the shallow, fractured and weathered part of the Precambrian basement. The water contained in the aquifer may have caused the decrease of resistivity, especially in case of high salinity. This assumption agrees with the measured temperatures of Alid fumaroles (around 90-95 °C). Since the estimated temperature of the heat source is around 250 °C, without this shallow aquifer fumarolic steam should have a considerably higher temperature. Considering such values of electrical conductivity, the resistive core (2 km thick) is probably a vapour-dominated geothermal reservoir, entirely laying in the fractured and permeable basement, and the chlorite-epidote alteration zone forms only the cap-rock, rather than the resistive layer itself; it is probably caused by the partial melted magmatic heat source, which represents the deep conductive zone.

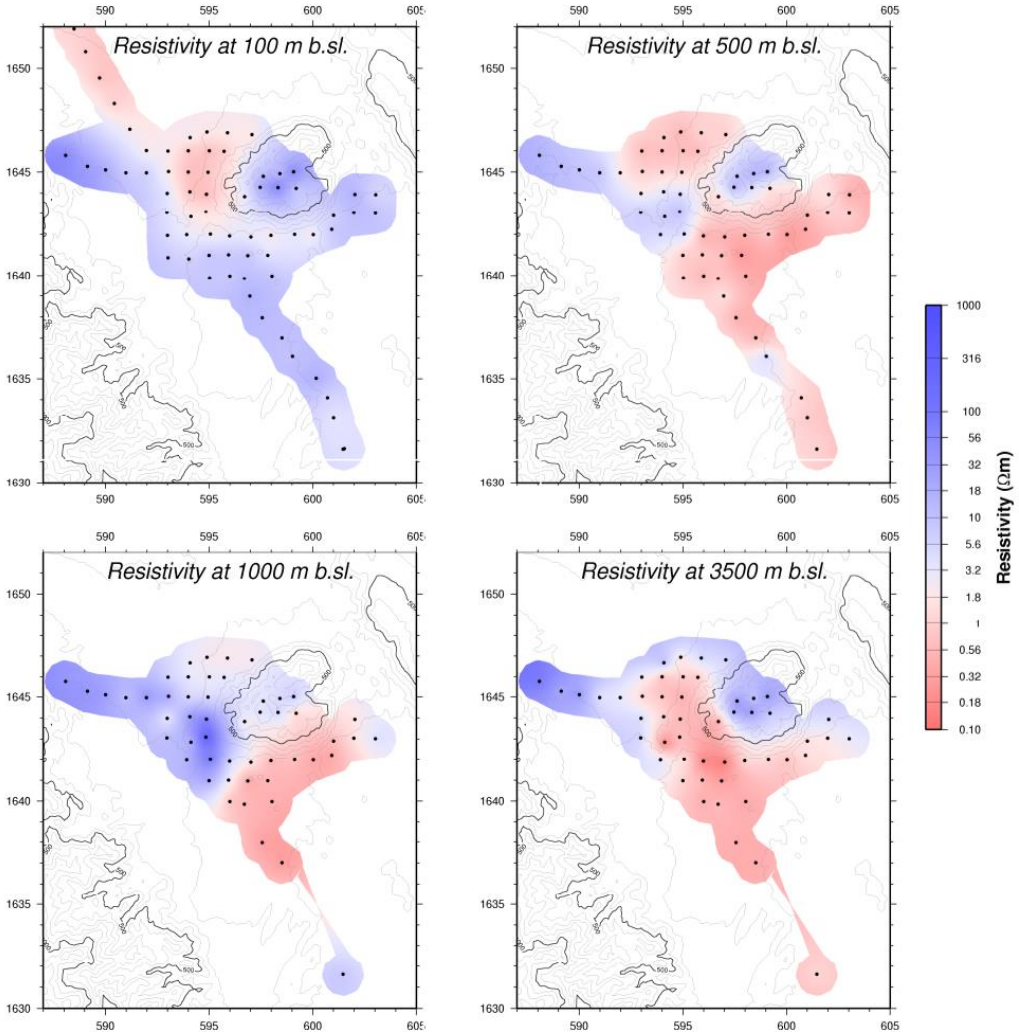

Figure 27. Iso-resistivity maps obtained from MT-TEM geophysical data (Eysteinsson et al., 2010).

From the analysis of iso-resistivity maps and cross sections, obtained from multidimensional inversion of MT and TEM data (Figure 27), it seems that the south-western flank of Mt Alid is the most suitable for geothermal exploration. Here, the positive anomaly identified as the steam reservoir is shallow and lies between 500 m and 2500 m b.s.l.

4.2. Conceptual model of the reservoir

Once the location of the reservoir has been fixed, the definition of the geometrical and physical properties of all rock units underlying the Alid western flank has been taken into account. A simplified section of the subsoil and a characterization of thermal and hydraulic properties of each rock composing the selected area has been carried out. The conceptual model has been obtained from the interpretation of electrical resistivity profiles derived from MT surveys conducted in the west side of the Alid complex (e.g. Figure 23 and 27).

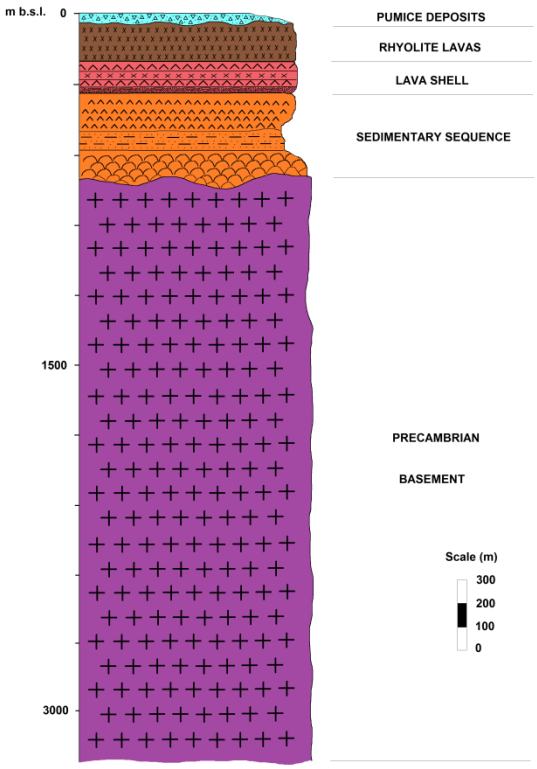

Figure 28. Schematic stratigraphic column of the western flank of the Alid complex.

The complex geological structure of the subsoil has been simplified in a five-representative-layers schematic stratigraphic column (Figure 28), in which the five main lithological units have been merged, giving to each of them different physical properties, defining the input data to implement through the TOUGH2 software, a specific code for modelling the high enthalpy geothermal systems. In this scheme, every rock formation is divided into sublayers, whose thickness is a function of the estimated abundancy of the different lithologies constituting every rock formation.

The following is a description of the simplified geological sequence:

- Precambrian Basement, mainly consisting of quartz-muscovite schist and minor kyanite schist with dikes of Aplite and amphibolite, has been assumed to be formed only by mica-schist, with a thickness of 2500 m;
- Sedimentary Sequence, an ensemble of intercalated volcanic and sedimentary rocks, is 350 m thick and it has been divided into three main sub-layers, each of them represents 1/3 of the total fraction: a lower level dominated by pillow basalt and hyaloclastytes, a level of shallow marine sediments (siltstones, sandstones, gypsum and anydrite) and an upper level of subaerial and altered basalts;
- The Lava Shell, formed by andesite and rhyolite lava flows with dominant interbedded basalts, has been arbitrarily divided following the plausible estimation made by Duffield et al. (2006), subdividing it in 1/2 of unaltered Basalt, 1/4 of andesite and 1/4 of Amphybole Rhyolite; the whole layer is 150 m thick;
- Rhyolite and Pumice deposits represent the top of the model and they are 150 m and 25 m thick, respectively.

After having defined their vertical and aerial extension , the rock layers have been associated to their thermal and hydraulic properties, in order to build the geothermal model and simulate, through the TOUGH2 code, the behaviour of the geothermal reservoir. The physical properties necessary for the implementation are: thermal conductivity λ, constant pressure specific heat cp, density ρ, permeability k, hydraulic conductivity K and porosity ϕ. Generally, during the definition of a conceptual model, an explorative well has already been drilled in order to define exactly the rock properties of a specific site, but in Alid's case this activity has not been done yet because the study is in an early stage. For this reason no measured data on these properties is available. Therefore, a wide literature research has been done to collect the largest and most representative data values and estimate an average value for the thermo-physical properties of the considered layers implemented in the geothermal model.

Stratigraphic unit	Lithology	Th. conductivity λ[W/mK]	Specific heat cp[kJ/kgK]	Density ρ[g/cm^3]	Porosity ϕ[%]	Intr. permeability k[d]	Hydr. conductivity K[m/s]
Pumix	Pumix	0,25	*0,8*	0,5425	75	6,17E+00	*1,00E-07*
Rhyolite	Rhyolite	3,3	*0,8*	21,245	23,44	1,71E-02	1,51E-07
Lava shell	Andesite	1,98	0,815	2,732	5,605	5,15E-08	*1,00E-07*
Sed. seq/lava shell	Basalt	1,87	0,88	2,82	8,9	6,16E-05	1,63E-07
Sedimentary sequence	Gypsum	1,6	1	22,875	8,1	*1,00E-04*	*1,00E-12*
Sedimentary sequence	Anhydrite	4,9	0,81	2,9	2,75	1,41E-04	5,05E-12
Sedimentary sequence	Sandstone	2,5	1,305	24,005	13,65	5,05E-04	6,35E-04
Sedimentary sequence	Siltstone	2,335	*1,3*	1,91	29,8	4,55E-06	7,01E-09
Sedimentary sequence	Hyaloclastytes	1,8	*0,8*	2,85	12	7,09E-04	*1,00E-07*
Precambrian Basement	Schists	3	0,948	27,465	1,94	3,12E-07	2,31E-06
Precambrian Basement	Gneiss	2,44	0,835	2,7	2,12	2,87E-06	4,60E-06

Figure 29. Thermal and hydraulic properties chosen for the lithologies constituting the Alid subsoil.

The literature research yielded a considerable amount of information (see Appendix 1 and in Appendix 2 for the full list), from which representative values for the model have been chosen. The median has been calculated where there was more than a single value, whilst some assumptions have been done where no information was available, evaluating the properties of similar rocks. Considering the textural and compositional similarity of some lithologies, in relation to their hydraulic properties, gypsum has been considered as anhydrite, andesite as basalt, pumix and hyaloclastytes as rhyolite. The most difficult thermal property to recover was specific heat of some type of rocks. Assumed that these values have a small range of variation because of their similar petrological compositions, siltsone's specific heat can be considered equal to the sandstone's values, while hyaloclastytes, pumix and rhyolite can be assumed to have the same value of anhydrite. These assumptions may be acceptable as these lithologies have, in literature, similar thermo-physical properties The values chosen for the characterization of the conceptual model are shown in Figure 29.

4.3. 3D model of the reservoir

After having schematized the Alid subsoil, it was necessary to realize a three-dimensional model of the western flank of Mt. Alid and subsequently import it into the Petrasim modelling software. This model has been carried out with the IGG-CNR researcher Dr. Montanari (Figure 30).

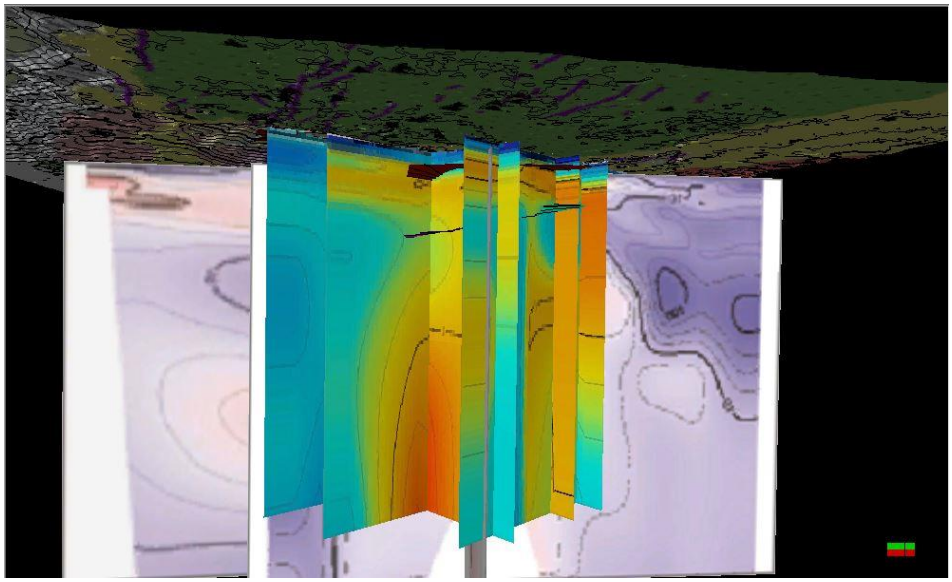

Figure 30. Petrel screenshot in which georeferenced resistivity cross-sections are shown.

All available data has been geo-referenced, using the GIS software ArcMap, and subsequently imported into the Petrel 3D modelling software, which has been able to interpolate, from the iso-resistivity curves of the cross sections and the resistivity depth slices, the main surfaces constituting the geothermal reservoir. A digital model of the Alid topography has been imported as well, a clipped version of the ASTER GDEM (see Chapter 5 for its specifics), constituting the uppermost surface of the three-dimensional model.

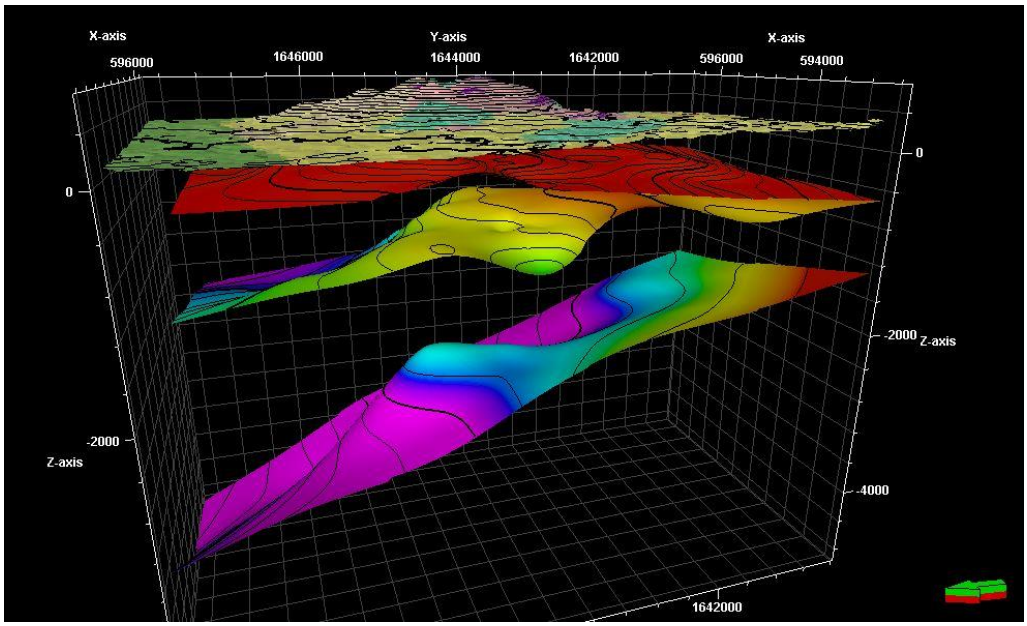

Figure 31. Results of surfaces interpolation from resistivity cross-sections of Figure 30.

The surfaces obtained from the interpolation process, shown in Figure 31, represent the boundaries of the geothermal system as well as of thoseof the numerical model: are recongnizable, from the surface the top of the shallow aquifer, the top of the reservoir and the top of the heat source layer. These surfaces represent the boundaries of the components forming the numerical model.

4.4. Modelling with Petrasim

Before implementing the Alid model in the PetraSim interface, in cooperation with the IGG-CNR researcher Dr. Montegrossi and the Ing. Tognoli (Master Degree Thesis-University of Padua), from geological and geochemical data collected by Duffield et. al (1996), a first preliminary estimation of the Temperature-Pressure, Pressure-Depth, and Temperature-Depth curves for the natural state of the reservoir has been done, in order to compare these curves with the output of the final model (Figure 32).

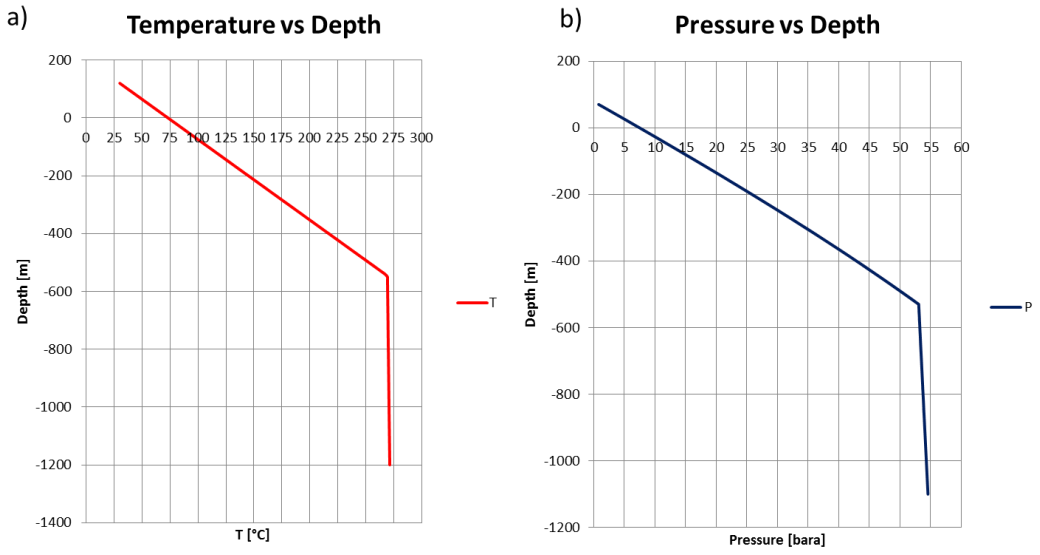

Figure 32. PreliminaryTemperature-Depth (a) and Pressure-Depth curves estimation.

The first step in the implementation of the Alid reservoir model in Petrasim has been the acquisition of the x-y-z coordinates of the geological surfaces that form the internal boundaries of the system. The topography, the top of the aquifer and the top of the reservoir have been previously obtained from interpolation of

resistivity cross-sections. Instead, the bottom of the shallow aquifer and the bottom of the reservoir have been modelled directly in the simulation program. For the bottom of the aquifer, a constant thickness of 50 m has been assigned and a new surface parallel has been modelled, in order to generate its top. In the same way the estimated bottom of the reservoir has been given: this time a specular reflection of the coordinates of the top-reservoir surface has been done, because it was necessary to impose a closed space for the vapour-dominated reservoir. Once these surfaces have been imported, the 3D model has been generated and consequently divided in six main domains (Figure xx) and a polygonal mesh has been produced, with a regular grid of 15840 cells (20x36x22).

The six layers constituting the model are named, from the top to the bottom, Rock 1, Aquifer, Rock 2, Reservoir, Rock 3, Basement. Each of them is characterized by a different material (Figure 33).

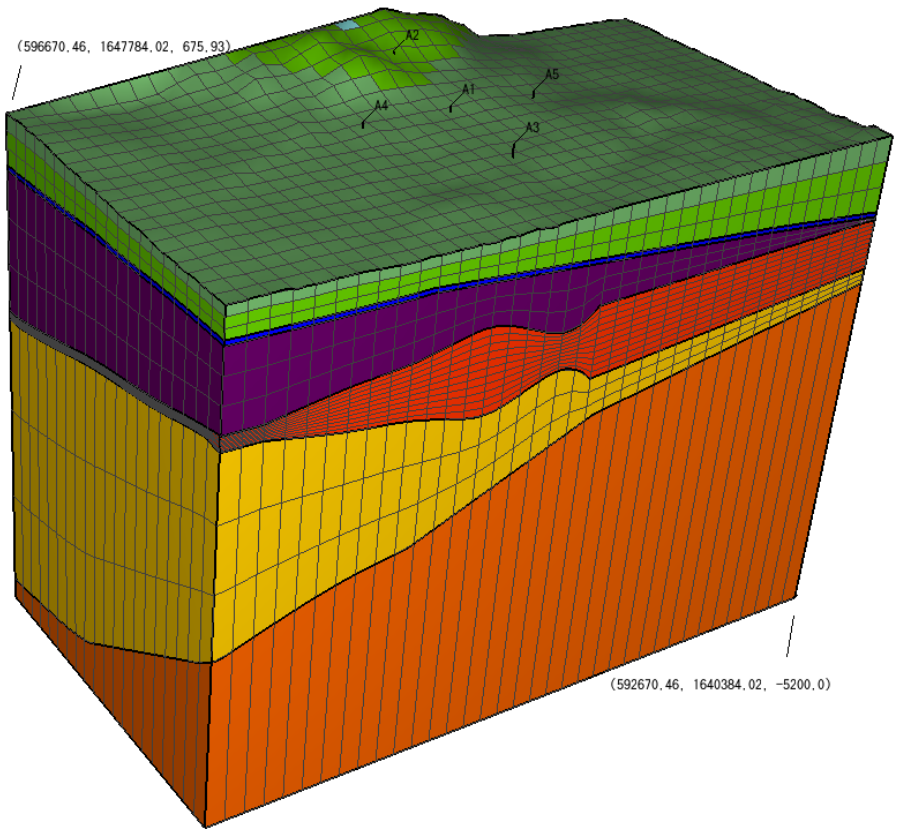

Figure 33. Polygonal mesh of the three-dimensional model representing the Alid geothermal reservoir.

After that, the heat source, the fumaroles, the water recharge and a link between the shallow aquifer and the geothermal reservoir (which are the other features constituting the Alid geothermal system) have been implemented in the mesh. In order to represent these object, four new materials have been created and assigned directly to specific groups of cells. All the properties of the components of the geothermal system presented below are shown in Figure 34.

Layer	ρ [kg/m^3]	ϕ	k_x [m^2]	k_y [m^2]	k_z [m^2]	λ [W/m°C]	c_p [J/kg°C]
Basement	2747	0.002	3E-22	3E-22	3E-22	3	948
Rock3	2747	0.002	3E-22	3E-22	3E-22	3	948
Reservoir	2747	0.06	1E-14	1E-14	1E-14	3	948
Rock2	2747	0.002	3E-19	3E-22	3E-22	3	948
Aquifer	2603	0.14	2.5E-14	2.5E-14	2.5E-14	2	1020
Rock1	2624	0.12	5E-15	5E-15	5E-15	2.26	848
Top_Boundary	2624	0.1	5E-26	5E-26	5E-26	2.26	1E05
Link	2747	0.14	2.5E-15	2.5E-15	2.5E-15	3	948
Heat Source	2747	0.002	3E-22	3E-22	3E-22	3	1E5
Fumarole	2747	0.01	1E-15	1E-15	1E-15	3	948

Figure 34. Hydraulic and thermal properties of the materials constituting the 3D model.

The heat source (Figure 35.a) has been represented as a cooling plutonic dyke located in the bottom layer of the reservoir. With a trial-and-error process has been applied, the dyke has been reshaped and extended, in order to reach in the reservoir the temperature conditions indicated from the geochemistry (260-270 °C). It is formed by the same material of the basement, except of the infinite value of the c_p parameter. An initial condition of 330 °C and 1.013 * 10^5 Pa has been given to the heat source.

The fumarole system, which connects the reservoir to the surface, has been simplified as a single and bigger fumarole (Figure 35.b). It has been modelled as a simple column of cells and it has been positioned on the western slope, close to the Ghinda thermal area. To avoid dispersion of fumarolic steam, a group of cell of the same non-permeable material constituting the Rock 2 layer (the

Precambrian basement under the Sedimentary Sequence) has been created around the fumarole. Its shape has been changed several times during the modelling, to force the steam flow to reach the top surface.

Considering the local groundwater assessment, the recharge area has been implemented as a cell row on the west-side of the surface aquifer (Figure 35.c). For this feature, the material constituting the recharge is the same of the surrounding cells, but a condition of infinite volume of water has been assigned to them.

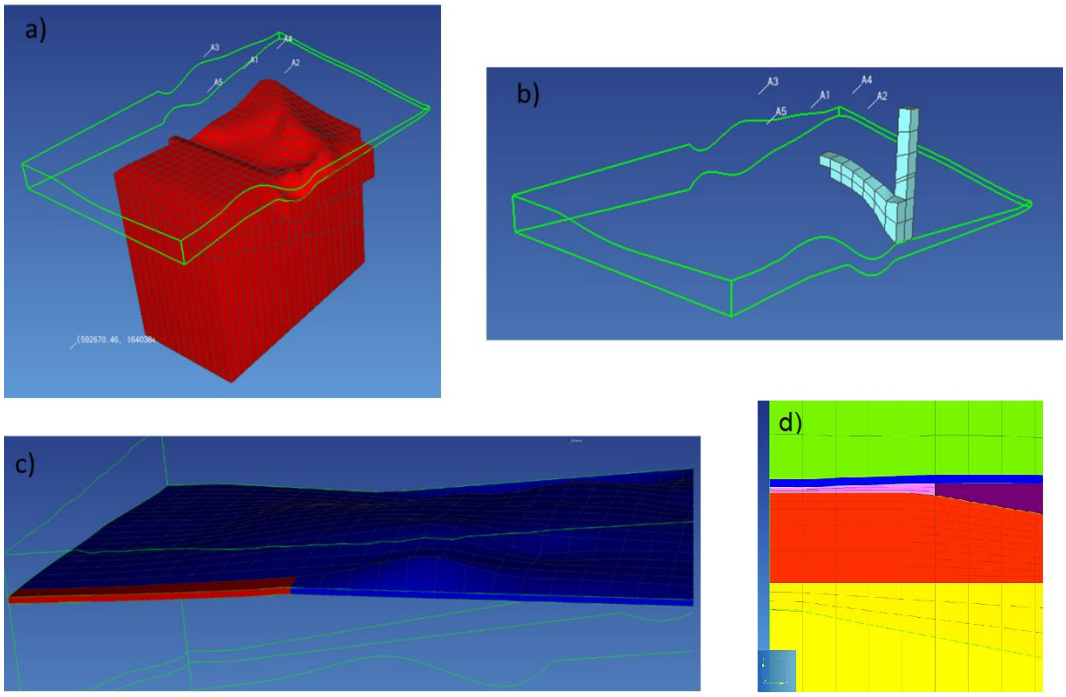

Figure 35. The four features added to the model: the heat source (a), the fumarole (b), the recharge (c) and the link between the aquifer and the geothermal reservoir (d).

Another important feature of this geothermal system is the connection between the reservoir and the aquifer (Figure 35.d). The two systems are not isolated one to each other, as suggested by the temperature and the chemistry of the fumaroles (Lowenstern, 1999), therefore a link has been modelled. Although the real nature of this connection is unknown, a pervasive fracture system caused by a fault

network may be the cause of this linkage, therefore high values of porosity and permeability have been given to some cells of the Rock 2 layer, in order to create such connection.

Besides the geothermal features, five wells have also been set in the model and each of them could be assigned to steam extraction or to the injection of the exhausted geothermal fluid. Petrasim automatically identifies the cells intersected by the wells and applies the appropriate boundary conditions.

Once defined all the materials, boundary and initial conditions, the model had the aspect shown in Figure 36

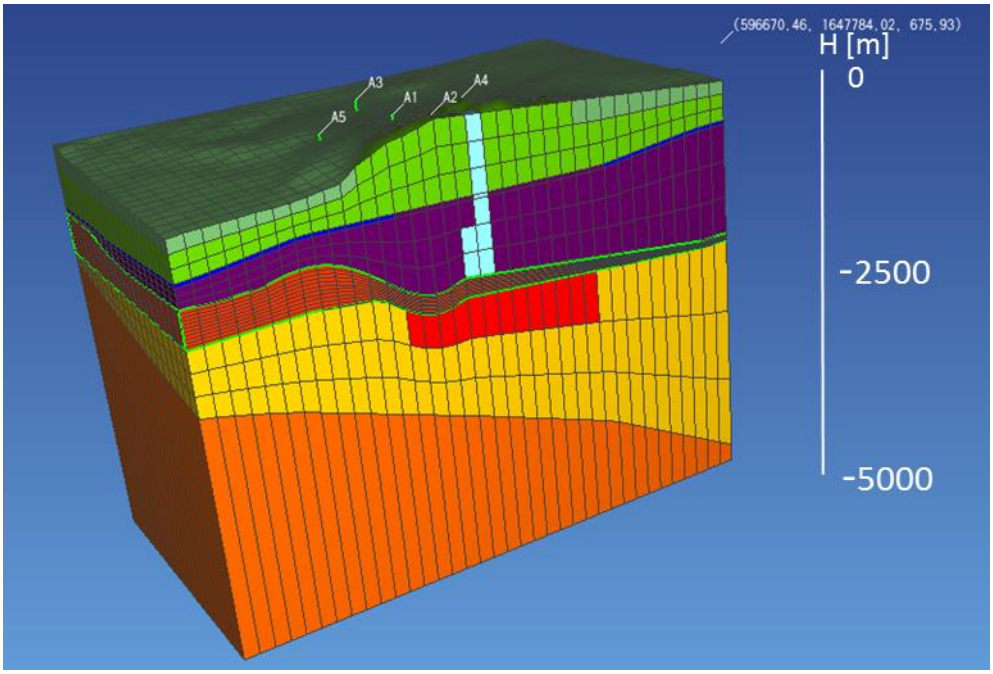

Figure 36. The final version of the three-dimensional mesh, in which the other four features have been added.

4.5. Simulation Results

On a first instance, wells have not been activated, to verify that the natural-state model of the geothermal system was sufficiently accurate: pressure, temperature and vapour fraction have been compared to the estimated values of the conceptual model.

Despite all the simplifications, the results of this simulation agree with the initial hypothesis, therefore this simplified and preliminary model can be

considered a good starting point for more advanced models that will be implemented next, when an exploration drilling will be performed.

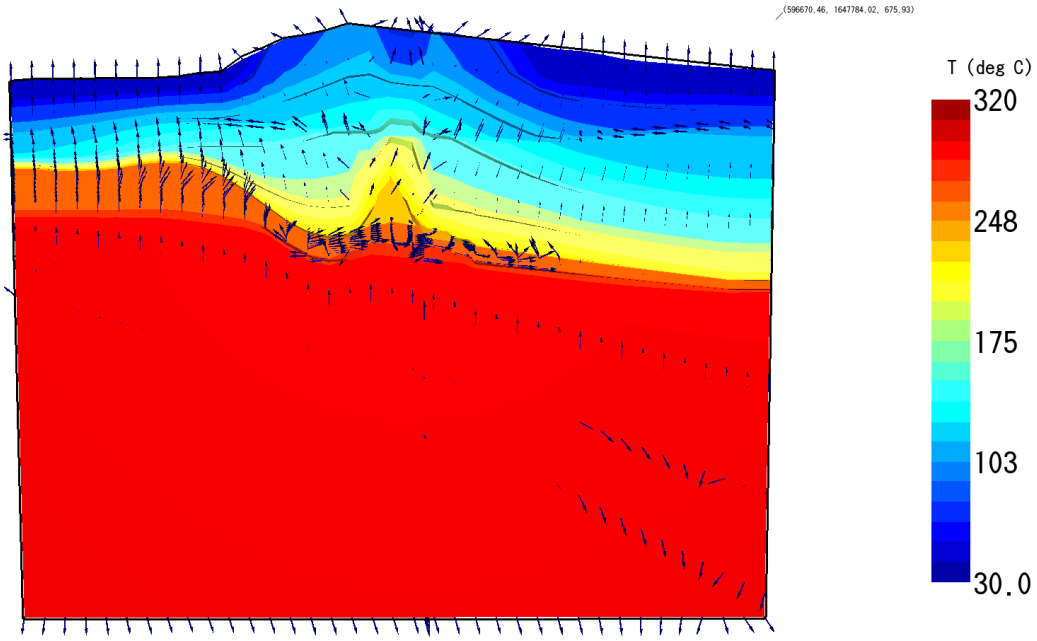

Figure 37. Temperature distribution within the natural-state geothermal model, including heat flux vectors.

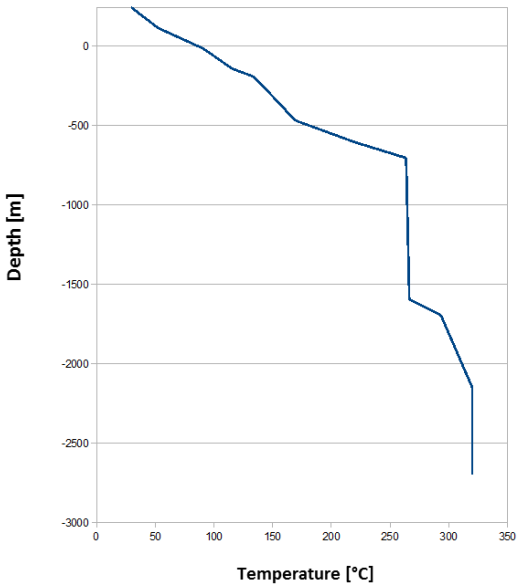

Figure 38. Temperature-Depth graph related to the simulation results.

In the cross-sections of Figure 37, the **temperature distribution** of the geothermal system is shown, including vectors representing the heat flux. When the system reaches the stationary state, the heat is transferred by thermal conduction from the dyke to the bottom of the reservoir, reaching a temperature of about 260-270 °C, consistent with the ones estimated in the conceptual model. The thermal anomaly around the fumarole pipe is due to the geothermal steam, which flows from the reservoir to the top surface.

In Figure 38 the Temperature-Depth graph of is represented: the temperature rises constantly in the hydrostatic part of the curve, reaches a constant value in the reservoir and finally the system reaches gradually the imposed temperature of 320 °C of the heat source. Temperatures are coherent with the estimated temperature trend of the curves calculated before the simulation.

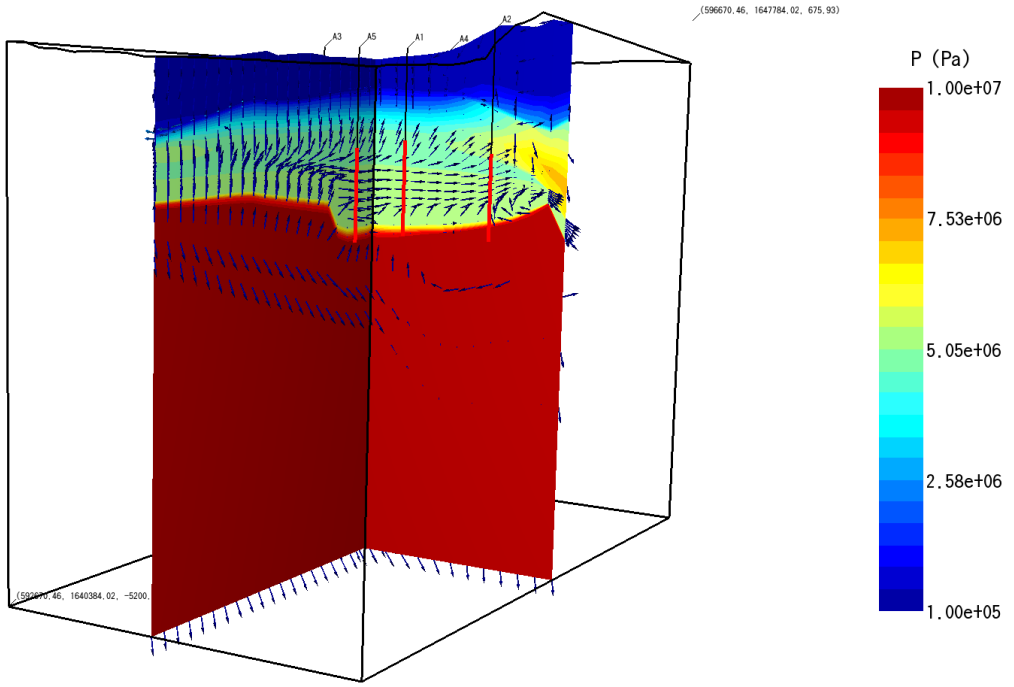

Figure 39. Pressure distribution within the natural-state geothermal model and flow vectors.

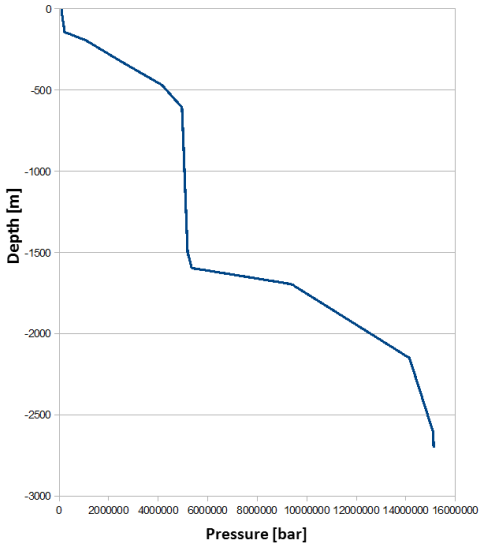

Figure 40. Pressure-Depth graph related to the results of the simulation.

Figure 39 represents the pressure distribution within the geothermal system together with the flow vectors. Pressure in the reservoir is about 50 bar, a value coherent with the natural-state curve calculated before, and in general the curve Pressure-Depth (Figure 40) shows a good match with the estimated values. The pressure curve shows also the phase transition from liquid water to steam occurring at -700 m b.s.l. and then the vapour-static section.

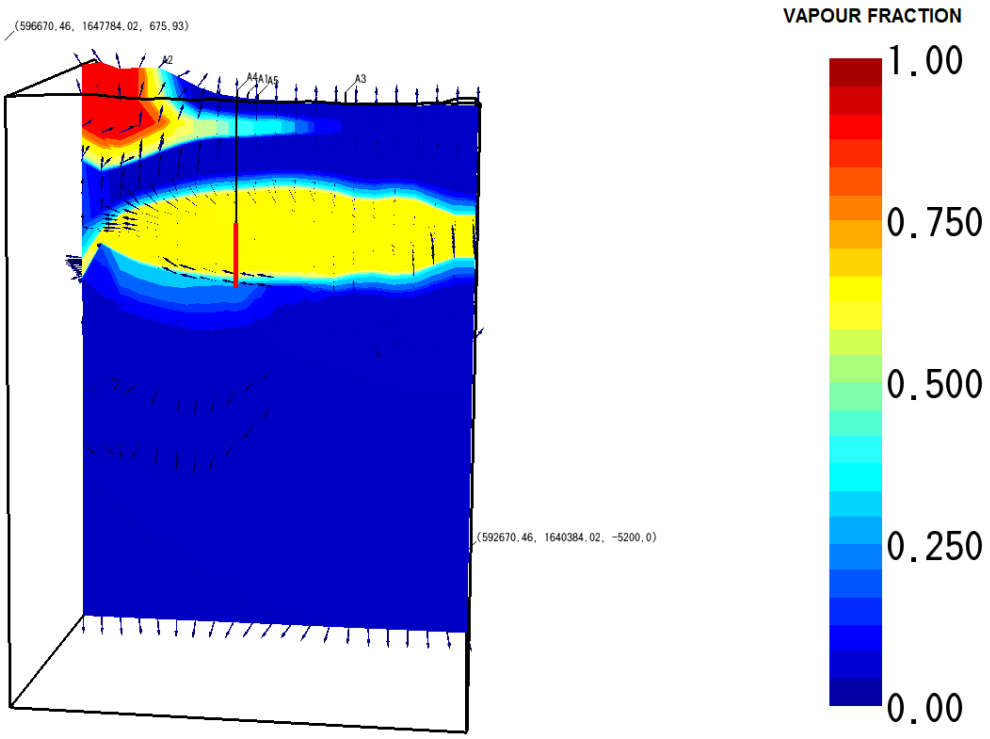

Figure 41. Vapour fraction within the modelled geothermal system. The position of the well is represented.

As regards the **vapour fraction**, from the cross-section of Figure 41 it is clear that the reservoir has reached the vaporization, with a vapour fraction of about 0.7. This is a typical value for vapour-dominated reservoirs (Pruess & Narasimhan, 1982). The high fraction of steam in the crater under the fumarole area is probably due to the depressurization caused by the fracture network, which has helped the vaporization process.

Finally, the five wells have been put into operation. According to Tognoli (2014), who simulated the energy production from extracted geothermal fluid, a net power ranging from 7 MW to 81 MW and a plant efficiency of 13.7% have been obtained, whit a reinjection of the 35% of condensed steam in the reservoir. A a well productivity of 20 kg/s of steam and an estimated capacity of Alid reservoir of 220 kg/s have been considered and the input flow rate of the power plant has been varied between 20 and 220 kg/s to reach different power results.

5. Remote sensing analysis - materials

The principal aim of the remote sensing analysis was to characterise geologic, geomorphological and structural features which outcrops the Alid geothermal area. The remote sensing based mapping activity was focused to identify also geothermal manifestations in the Alid area. Another objective was to extract geothermal anomalies from thermal infrared bands, in order to measure the heat contribution due to the presence of thermal vents.

Since the access to the study area is not easy, obtaining high quality material is essential to collect the maximum amount of information remotely, such as a detailed elevation model or multi-spectral satellite images.

The following paragraphs explain some key concepts about the remote sensing, which will be frequently mentioned, and list all the used datasets.

5.1. Basics of remote sensing

Remote sensing, in the widest sense of the term, is the acquisition of physical data about an object by means of propagated signals (e.g. electromagnetic radiation). This kind of signal may have originated directly from separate components of the target area, it may be solar energy reflected from them, or it may be reflections of energy transmitted to the target area from the sensor itself (White, 1977; Gomarasca, 2009).

One of the main benefits of remote sensing is the production of thematic and topographic map. Its fundamental characteristics are:

- a synoptic vision of ground surface conditions otherwise not obtainable with traditional techniques;
- a repeating cycle: periodic observations enabling temporal comparisons and updating of the collected data;
- multispectral and/or hyperspectral acquisitions.

Remote acquisition is developed in three phases: collection of data from the ground, aerial and/or satellite acquisition stations, processing of the collected data and, finally, data interpretation and restitution of thematic cartography.

The instruments are divided into passive sensor and active sensors. The first ones record the intensity of the reflected electromagnetic energy coming from the Sun or emitted by the Earth: photo cameras, scanners, thermal cameras and video cameras are part of this category. By contrast, on active sensors the acquisition systems emit radiation themselves, collecting the back signal (radar); the radiation is backscattered to the sensor with intensity depending on the structural characteristics of the examined surface and on the wavelength of the incident energy. For the remote sensing analysis conducted in the Alid geothermal field, only passive remote sensing sensors were used.

Below are explained some key concepts that will be used in the next part.

Swath width is the acquisition width, while the field of view (**FOV**) is the maximum angle of view. The instantaneous field of view (**IFOV**) defines the smallest area viewed by the scanner and establishes a limit for the level of spatial detail that can be represented in a digital image.

Spatial resolution is the ability of the sensor to discriminate two adjacent objects and for digital detectors is the dimension of a single pixel of the image. It depends on the detector itself but also on atmospheric diffraction phenomena.

Spectral resolution is the ability to discriminate between different wavelengths. It is usually defined by:

$$R = \lambda/\Delta\lambda$$

where $\Delta\lambda$ is the smallest difference in wavelengths that can be distinguished, at a wavelength of λ. The spectral resolution is also related to the number of spectral bands and their correlation.

Radiance is the brightness of radiation reflected from the Earth's surface. It is measured as brightness (watts) per wavelength interval (micrometer) per angular unit (steradian) per square meter from which it was reflected; thus the measured brightness is defined with respect to wavelength (i.e., "color"), spatial area (angle), intensity (brightness), and area.

Reflectance is the fraction of incident electromagnetic power that is reflected from the ground surface onto the sensor.

Thermal emittance or **thermal emittivity** is the ratio of the radiant emittance of heat of a specific object or surface to that of a standard black body. Emissivity and emittivity are both dimensionless quantities given in the range of 0 to 1, but emissivity refers to a material property (of a homogeneous material), while emittivity refers to specific samples or objects.

Brightness temperature is defined as the temperature a blackbody would be in order to produce the radiance perceived by the sensor. It is obtained by equating the measured radiance with the integral over wavelength of the Planck's black body function multiplied by the sensor response.

5.2. Landsat 8 data products

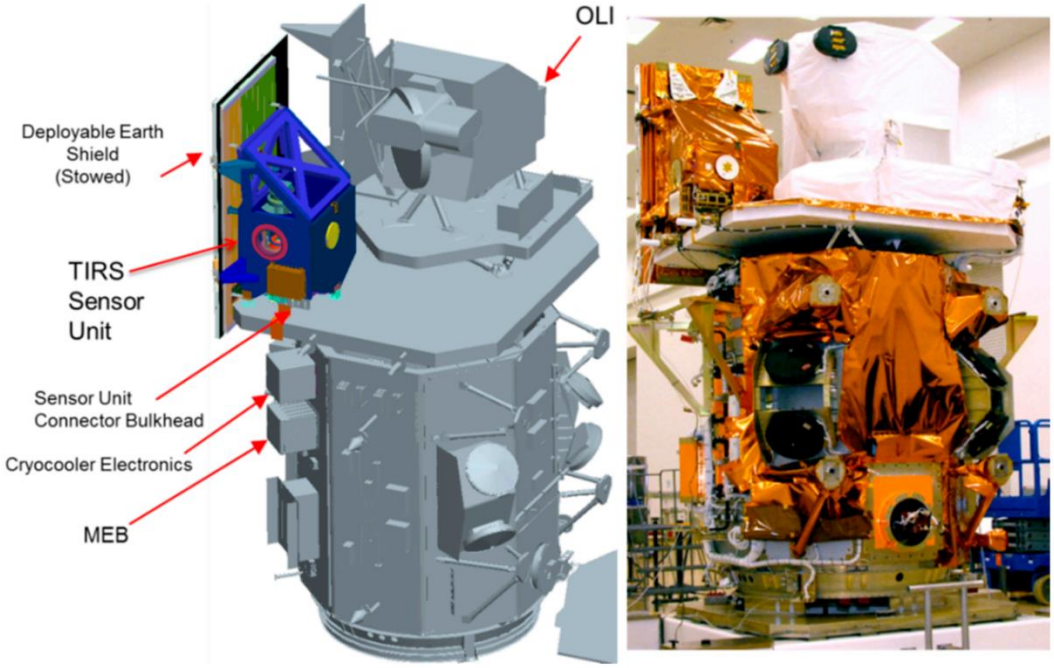

Figure 42. The two Landsat 8 instruments, OLI and TIRS, mounted on the spacecraft (source:nasa.gov).

Landsat 8 is a spacecraft jointly developed by the National Aeronautic and Space Association (NASA) and the United State Geological Survey (USGS), launched on 11 February 2013. It carries two multispectral instruments that are able to operate simultaneously, but independently (Figure 42): the Operational Land Imager (OLI) that acquires images in the visible, near-infrared and short-

wave infrared, and the Thermal Infrared Sensor (TIRS), a two-channel thermal imager. The Landsat 8 satellite have a near-polar, sun-synchronous, 705 km circular orbit and position, which gives the satellite a swath width of 175 km (Irons et al., 2012; Roy et al., 2014). OLI acquisition have a 30 m spatial resolution (15 m for the panchromatic band), while TIRS images have a pixel dimension of 100x100 m.

NASA provides global orthorectified Landsat images for free, that is why several Landsat 8 scenes have been collected and processed for mapping purposes. Moreover, they have a good resolution and a large swath width, giving them a great overview. Landsat scenes have been used for supervised classification process and spectral band combinations have been used to create specific RGB composities, which emphasized Alid rock differences.

5.3. ASTER L1B data products

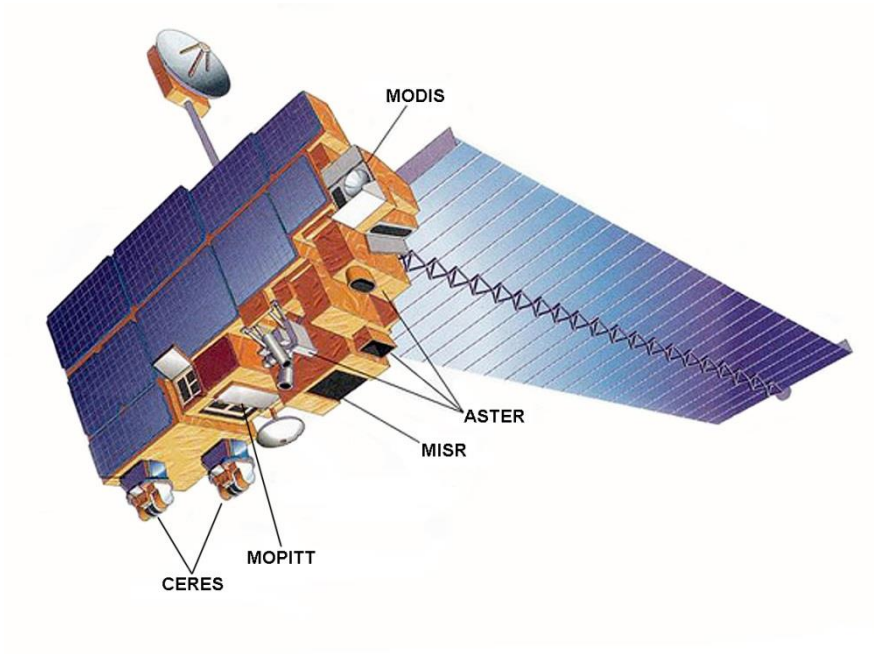

Figure 43. The Terra spacecraft, on which the ASTER sensor is mounted (source:nasa.gov).

The Advanced Spaceborne Thermal Emission and Reflection Radiometer (ASTER) is a multispectral scanning device (Figure 43), acquiring radiance in 14 different spectral bands, at variable spatial resolutions, depending on the

wavelength: 15 m in the visible and near-infrared (VNIR), 30 m in the short wave infrared (SWIR), and 90 m in the thermal infrared (TIR). The swath width is 60 km (Abrams et al., 2002).

The VNIR Band 3 have two sensors acquiring at the same spectral range: a nadir and an additional backward telescope, which gives ASTER a stereoscopic capacity (see paragraph 5.6).

The ASTER L1B registered radiance at the sensor products contain radiometrically calibrated and geometrically co-registered data for the acquired channels of the three different telescopes. This data is freely obtainable only for US users. An application to NASA has been done and, after being allowed, eight datasets have been downloaded from the NASA Reverb portal

ASTER images have been used especially for the thermal analysis of the Alid surface, aimed to isolate shallow geothermal heat anomalies.

5.4. ALOS PRISM high resolution DEM

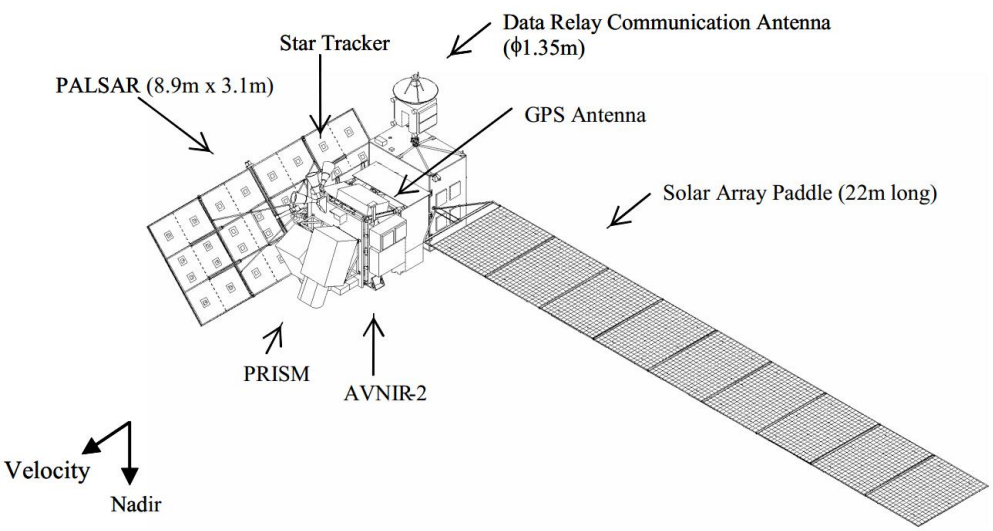

Figure 44. The ALOS satellite and its principal features (Osawa, 2004).

The Advanced Land Observing Satellite (ALOS) is a high-resolution land observation satellite, launched by the Japanese Aerospace Exploration Agency (JAXA) in 2004. Its major sensors are Panchromatic Remote-sensing Instruments for Stereo Mapping (PRISM), Advanced Visible and Near Infrared Radiometer

type2 (AVNIR-2), and Phased Array type L-band Synthetic Aperture Radar (PALSAR) (Osawa, 2004).

The PRISM sensor (Figure 44) consists of three independent telescopes for forward, nadir and backward view (side sensors are inclined ± 23.8° from the nadir radiometer) each of them with a 2.5 m nominal spatial resolution. Height accuracy is less than 5 m, even in cloud-capped areas by in-track optical sensors and/or SAR in conjunction with a highly stable attitude control system. These specifications are given to generate precise Digital Elevation Model (DEM). PRISM provides not only high resolution, but also wide swath image up to 70 km (35 km in triplet mode). The PRISM's three-mirror type optics has no chromatic aberration over wide field of view, giving clear and sharp images. ALOS is also capable of highly-accurate, ground control point (GCP)-free position and attitude determination (Osawa et al., 1998; Tadono et al., 2012).

JAXA is starting to process a detailed global DEM from ALOS acquisitions, but the project is still ongoing and products are not available yet. An application for research purposes was made and the specific digital surface model (DSM) of the site area has been provided (courtesy of Takeo Tadono of Japan Aerospace), with a resolution of 5 m. It has been generated stacking and mosaicking 17 triplet pair images (51 images in total). Since the vegetation is almost absent as well as the anthropogenic component, mainly because of the desert and semi-arid climate, DSM has been assumed to be a DEM.

Before its use, the ALOS PRISM DEM has required to be validated in comparison with more accurate elevation data, process (see 6.1), which has given good results, confirming that the digital model is quite accurate and can be applied for remote sensing analysis.

5.5. CGIAR SRTM 90 m digital elevation data

The SRTM is an interferometric SAR system that flew during 11-22 February 2000 aboard NASA's Space Shuttle Endeavour and collected highly specialized data about Earth's surface. (Henning et al., 2001). Subsequently, the collected data was processed and an accurate global DEM was generated, with a geometric

resolution of 1 arcsec for USA territories, (~30 m) and 3 arcsec for other countries (~90 m).

For the Alid geothermal field, a revised and corrected version of the SRTM DEM has been obtained from the CGIAR-CSI geoportal. Despite its relatively low spatial resolution, SRTM digital elevation data have a good vertical accuracy of less than 10 m and less "noise", thanks to the SAR technique and the short time acquisitions of the original data.

5.6. ASTER GDEM V2

The ASTER Global Digital Elevation Model (GDEM) was developed from stereoscopic acquisitions of ASTER VNIR band 3 sensor, with the aid of GCPs. It has 30 m horizontal resolution and a vertical accuracy of about 20 m. (Fujisada, 1994; Yamaguchi et al., 1998). It has been downloaded from the NASA Reverb geoportal. Despite its better spatial resolution, compared to SRTM DEM, it is less accurate: many artefacts are present on the digital surface, mainly due to the wide time interval in which stereo acquisitions were made.

5.7. National Eritrean DEM

The National Eritrean DEM reaches a resolution of 50 m and it is extracted from 1:25,000 national topographic maps. It has been kindly offered by Dr. Filmon Tesfaslasie. In the validation process, this DEM resulted unsuitable for mapping purposes because of the poor height accuracy.

5.8. Bing and Google maps imagery

Because of their very good resolution (less than 1 m), Bing and Gmaps images proved to be a valuable aid for the mapping activity, especially in these remote zones, where a fieldwork is not possible. Both services use commercial satellite images, like Quickbird or the Worldview series, and aerial views. These acquisitions have been downloaded from their portals, georeferenced and subsequently examined to extract geological and structural features.

5.9. National Eritrean geological map

The National Eritrean geological map has been kindly offered by the Eritrean Ministry of Energy and Mines and it is extracted from 1:25,000 (www.moem.gov.er).

5.10. USGS simplified geological map

The simplified geologic map of Duffield et. al (1996) has been used especially to check and validate results coming from remote sensing analysis and when satellite images could not give detailed information about rock lithologies or rock structures.

6. Remote sensing analysis - results

Before the mapping activity, an evaluation of ALOS DEM accuracy has been done, in order to use it. The following remote sensing analysis has been conducted in three main steps. At first, satellite acquisitions have been processed to provide material for the rock classification. The second part of the work consists in the visual analysis and the photointerpretation of satellite imagery. The last part of the study concerns with the normalization of the ground temperatures derived from ASTER TIR acquisitions.

6.1. ALOS DEM validation

To evaluate the height accuracy of the non-validated DEM derived by the spaceborne optical instrument PRISM and provided by JAXA heights have been compared with already validated digital data available and GCPs. The ALOS DEM altitudes are referred to the WGS84 ellipsoid Earth surface model, therefore, the first thing that has been done in order to compare it with other DEMs is to project it onto the EGM96 geoid, on which other heights are referred.

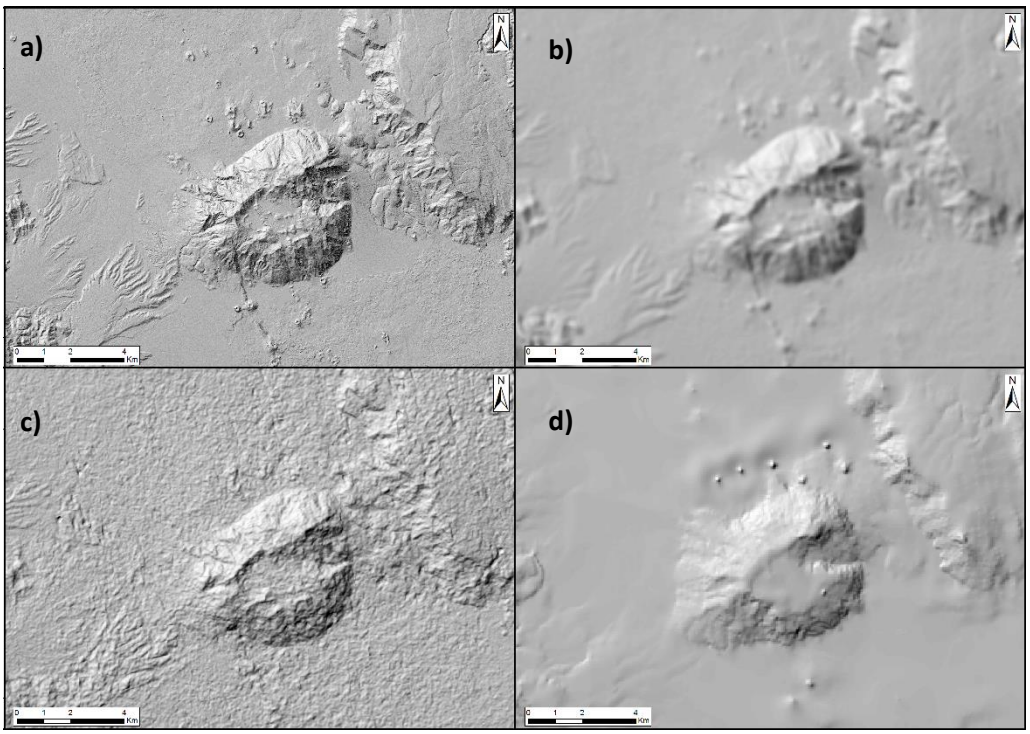

Figure 45. Comparison between the DEMs used for the validation process: a) ALOS, b) SRTM, c) GDEM, d) Eritrean DEM.

The datasets chosen for the validation process are three: CGIAR SRTM, ASTER GDEM V2 and tha National Eritrean DEM. A visual comparison of digital elevation data is shown in Figure 45.

SRTM DEM is very smooth, due to its good accuracy, but have a low spatial resolution, compared to other digital data (about 90 m). ASTER GDEM has a better resolution (30 m), but shows rough surfaces which may cause problem in the validation. The Eritrean DEM is the less accurate, despite its good resolution (50 m), because it was probably realized interpolating contour lines of old and inaccurate topographic maps: in fact, its surfaces appear very different compared to other data (e.g. the four artefacts on the north flank of the mountain, or the as well as the shape of the top). The ALOS DEM has a very good resolution and at a first look it seems to have a great accuracy, though it is not flawless.

In Figure 46 a slope map is shown, in which the first class, the one with values between 0° and 2°, is coloured in black. Through it, some strange perfectly flat areas have been highlighted, whose shapes matches exactly to the most recent basalt flows covering the Alid graben and they are probably missing-data zones. The reason for such errors is unknown and we do not know which factor may cause lack of signal in stereoscopic acquisitions.

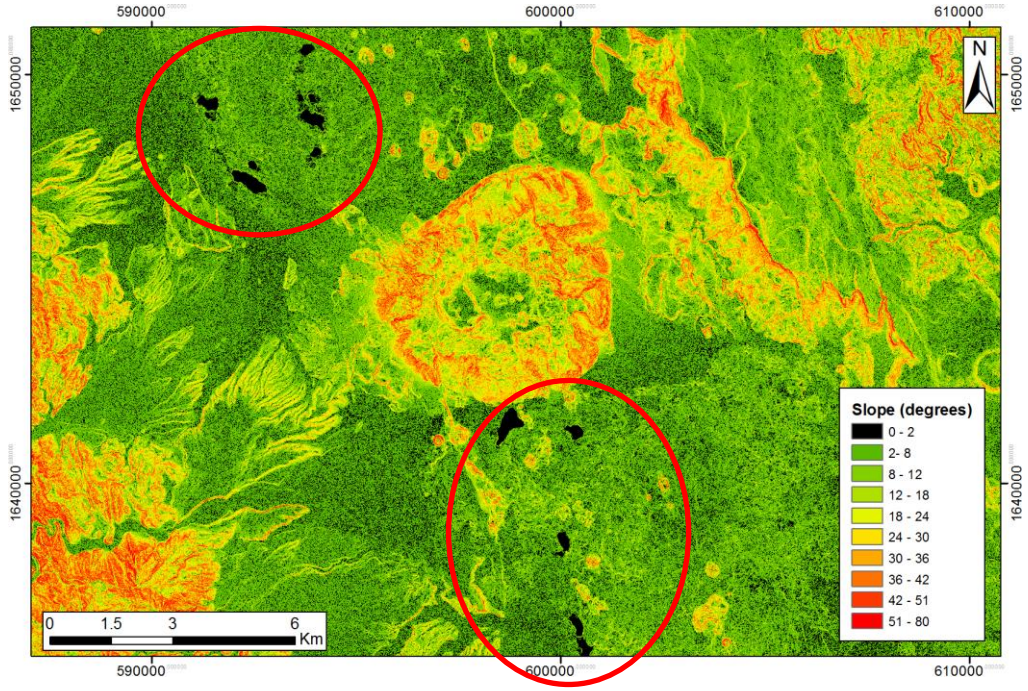

Figure 46. Slope map of the Alid graben. The red circles highlight ALOS missing-data zones.

The reference ground measures chosen for this purpose are the GPS point coordinates carried out by Teklesenbet during its 2012 geophysical campaign. They consist in two distinct sets of CGPs, respectively for TEM and MT soundings. The complete list can be found in the Appendix A and Appendix B.

A problem with height values of the TEM coordinates has been found. Since MT and TEM sounding are side by side, it is assumed they have a similar altitude on the average sea level, but there are a couple of points which have a quite different height.

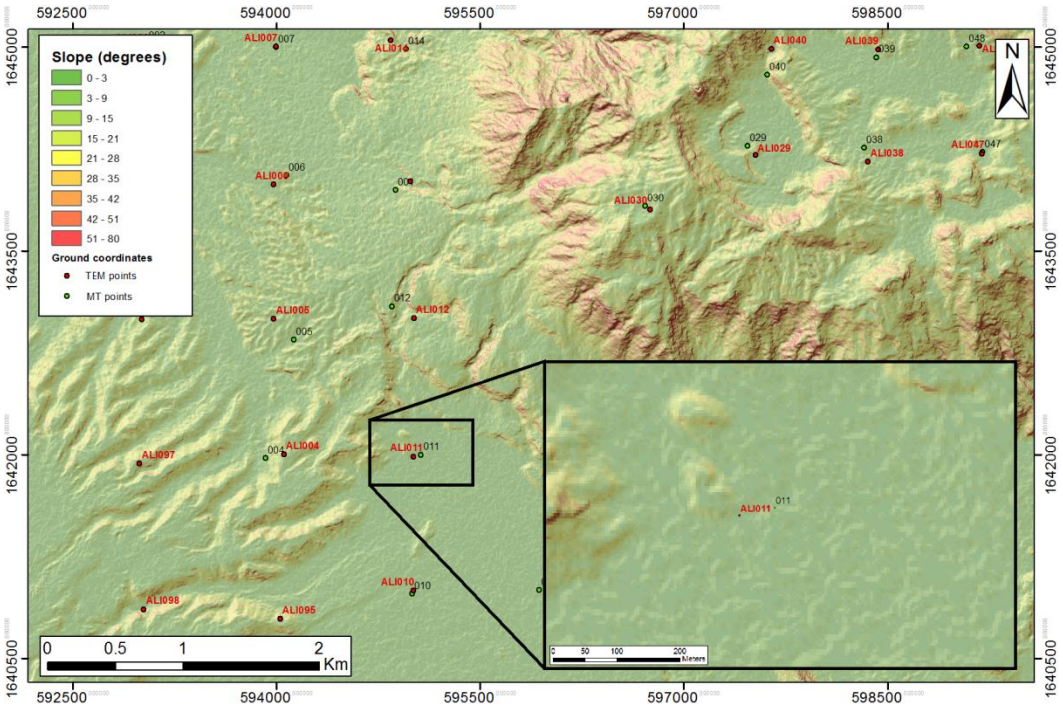

Figure 47. Slope map on which position of the ALI011 and 011 TEM-MT soundings is shown.

The most striking example is given in Figure 47: the two soundings in picture are 52 m far from each other, in a low slope area and approximately at the same altitude, but the given height of the TEM sounding (ALI011) is 148 m, whereas the MT sounding height (011) and the DEM height are respectively 175 and 176 m. This error is probably due to the different GPS trackers used for the two geophysical instruments. Therefore, it was decided to consider only the MT GCPs in the evaluation procedure and keep the TEM points only for a comparison.

Before taking into consideration the ALOS elevation data, SRTM GDEM and Eritrean DEM have been confronted with GCPs, to confirm their accuracy and choose the best datasets for the comparison with the ALOS DEM (Figure 48).

Elevation data	Bias error (m)	Standard deviation (m)	RMSE (m)
CGIAR SRTM	3.82	6.04	7.10
ASTER GDEM V2	-10.31	11.63	15.45
Eritrean DEM	37.82	38.87	53.96
PRISM DEM	0.78	3.30	3.36

Figure 48. Table in which height accuracy results between the four DEMs and the GCPs are shown.

As literature suggests, the absolute height accuracies of SRTM were in the ranges of 6.0 to 10.0 m of 90% error, -0.7 to 1.8 m (bias error), and 3.5 to 5.9 m (standard deviation) using kinematic GPS data on continental-scale validation campaign (Rodriguez et al., 2006), and the greatest errors were associated with steep terrain and very smooth sandy surfaces with low signal-to-noise ratio (SNR) such as deserts (Farr et al., 2007).

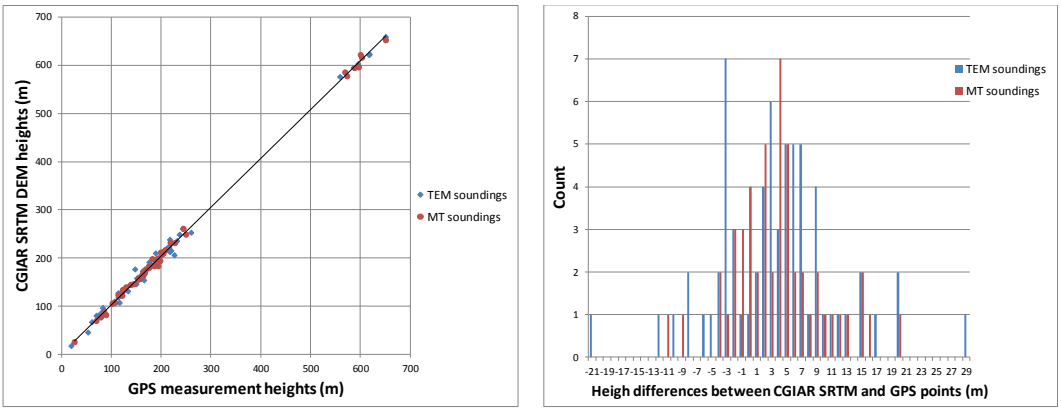

Figure 49. Height validation results coming from the comparison between the GCPS and the SRTM DEM.

Figure 49 shows a height validation result for SRTM. Height differences have a Gaussian distribution and these values present a slightly lower accuracy (see first row of the table in Figure 48), probably due to the two reasons previously listed. However SRTM is considered the most accurate digital model for the ALOS verification process.

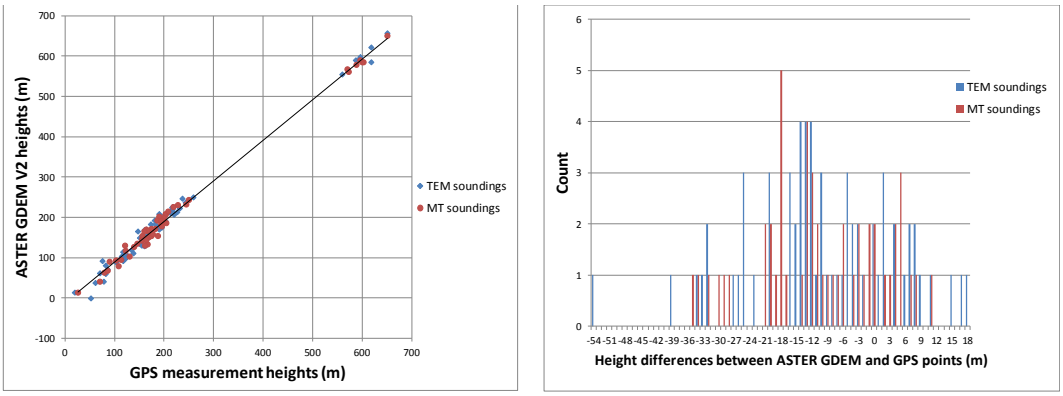

Figure 50. Height validation results coming from the comparison between the GCPS and the ASTER GDEM.

Validation results of ASTER GDEM are shown in Figure 50. Height differences have a relatively strange distribution, that may be related to its rough surfaces. Estimated errors (Figure 50) are worse than expected. According to Tachikawa et al. (2011), estimated errors for a DEM validation are within 7.4 m (bias), 12.7 m (STDEV) and 15.1 m (RMSE) for mountainous areas. Therefore, GDEM is not the best choice for evaluating ALOS accuracy.

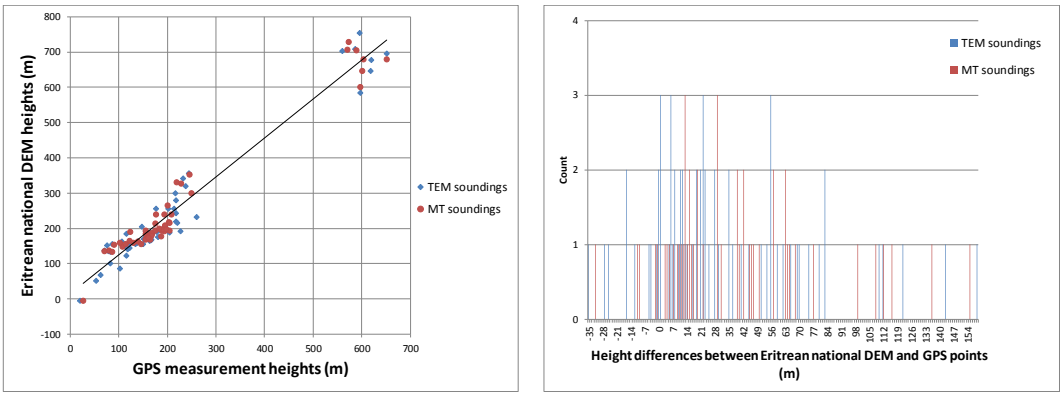

Figure 51. Height validation results coming from the comparison between the GCPS and the Eritrean DEM.

The National Eritrean DEM is the least accurate: Figure 51 shows a great dispersion of height differences, with extreme values of -35 and +154, and the given accuracy is of 37.82 m (bias), 38.87 m (standard deviation) and 53.96 m (RMSE).

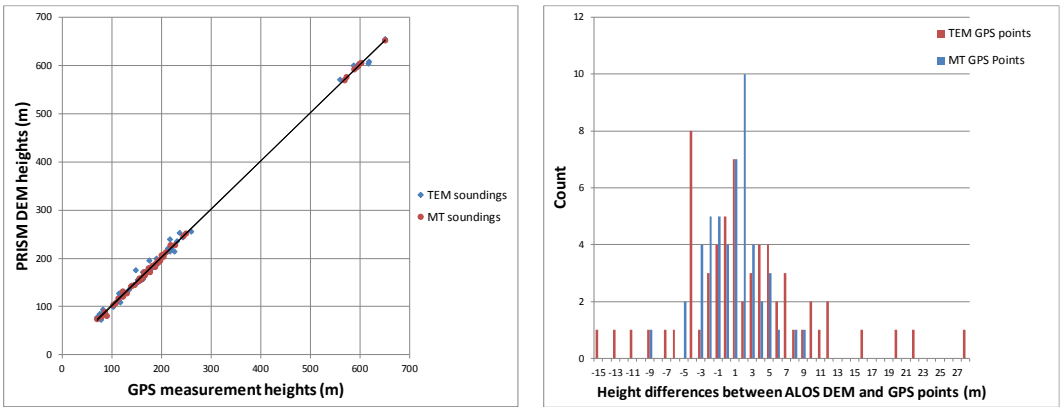

Figure 52. Height validation results coming from the comparison between the GCPS and the ALOS DEM.

The ALOS DEM is certainly the most accurate digital model. Figure 52 shows the linear relationship of height between digital data and GPS points. It confirms that the height accuracy for this DEM is within the expected ranges (Tadono et al., 2012) with values of 0.78 m (bias), 3.30 (standard deviation) and 3.36 (RMSE).

For a graphical evaluation of ALOS accuracy, a large scale height validation has been conducted both with SRTM and GDEM. After a resample of the SRTM and GDEM, bringing them to the ALOS resolution (5 m) and having clipped their size to the same size, two new raster have been generated, simply subtracting from the ALOS DEM the two other already validated digital data (see Figure 53 and Figure 54).

In these maps, the white colours represent areas in which the height difference is around 0 m, while red and blue graduations correspond to areas with +/-100 m differences, and more than +/-100 m filled in red and blue, respectively. ALOS and SRTM flat areas show large coherence and confirm that the ALOS DEM is very accurate and ready to be used for the mapping activity. Instead, as expected, the greater differences appear to be the steep flanks of Alid mountain, the eastern scarp fault and the western highlands. This is simply due to the lower SRTM resolution. The subtraction with SRTM gives an accuracy of 0.54 m (mean) 12.26 m (standard deviation) and 12.33 m (RMSE), while the minimum and maximum values are -103.50 m and 115.20 m, respectively.

As stated previously, GDEM has given worse results since there is no coherence, even in flat surfaces, mainly because its "bumpy" surface gives low accuracy and therefore it cannot be used for validation.

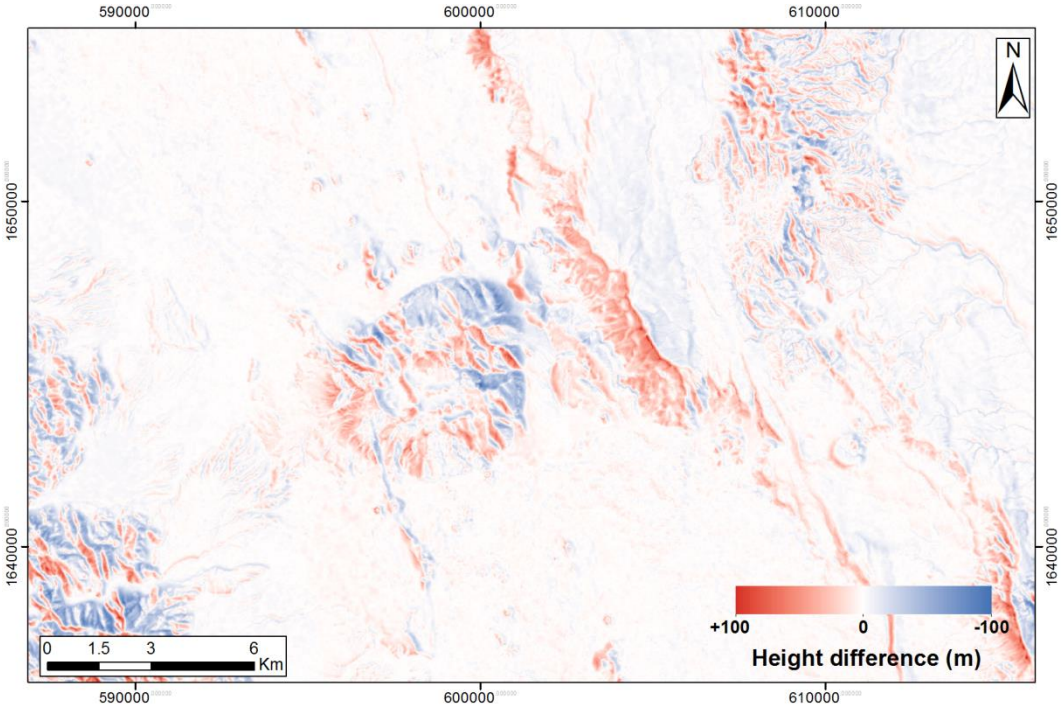

Figure 53. Height differences between the ALOS DEM and the SRTM.

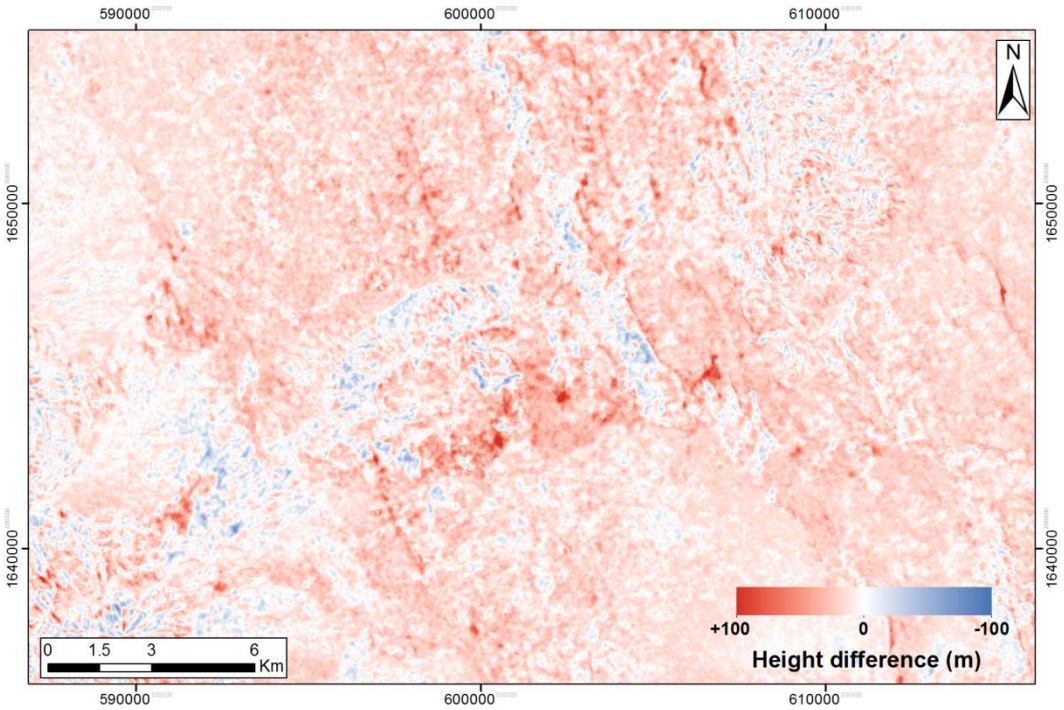

Figure 54. Height differences between the ALOS DEM and the ASTER GDEM.

6.2. Preprocessing of Landsat 8 images

All Landsat 8 images have been preprocessed and analyzed in ENVI, which is one of the most famous softwares used to process and analyze geospatial imagery.

The standard Landsat 8 products provided by the USGS EROS Centre consist of quantized and calibrated scaled Digital Numbers (DN), in 16-bit unsigned integer, representing multispectral image data acquired by both the OLI TIRS. Before processing them, DN must be scaled to the reflectance and radiance using radiometric rescaling coefficients provided in the product metadata file, in a process called **Radiometric Calibration**. In ENVI, the following equation is applied to the image:

$$L_\lambda = M_L Q_{cal} + A_L$$

where L_λ is the spectral radiance, M_L is a band-specific multiplicative rescaling factor taken from the metadata, A_L is a band-specific additive rescaling factor taken from the metadata and Q_{cal} is the quantized and calibrated standard product pixel values (DN).

After having calibrated the radiance at sensor, Landsat data has been corrected from undesired atmospheric effects, such as absorption, reflection and diffusion of the incoming electromagnetic radiation. Moreover, the atmospheric correction is able to convert the radiance values into the corresponding reflectance percentage.

The **Fast Line-of-sight Atmospheric Analysis of Hypercubes** (FLAASH) is a first-principles atmospheric correction tool that corrects wavelengths in the visible through near-infrared and shortwave infrared regions, up to 3 μm. FLAASH starts from a standard equation for spectral radiance at a sensor pixel, *L*, that applies to the solar wavelength range (thermal emission is neglected) and flat, Lambertian materials or their equivalents. The equation is as follows:

$$L = \left(\frac{A\rho}{1 - \rho_e S}\right) + \left(\frac{B\rho_e}{1 - \rho_e S}\right) + L_a$$

where ρ is the pixel surface reflectance, ρ_e is an average surface reflectance for the pixel and surronding region, S is the spherical albedo of the atmosphere, $L_a$is the radiance backscattered by the atmosphere, A and B are coefficients that depend on atmospheric and geometric conditions but not on the surface (Matthews et al, 2000).

The values of A, B, S and L_a are determined from code calculations, which uses the viewing and solar angles and the mean surface elevation of the measurement, and they assume a certain model atmosphere, aerosol type, and visible range.

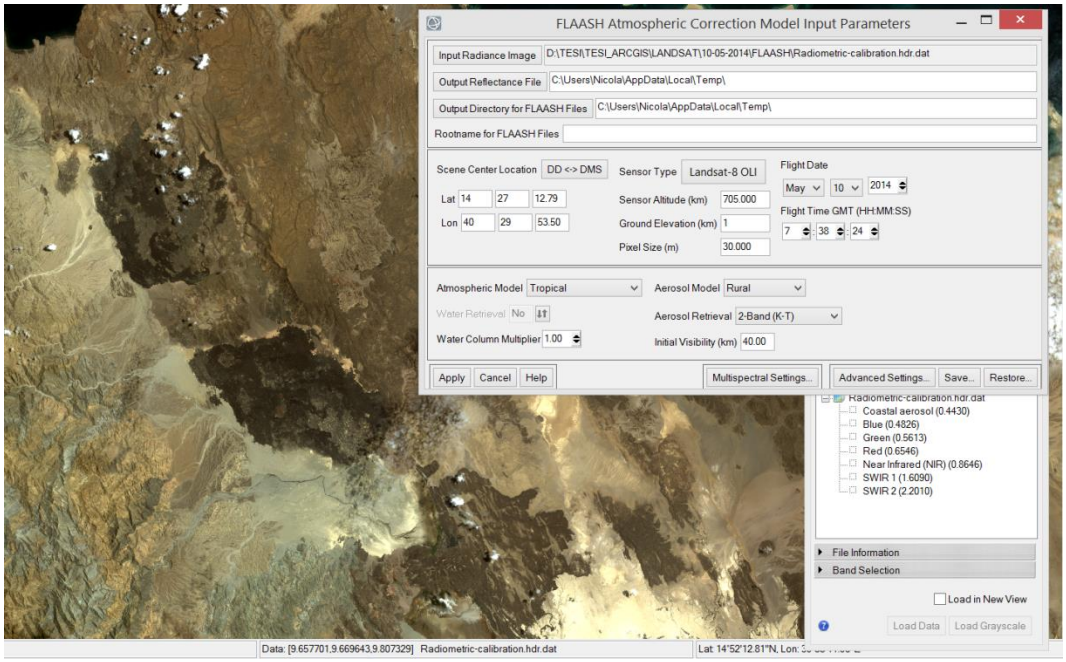

Figure 55. The FLAASH atmospheric correction tool and the required input parameters. In background, a Landsat 8 image centered on the Alid complex.

The input image for FLAASH must be a radiance image in band-interleaved-by-line (BIL) or band-interleaved-by-pixel (BIP) format. After having imported it, scene and sensor details must be assigned in order to give FLAASH an approximation of the sun's position relative to the surface (Figure 55). The required information are latitude and longitude, sensor type and altitude, flight date and acquisition time, pixel size and average ground elevation.

Besides the atmospherically corrected reflectance image, FLAASH creates an image of column water vapor in units of (atm * cm) and a cloud map classification image. To perform the correction, the average value of visibility must be indicated as well as the atmospheric model, which better approximates such coordinates and season, and the aerosol model.

6.3. Landsat 8 false colour compositions

To facilitate the mapping activity described in the next paragraphs, some operations have been done with the Landsat 8 images. One of these is the RGB (Red Green and Blue) combination of spectral band, which is the term used to refer to the assignment of colours to represent brightness in different regions of the electromagnetic spectrum. It consists of giving each band one of the three different addictive colours, which are red, green or blue. In this system, different colours are generated by additive combinations of these three components. For instance, if the red, green and blue bands of a multi-spectral image are displayed in red, green and blue simultaneously, a **true colour composite image** is generated. For the Landsat 8 OLI sensor, this RGB composition is made with band 4, 3 and 2, respectively.

Bands	Wavelength (micrometers)	Resolution (meters)
Band 1 - Coastal aerosol	0.43 - 0.45	30
Band 2 - Blue	0.45 - 0.51	30
Band 3 - Green	0.53 - 0.59	30
Band 4 - Red	0.64 - 0.67	30
Band 5 - Near Infrared (NIR)	0.85 - 0.88	30
Band 6 - SWIR 1	1.57 - 1.65	30
Band 7 - SWIR 2	2.11 - 2.29	30
Band 8 - Panchromatic	0.50 - 0.68	15
Band 9 - Cirrus	1.36 - 1.38	30
Band 10 - Thermal Infrared (TIRS) 1	10.60 - 11.19	100 * (30)
Band 11 - Thermal Infrared (TIRS) 2	11.50 - 12.51	100 * (30)

Figure 56. Landsat 8 spectral bands, with their spectral interval and spatial resolution (Source: nasa.gov).

With multispectral images, different band combinations can give more information than a simple natural colour image. For example, the NIR wavelength is one of the most commonly used wavelengths on multispectral sensors because vegetation reflects so strongly in this portion of the electromagnetic spectrum, which is very useful when performing vegetation analyses. Instead, the SWIR bands are very useful for discerning lithological differences and for identify wet surfaces, because in this spectral interval there there is the maximum variability of soil brightness.

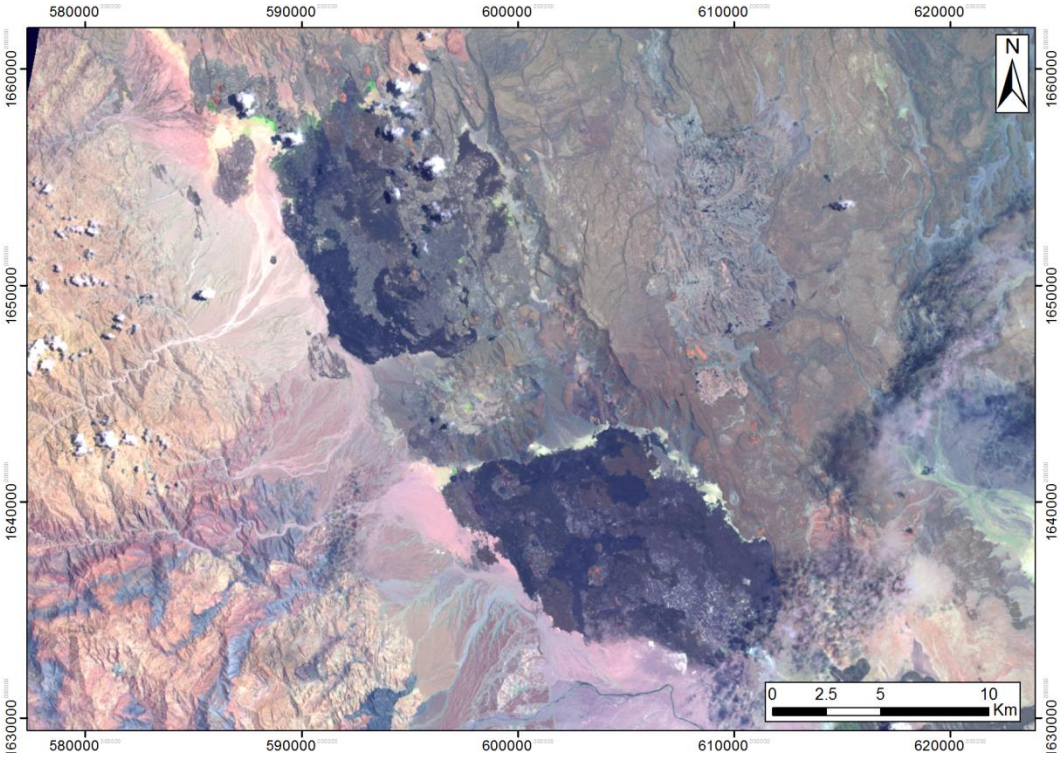

Figure 57. Landsat 7-5-3 false colour composition.

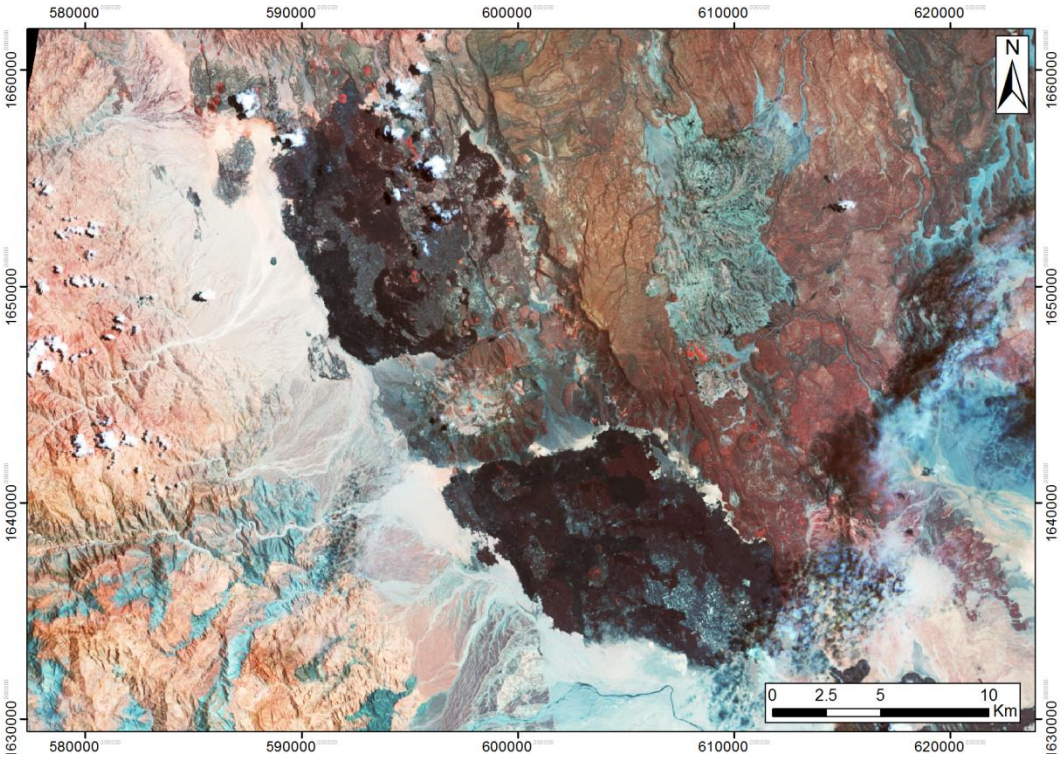

Figure 58. Landsat 6-3-2 false colour composition.

Shown below are the Landsat 8 band combinations performed, whilst all Landsat 8 bands mentioned are listed in Figure 56.

7-5-3 combination (Figure 57) uses one region from the SWIR region, one from NIR, and one from the visible spectrum and it is called Landsat Geocover, because it is indicated for geological purposes. Bright green areas represent healthy vegetation, pink areas are arid soil, oranges and browns represent sparsely vegetated areas. In desert landscapes, sands, soils and minerals are highlighted in a multitude of colours, therefore this band composition provides striking imagery for desert regions, like the Eritrean Lowlands. This combination has been employed for geological analysis, as differing soil minerals can be distinguished.

6-3-2 combination (Figure 58)is good for discerning variations in a landscape that do not contain abundant vegetation, like deserts, and it is good for geologic applications. This composition has really highlighted some lithological contrasts and it has been used for geological mapping of certain rock units, like the alluvial deposits around the Alid flanks.

7-6-5 combination (figure 59) can be useful for geological studies, since uses three bands from outside the visible region. It may be used to find textural and moisture characteristics of soils. In these images, blue spots represent vegetation. Because it employs longer wavelengths, it is free of effects of atmospheric scattering. Since in the Alid graben humidity rate reaches even 90%, this combination has been heavily employed and it has been resulted helpful for mapping the Precambrian basement outcropping on the top of Mi Alid.

6-5-4 combination (Figure 60) uses NIR, SWIR, and red bands and provides the user with a great amount of information and color contrast. Healthy vegetation is bright green and soils are mauve. It is also sensitive to variations in soil moisture and is useful for analysis of soil and vegetation conditions, because wetter soils appear in darker tones. Through this combination, the altered basement which outcrops at the top of Mt Alid appears very clearly in pink tones.

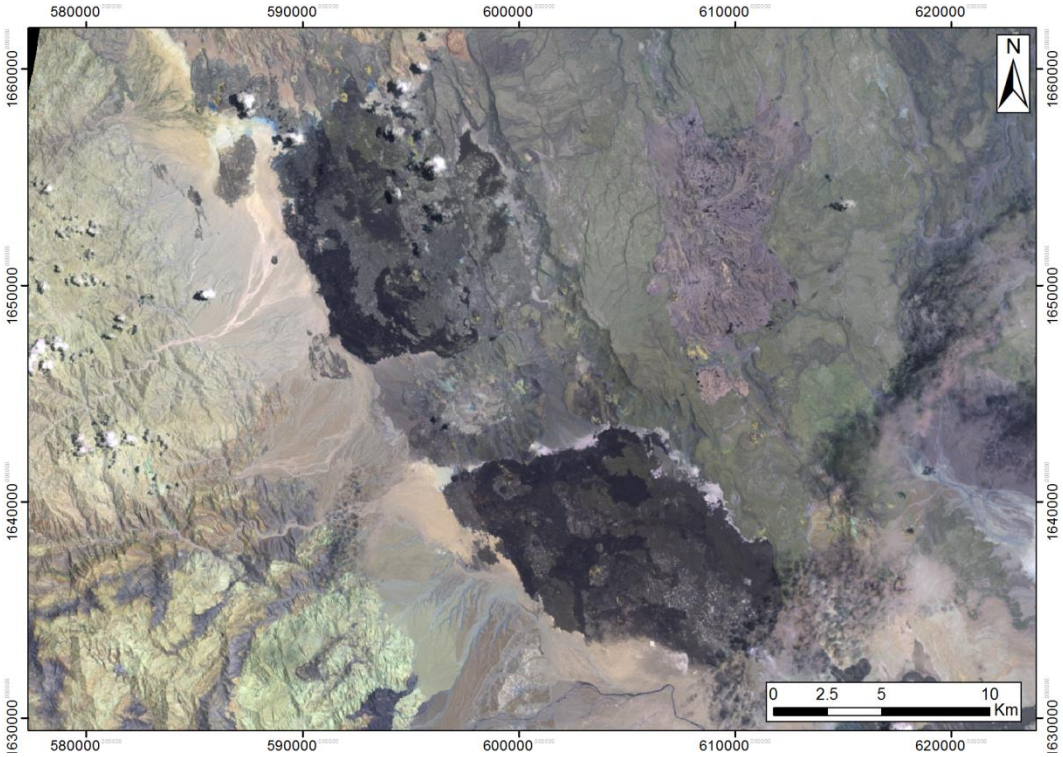

Figure 59. Landsat 7-6-5 false colour composition.

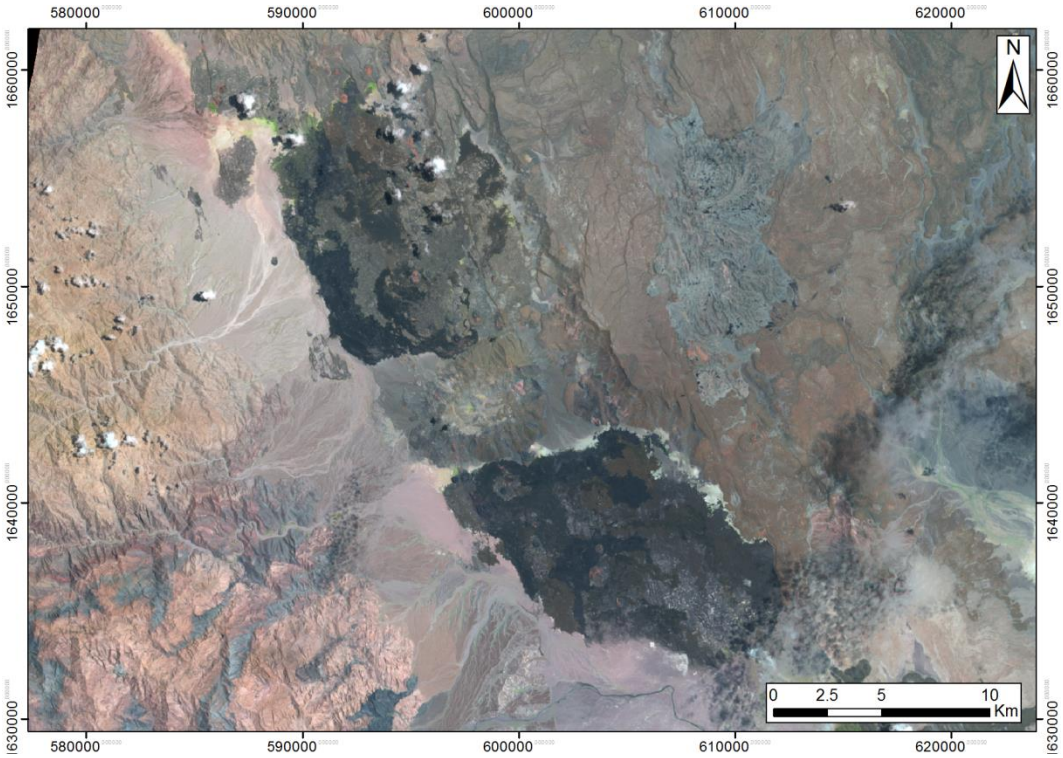

Figure 60. Landsat 6-5-4 false colour composition.

6.4. Supervised Classification

The classification process is the statistical analysis of the remote sensing image data by which pixels are considered to belong to a certain class, in view of their spectral characteristics. It is considered a quantitative analysis because of its ability to identify pixels based upon their numerical properties and owing to its ability for counting pixels for area estimates.

The classification workflow uses either unsupervised or supervised methods to categorize image pixels into many classes, unsupervised if training data is not provided, or supervised classification, training data is given and a classification method (maximum likelihood, minimum distance, distance, or Spectral Angle Mapper) is specified.

In this instance, maximum likelihood classification has been chosen, which is the most common supervised classification method used with remote sensing image data. It assumes that the statistics for each class in each band are normally distributed and calculates the probability that a given pixel belongs to a specific class. Unless a probability threshold is selected, all pixels are classified. Each pixel is assigned to the class that has the highest probability.

ENVI implements maximum likelihood classification by calculating the following discriminant function for each pixel in the image (Richards, 1999):

$$g_i = \ln p(\omega_i) - \frac{1}{2}\ln|\Sigma_i| - \frac{1}{2}(x - m_i)^t \Sigma_i^{-1}(x - m_i)$$

where i is the class, x the n-dimensional data (where n is the number of bands), $p(\omega_i)$ is the probability that class ω_i occurs in the image and is assumed the same for all classes, $|\Sigma_i|$ is the determinant of the covariance matrix of the data in class ω_i, Σ_i^{-1} is the inverse matrix and m_i is the mean vector.

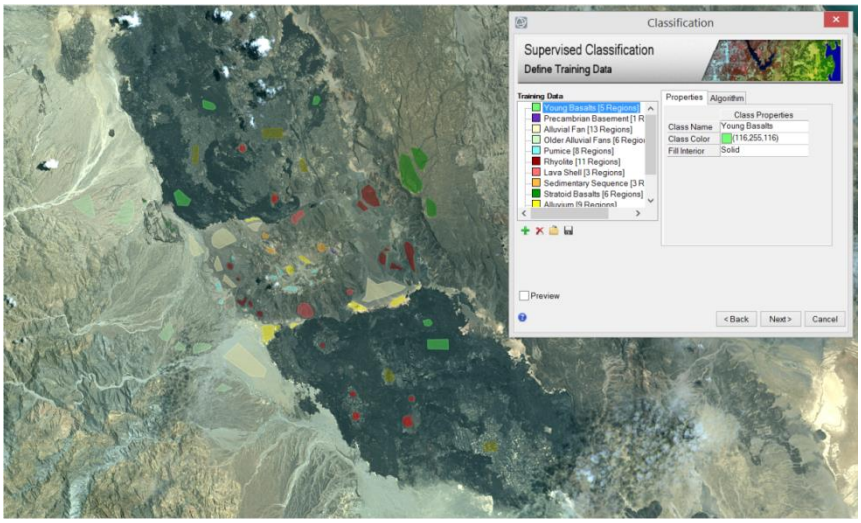

Figure 61. ROI related to the supervised classification process.

A subdivision into 12 classes has been performed and, for each class, a certain number or Regions of Interest (ROI) has been defined (figure 61), in order to extract statistics for the classification process. Once applied to each pixel the previous equation, the classification map is generated. Several maps have been produced, using all the Landsat 8 images available. One of the best results is shown in Figure 62.

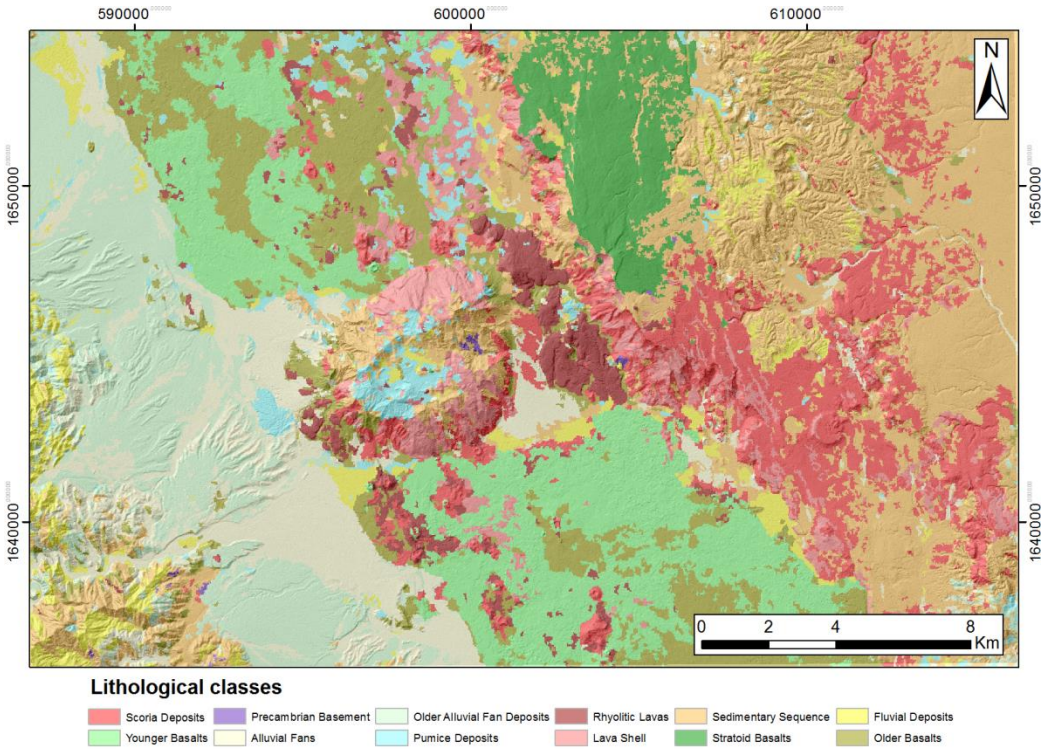

Figure 62. Lithological classes derived from the supervised classification process.

The classification has given good results and, in general, also a good coherence with visual interpretation. For example, old and actual alluvial fan deposits appear clearly and different types of volcanic effusions have been discriminated in the basaltic fields. On the Alid flanks, the results fit very well with the preliminary geological survey conducted by Duffield et al. (1996), therefore they have been helpful for the delineation of different lava flows deposits and the Precambrian basement outcrops in the Ilegedi thermal area. The classification has been successful also on the eastern scarp of the graben, where some basement outcrops have been highlighted. Only on the eastern horst results have been considered unsuccessful. This lack of coherence was expected, since in this area ROIs were not defined due to the lack of information about local lithologies.

6.5. ArcGIS geodatabase realization

After having processed in ENVI the Landsat 8 images, the previously obtained results have been imported in a geodatabase. In addition to them, all the cartographic material provided by Duffield et al. (1996), the resistivity maps developed by Eysteinsson et al. (2010) and Teklesenbet (2012), Bing and Google images and the digital elevation models, including the ALOS DEM, have been added to the database.

Part of the listed material has been georeferenced, such as Bing and Google images and the iso-resistivity maps. Moreover, the USGS geological and structural maps have been subjected to an orthorectification process, since they are based on photogeologic analysis of 1:60,000 scale aerial photographs.

6.6. Geological map

One of the main results obtained from the remote sensing analysis has been the realization of an improved geological map, compared to the previous version. To achieve this result, the mapping activity has been performed with the aid of the USGS orthorectified geological map. Because it was originally affected by a strong perspective distortion and because no topographic map was used for its realisation, contacts between the different lithological units and tectonic

lineaments are strongly inaccurate, especially far from the Alid dome, where the deformation is maximum. Nevertheless, the 1:60,000 map scale makes it unsuitable for any type of field activity, especially for a possible geothermal exploration campaign.

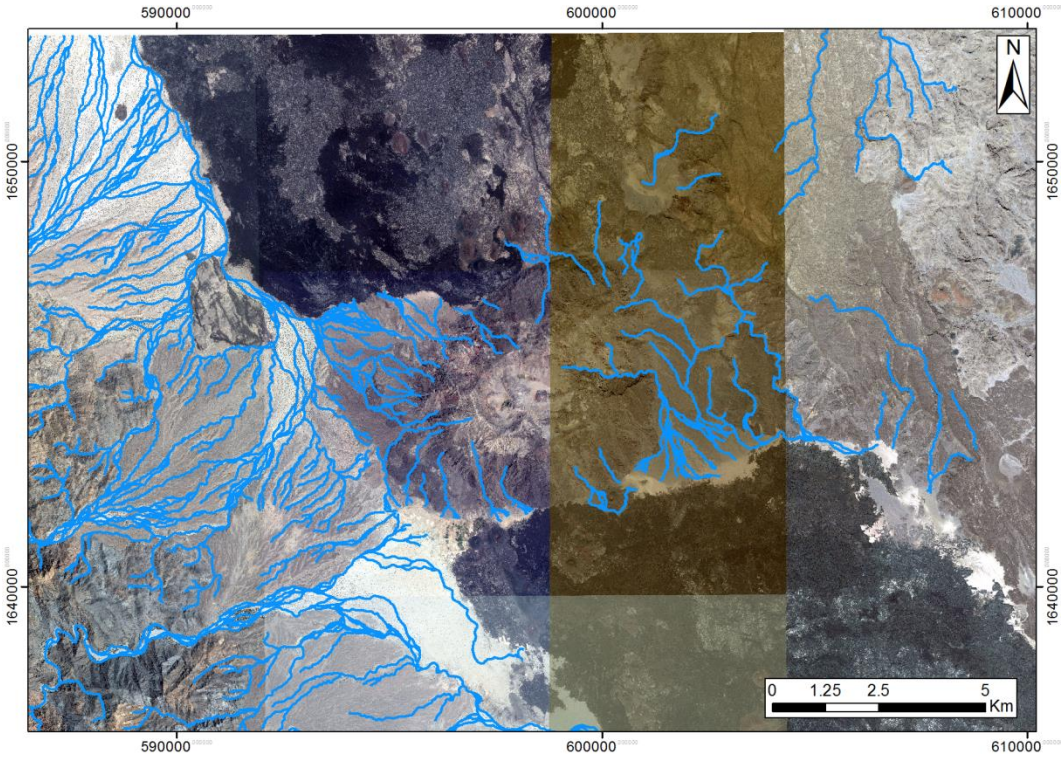

Figure 63. Surface drainage map of Alid and surrounding.

First of all, a morphotectonic analysis of the stream network has been done, interpreting images and drawing the main **surface drainage map**, in order to highlight tectonic lineaments from river channel anomalies or deviations (Figure 63). As a matter of fact, the analysis of drainage systems allows the detection of tectonic activity, because fluvial systems are very sensitive to changes in the parameters that control their shape and slope. Rivers tend to develop equilibrium profiles in

Figure 64. An example of a structural lineament deducted from the surface drainage analysis.

relatively short times, and consequently, anomalies in the river network systems can be considered recent tectonic activity (Sheidegger, 2004).

This analysis has been useful especially in the western scarp of the graben, where hydrography is well developed and assumes a trellis geometry. In Figure 64 an example of anomaly in the river course is shown. It has been interpreted as one of the NNW-SSE synthetic normal faults which form the western slope of the Alid graben, with a possible dextral strike-slip component.

With the aid of the previous analysis and in cooperation with Dr Montanari of the IGG-CNR research institute, the mapping of the **tectonic lineaments** has been made (Figure 65).

Two main tectonic trends characterize the Alid complex: a NNW-SSE normal fault trend, controlled by the Regional tectonic setting , and a local NE-SW strike-slip trend, which characterizes the volcanic structure and is probably caused by the dome uplift. This lineaments have been interpreted as the product of a dextral shear zone, which accommodates differential crustal extension rates resulting from the progressive northward increase of amount of extension (Acocella, 2014). The astenospheric plume, which fed the quaternary volcanic activity and currently heats the geothermal reservoir, probably moved upward along this structural weakness, stopping at 4-5 km b.s.l.. The NE-SW elongated shape of Mt. Alid could be due to this mechanism.

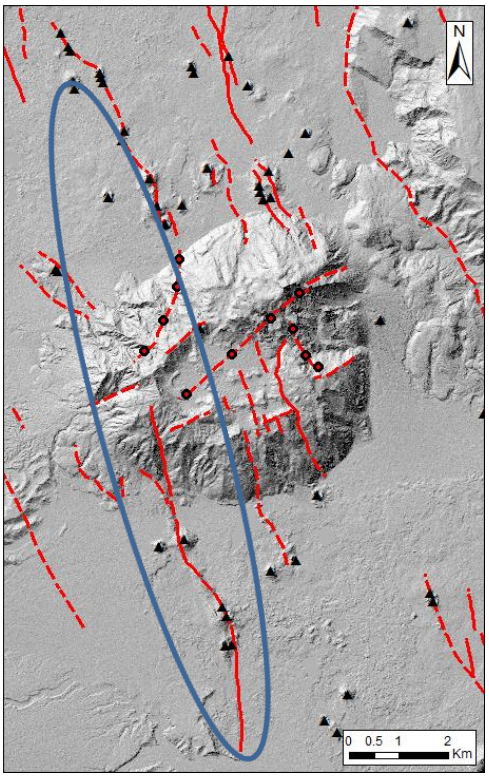

Figure 65. The structure circled with the blue line has been interpreted as a normal fault which is subjected to a dextral shift under the Alid dome.

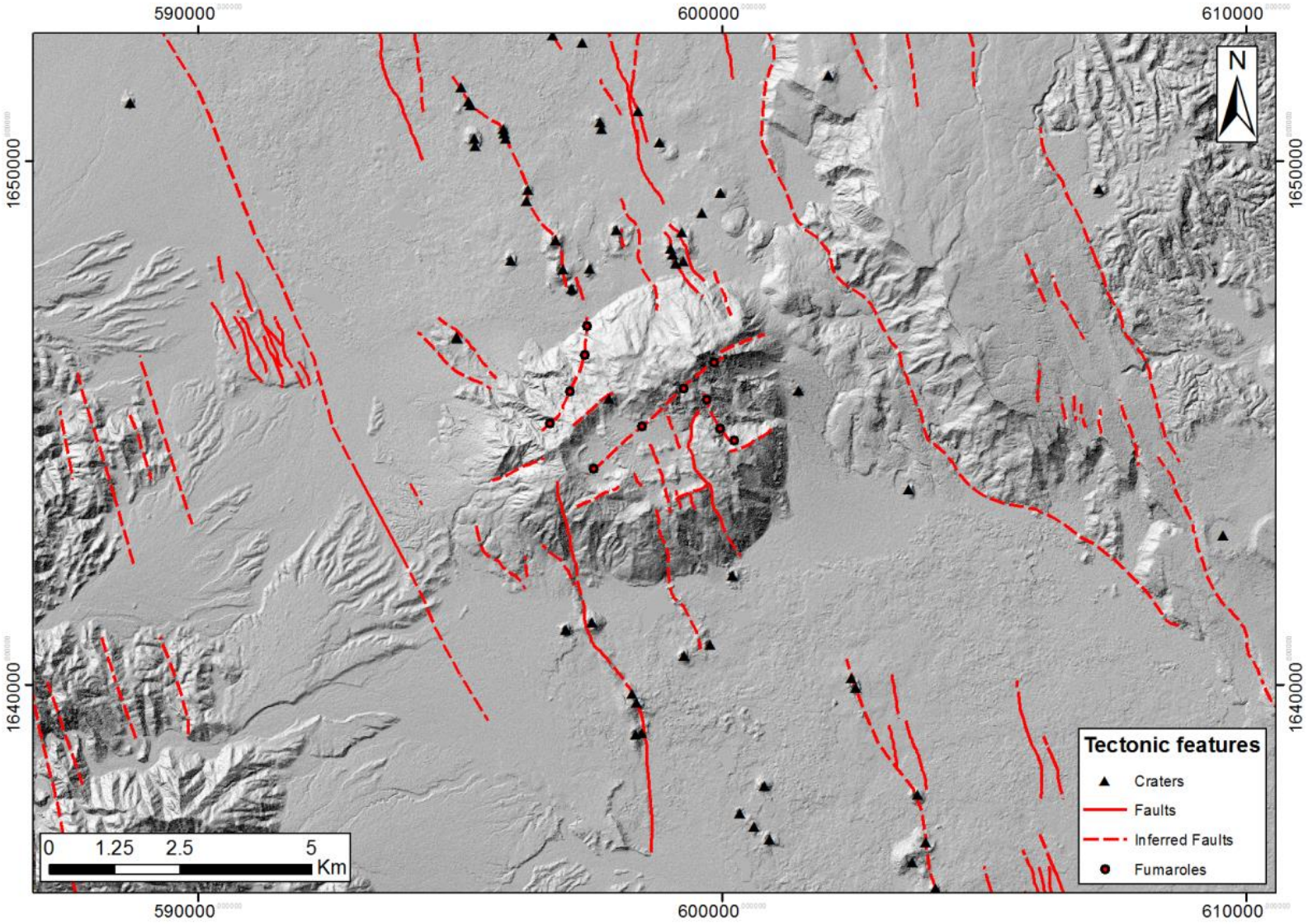

Figure 66. Structural map of the Alid volcanic center and surrounding.

The structural map also shows the crater's position. Scoria cones, which can be found in the two basalt fields, appear aligned along the NNW-SSW structural lineaments, because conjugated normal faults probably act as preferential ways for the ascent of basaltic lavas.

Even the coordinates of the fumaroles coordinates have also been represented, because their position seems to be controlled by structural mechanisms. The fumaroles in the collapsed zone follows the NE-SW local tectonic while the three eastern fumaroles are connected with the NNW-SSE Regional tectonic trend.

The four fumaroles on the northern flank of Mt. Alid follow an interesting pattern. They appear aligned on a shifted NNE-SSW lineament and could have originated from the interception between the two main structural trends. These four steam vents also appear connected with the NNW-SSE tectonic structure circled in Figure 66: it seems that the shear zone shifted the fracture clockwise and, consequently, brought the formation of the northern fumaroles.

Finally, the **lithological mapping** has been conducted (Figure 67). Rock units have been mapped at an average scale of 1:2000. The images used for lithological unit delineation are: the Bing and Google imagery, the supervised classification maps and the Landsat false colour compositions. The ALOS DEM has represented a valid help for the mapping purpose: through its processing hillshades and slope maps have been derived from it, giving useful information for mapping especially low relief landforms (such as older alluvial fan deposits) and define the exact position of scarps and topographic variation. The preliminary geological map, realized by Duffield et al. (1996) and previously referenced, has been used for validation or for those parts in which satellite images were not clear.

The thirteen lithological units reflect the rock classification of Chapter 2 with some modifications. Scree class has been added, to map the talus deposit constituting the eastern scarp of the graben. The basaltic lavas which fills the bottom of the graben have been split in two different units: basalts partially filled with aeolian deposits and young basalts. The analysis of the ALOS DEM has revealed that these basalts, previously mapped by Duffield et al. (1996) as a homogeneous rock unit, are actually made by two different deposits: older

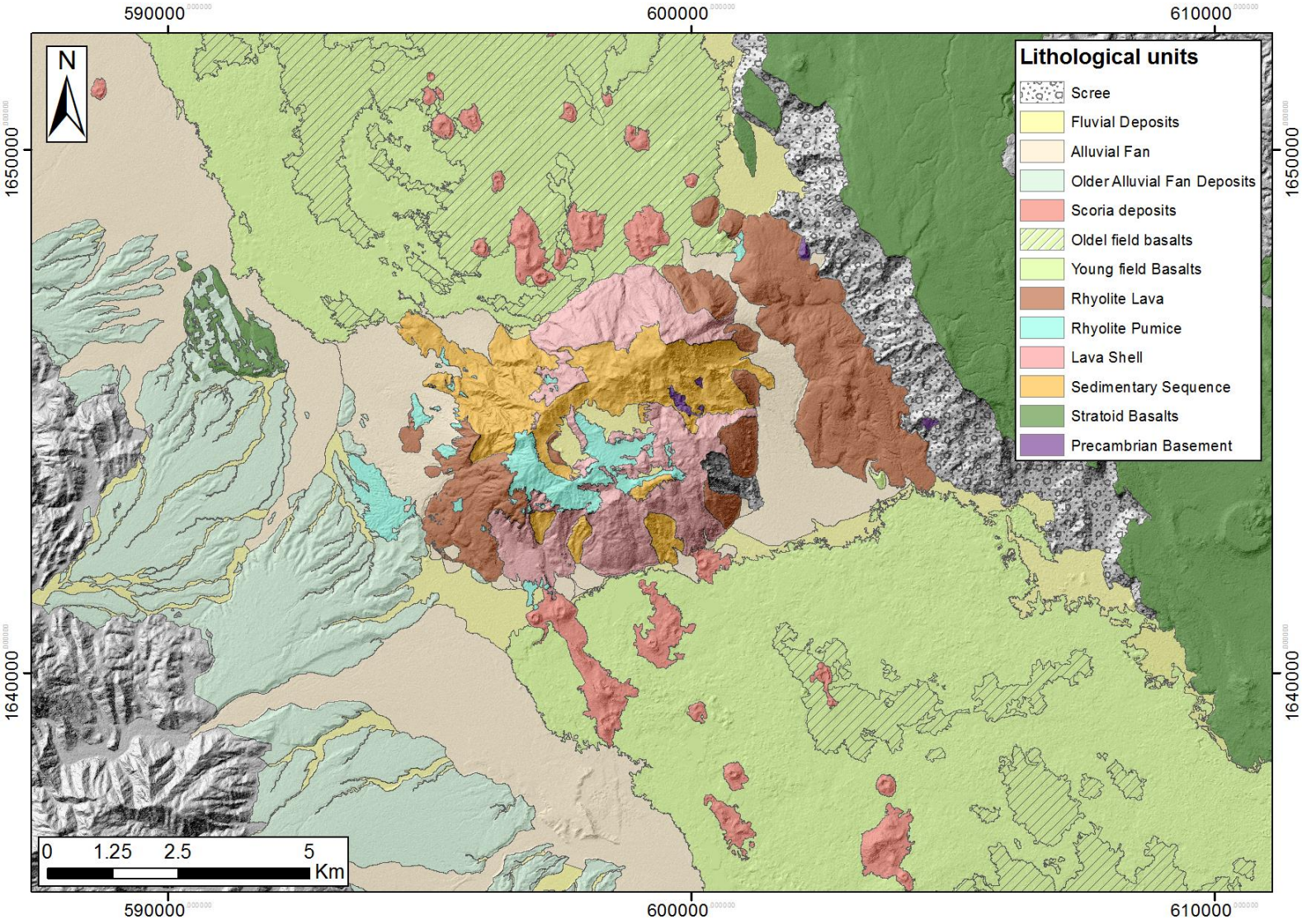

Figure 67. Geological interpretation of the Alid graben.

aeolian-filled basalts and younger basalt flows, which overlies partially the older deposits. A modified version of the Riley's Topographic Rugged Index (1999) has been calculated: the difference between the two type of basalts is very sharp, because the older aeolian-filled deposits are smoother than the younger basalts, for which the index assumes a greater value (Figure 68).

From the photointerpretation map the dextral shear zone underlying the Alid dome is evident: the position of scoria cones is a clear marker of the dextral strike-slip component explained above.

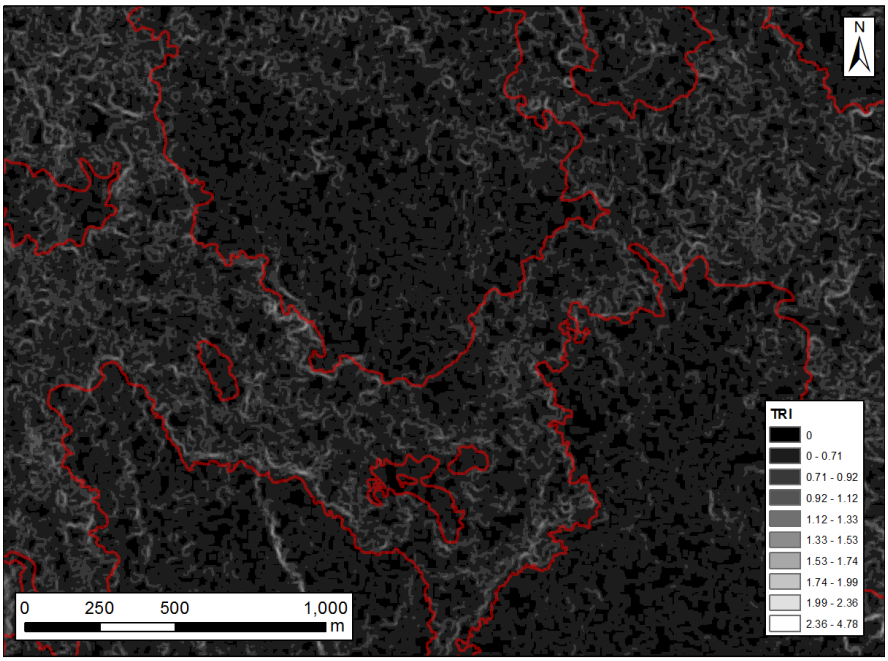

Figure 68. Analysis of the modified Terrain Ruggedness Index. The red line shows the boundary between the two basaltic flow types.

6.7. Processing of ASTER images and thermal analysis attempt

A first attempt to analyse thermal images and isolate Alid's surface geothermal anomalies has been done. Eight ASTER L1B datasets have been examined, two day acquisitions and six night scenes. Only winter acquisitions, taken from 2011 to 2014 from, have been chosen for this kind of analysis, in order to reduce the effect of solar radiation and therefore the high thermal inertia of local rocks. As a matter of fact, during summer, daily round temperature can exceed 50 °C.

In ASTER Level 1B data, the raw digital counts of Level 1A data are converted to radiance values, and a transformation has been applied to register the image to a coordinate system. Therefore, no radiometric calibration is needed.

Aster images have been imported into ENVI and, before processing them, atmospheric correction has been applied, in order to approximate and remove the atmospheric contributions from thermal infrared radiance. The **Thermal Atmospheric Correction** (TAC) tool has been used.

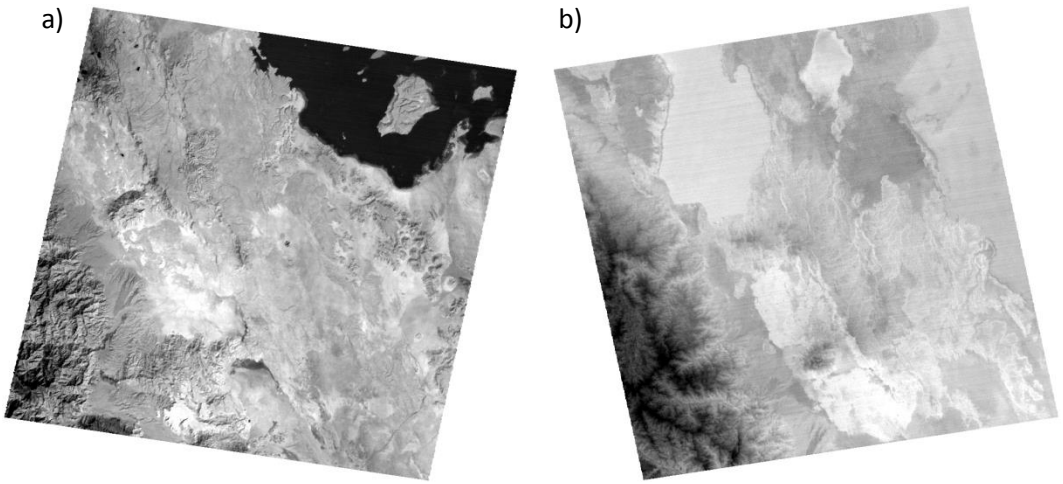

Figure 69. Day (a) and night (b) TIR ASTER band 10 greyscale images.

Once the TAC has been performed, emissivity and brightness temperature have been calculated. In fact, the radiation emitted from a surface in the thermal infrared wavelengths is a function of both the surface temperature and emissivity. Through the ENVI **Emissivity Normalization** tool, this operation has been performed. The emissivity normalization technique calculates the temperature for every pixel and band in the data using a fixed emissivity value. Then, the highest temperature for each pixel is used to calculate the emissivity values using the Planck function.

The comparison between day and night radiance and brightness temperature has shown that day TIR acquisition are influenced by aspect, which causes positive anomalies in brightness and temperature of south-facing slopes. Night TIR are also affected by altitude effects, since in night acquisitions peaks show

negative radiance or temperature anomalies. Moreover, images reveal a strong lithological influence in the distribution of temperatures.

To better emphasize thermal anomalies of the Alid top surface, other treatments must be done, in order to remove, or at least reduce, the previously listed effect. The day TIR acquisition have been discarded, only night scenes have been taken into account for the thermal analysis, since they are much less affected by the aspect effect. Then, a "**spatial temperature normalization**" has been applied to TIR images, which consist of applying to the pixel value temperature a scale factor, function of the topography. The results are corrected for a temperature gradient based on a normal lapse rate.

The environmental lapse rate (ELR) is the rate of decrease of temperature with altitude in the stationary atmosphere at a given time and location. As an average, the International Civil Aviation Organization (ICAO) defines an international standard atmosphere (ISA) with a temperature lapse rate of 6.49 K(°C)/1,000 m from sea level to 11 km. Therefore , the value 0.0065 °C/m has chosen, as Warner and Chen suggest (2011).

Since the ASTER TIR images have a 3 arcsec spatial resolution (about 90 m), the SRTM DEM, which has the same resolution, has been chosen for calculating the temperature gradient. Then, using the Raster Calculator Toolbox, the SRTM pixel values have been multiplied by the average lapse rate. The output raster have finally added to the TIR scenes, obtaining a temperature normalization.

The comparison between unprocessed and normalized TIR images (Figure 70) shows that temperature variation has been smoothed and the lithological control of thermal emissions seems to have strongly decreased. Besides, the height thermal anomalies have been reduced, especially on the Alid top.

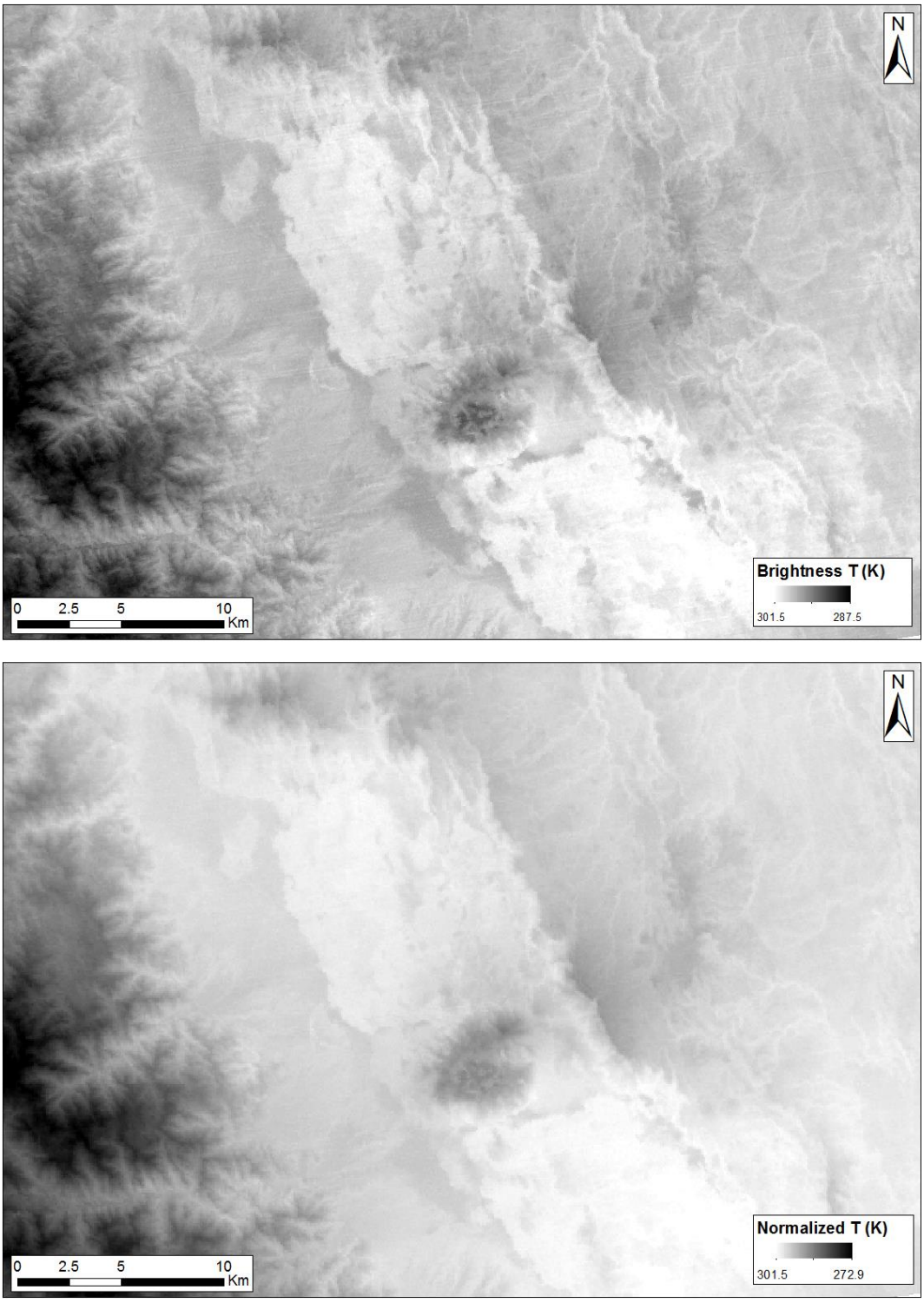

Figure 70. Comparison between unprocessed brightness temperatures and normalized temperatures.

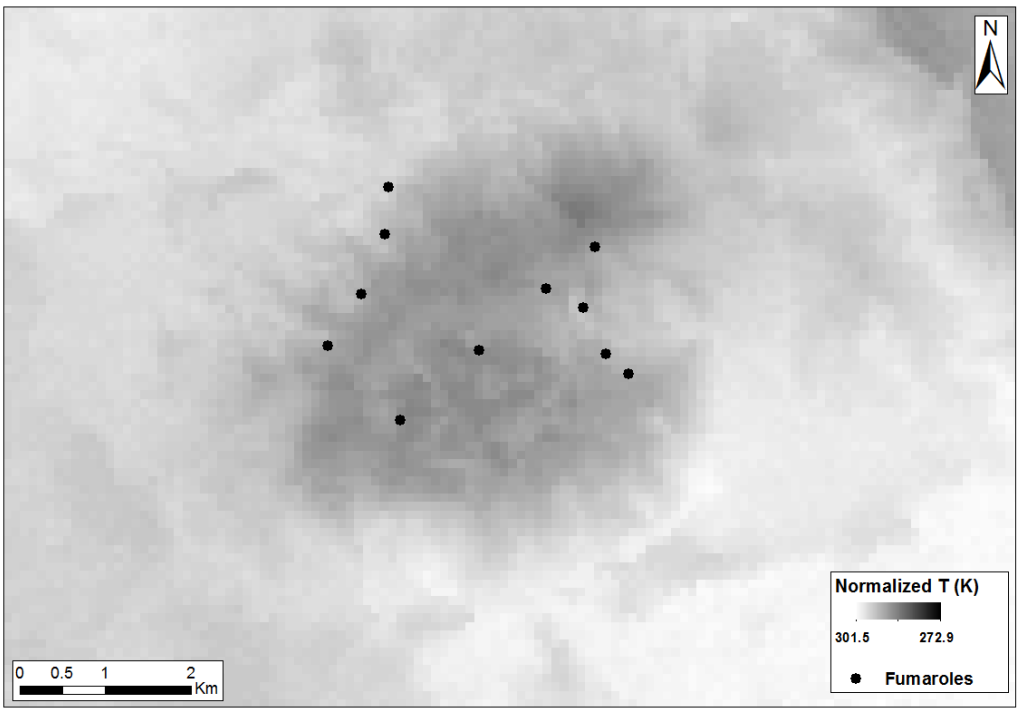

Figure 71. Normalized temperatures of the Alid center. Fumaroles coordinates have been plotted to highlight the correlation between anomalies and fumarolic steam.

Figure 71 shows a zoom of the top of Mt. Alid. Majority of thermal anomalies visible on the top of Alid seems to be linked with fumarolic activity, especially for Illegedi and the four on the northwestern flank. Because the good correlation between fumaroles and anomalies, it is unlikely that they can be interpreted as an effect of topography or insulation.

Despite the low image resolution, the high daily temperatures, which could affect the efficacy of this method, these results show the efficacy of this preliminary TIR analysis. Further detailed thermal investigation could give good results, useful for an the identification and the reconstruction of superficial manifestations of hydrothermal circulation network.

7. Conclusions

Considering the structural and geological setting, geothermal energy can represents one of the best options for the country to satisfy the increasing energetic demand and reduce carbon emissions, safeguarding the environment.

The principal aim of this work was to improve the characterization of Mt. Alid geothermal system (eastern Eritrea), considered the most favourable geothermal resource of the country.

After the height accuracy validation, the ALOS DEM has been fundamental in the process of the geological mapping, especially in a remote area like the northern part of the Afar Depression, where its 5 m cell size can be considered an high resolution topographic data. The combined use of DEMs, Landsat 8 data and aerial imagery has brought about the realization of an updated and more accurate geologic map of the Alid dome and surrounding area.

A decisive improvement in the interpretation of local structures, lithologies and geomorphologies has been achieved. The visual analysis of the drainage network has shown a fault-controlled fluvial system, helping the mapping of faults and structural lineaments, especially in the western scarp of the graben, where this tectonic control is more important.

The mapping of tectonic structures revealed two main tectonic elements: a NNW-SSE normal fault system, which is coherent with the regional trend and a NE-SW local fault system, which characterizes the Alid top. This local lineation seems to have a dextral strike slip component, as revealed by the deformation of fractures which cut the Alid dome. Moreover, the disposition of fumaroles appears related to the intersection of these two fault systems.

With the support of the processed multi-spectral images, the mapping of lithologies has brought about the definition of new rock classes, especially of different phases of basaltic effusions, characterized by two different topographic ruggedness indexes and previously mapped as a single phase eruption. Moreover the DEM analysis of the two basalt surfaces has confirmed the presence of two different topographic ruggedness indexes. A preliminary fieldwork, aimed to

check ground truths, was done in February 2015 and has confirmed the good coherence of the mapping.

The thermal normalization of ASTER TIR night images, despite the complexity of local topography and the high daily temperature, has revealed the presence of thermal anomalies which can be related shallow thermal manifestations such as fumaroles and has given us promising results for further advanced studies through TIR remote sensing. This preliminary analysis encourages further detailed studies.

Another interesting result obtained consists in the natural-state numerical model of the reservoir, achieved through a new interpretation of the available geological and geophysical data. Considering all the available data, and despite all the assumptions made to supply to the lack of information about hydraulic and thermal properties, the simulations showed extremely reasonable and realistic results, if compared to similar contexts within the EARS, with a reservoir temperature of 260-270 °C, a pressure of around 55 bar and a vapour fraction of 70% in the reservoir. Temperature-depth and pressure-depth curves obtained from the model has given a good match with the estimated values estimated fromy the geochemical and isotopic data.

In conclusion, the remote sensing approach has been shown to be a useful resource for the analysis of geological and structural morphologies, especially for places like the Eritrean Lowlands, where the arid climate and the logistics can be serious problems for the acquisition of geological information. Moreover, the high resolution DEM has brought to an improvement of new important structural data. The analysis of high resolution satellite data has given new information about the geological assessment and the geothermal system. However, this approach cannot replace the information provided by fieldwork campaigns and direct investigations, such as a detailed geological reconnaissance, geophysical surveys or deep exploration drilling.

At present, the advantage of geothermal energy exploitation should be considered a priority in the national energetic strategy of Eritrea. The exclusive dependence on imported oil makes the Eritrean power sector vulnerable to

increases in oil price. The low power generation capacity has further limited the spatial coverage and dependability of electrical service, denying almost all of the rural population access to cleaner energy and limiting opportunities for improving the living conditions of rural people. One major consequence of this situation is the reduction of the country's socio-economic development. Dependence on imported refined petroleum also causes environmental pollution.

These promising results can contribute to further exploration in the Alid volcanic field, which can be a serious opportunity for the socio-economic development of Eritrea and to improve the energetic sector of the country.

Acknowledgements

First of all, I want to thank my supervisor, Antonio Galgaro , who involved me in this interesting project and introduced me to geothermal energy. He also read and corrected my thesis during illness, causing his fever to get higher and higher. I owe him so much.

Many thanks goes to my co-supervisor, Andrea Ninfo, who provided help for the remote sensing analysis and for the writing of this thesis, providing fundamental correction, especially for the technical parts. He was for me an extraordinary co-supervisor.

Another thanks also goes to the CNR-IGG researchers Domenico Montanari and Giordano Montegrossi, who really helped me in the realization of the conceptual and numerical model. My days in Florence with them were very pleasant and challenging.

I want to thank Chiara Tognoli, who helped me to simulate the geothermal reservoir and with whom I spent a lot of time during my thesis. She is one of the best people I met in Padua as well one of my dearest friends. I hope to be the same for her.

Special thanks goes to the UNIPD members prof. Andrea Marzoli and Dr. Matteo Massironi, who gave me precious geological and structural information, as well as Dr. Massimiliano Ghinassi, who kindly shared with me a lot of information about the site area and provided a ground check.

I wish to thank Steve Owen for his extraordinary help. His correction were more than fundamental and I owe him all my progress in learning English. I want to consider you not only my teacher, but also a true friend. You'll miss me.

Many thanks also goes to my friends and colleagues in Padua. I spent two wonderful years in this beautiful city thanks to them, especially for Cristiano, Giorgio, Filippo, Tommaso, Ilaria, Michele, Pierre, Matteo…

One of my dearest friends, Riccardo, deserve special thanks. He spent a lot of time with me, preparing our exams, writing his thesis and so on. Our discussions about the ugliness of this world will be remembered forever (EEEEEEEEE).

Other special thanks goes to Elena, who was probably the best roommate I could desire. I wish here a beautiful life and a great success as geologist.

I wish to thank also my dear friend Ruben, who made me love his wonderful land. I hope to join him in Eritrea, one day, and discover its secrets.

A special thank also goes to Davide, who gave me motivation when my strength began to falter.

I can't forget my dear friends I left in Pavia, especially Andrea, Edoardo and Matteo. I left in Pavia a piece of my heart, as well as litres of my blood. I will never forget our three years together and I hope to see you more often.

A huge kiss goes to my beloved girlfriend, Elisabetta, who helped me every time I needed and gave me two special and unforgettable years. I only want to say that I truly love her.

Last but not least, I want to thank my family, who gave me life, education and love. If I can write this thesis it's only thanks to you. I can never really repay you and I will never forget what you taught to me: how to live an honest life.

References

Abrams, M., Hook, S., & Ramachandran, B. (2002). ASTER user handbook, version 2. Jet propulsion laboratory, 4800, 135.

Acocella, V. (2014). Structural control on magmatism along divergent and convergent plate boundaries: Overview, model, problems. Earth-Science Reviews, 136, 226-288.

Asmerom, Y. (1999). Th–U fractionation and mantle structure. Earth and Planetary Science Letters, 166(3), 163-175.

Bahati, G., & Natukunda, J. F. (2008). Status of geothermal exploration and development in Uganda. Short Course III on the Exploration of Geothermal Resources, 10.

Bahati, G., & Tuhumire J. (2002). Geothermal Energy in Uganda. Geological Survey of Uganda.

Baker, B. H., Mohr, P. A., & Williams, L. A. J. (1972). Geology of the eastern rift system of Africa. Geological Society of America Special Papers, 136, 1-68.

Barberi, F., Borsi, S., Ferrara, G., Marinelli, G., Santacroce, R., Tazieff, H., & Varet, J. (1972). Evolution of the Danakil depression (Afar, Ethiopia) in light of radiometric age determinations. The Journal of Geology, 720-729.

Barberi, F., Borsi, S., Ferrara, G., Marinelli, G., & Varet, J. (1970). Relations between tectonics and magmatology in the northern Danakil Depression (Ethiopia). Philosophical Transactions of the Royal Society of London. Series A, Mathematical and Physical Sciences, 267(1181), 293-311.

Barberi, F., & Varet, J. (1977). Volcanism of Afar: Small-scale plate tectonics implications. Geological Society of America Bulletin, 88(9), 1251-1266.

Barker, D. S. (1970). Compositions of granophyre, myrmekite, and graphic granite. Geological Society of America Bulletin, 81(11), 3339-3350.

Baker, B. T., & Wohlenberg, J. (1971). Structure and evolution of the Kenya Rift Valley. Nature, 229, 538-542.

Bosworth, W. (1985). Discussion on the structural evolution of extensional basin margins. Geological Society of London Journal 142, 939-942.
Bourdon, B., & Sims, K. W. (2003). U-series constraints on intraplate basaltic magmatism. Reviews in mineralogy and geochemistry, 52(1), 215-254.

Calais, E., d'Oreye, N., Albaric, J., Deschamps, A., Delvaux, D., Déverchere, J., Ebinger, C., Ferdinand, R. W., Kervyn, F., Macheyeki, A. S., Oyen, A., Perrot, J., Saria, E., Smets, B., Stamps, D. S., & Wauthier, C. (2008). Strain accommodation by slow slip and dyking in a youthful continental rift, East Africa. Nature, 456(7223), 783-787.

Campbell, J. B. (2011). Introduction to remote sensing - fifth edition. CRC Press, 716.

Chorowicz, J. (2005). The East African rift system. Journal of African Earth Sciences, 43(1), 379-410.

Chorowicz, J., Collet, B., Bonavia, F. F., Mohr, P., Parrot, J. F., & Korme, T. (1998). The Tana basin, Ethiopia: intra-plateau uplift, rifting and subsidence. Tectonophysics, 295(3), 351-367.

Chorowicz, J., Fournier, J. L., & Vidal, G. (1987). A model for rift development in Eastern Africa. Geological Journal, 22(S2), 495-513.

Clynne, M. A., Duffield, W. A., Fournier, R. O., & Janik, C. J. (1996). Geology and Geothermal Potential of Alid Volcanic Center, Eritrea, Africa (No. CONF-960913). Geothermal Resources Council, Davis, CA (United States), 279-285.
C.N.R.-C.N.R.S. (1973), Geology of northern Afar (Ethiopia). Revue de Geographic Physique et de Geologic Dynamique, v. 15, Fasc. 4, 443-490.

Corti, G. (2009). Continental rift evolution: from rift initiation to incipient break-up in the Main Ethiopian Rift, East Africa. Earth-Science Reviews, 96(1), 1-53.

D'Amore, F., & Panichi, C. (1980). Evaluation of deep temperatures of hydrothermal systems by a new gas geothermometer. Geochimica et Cosmochimica Acta, 44(3), 549-556.

Dainelli, G., & Marinelli, O. (1912). Risultati scientifici di un viaggio nella Colonia Eritrea. Tip. Galletti e Cocci, 601.

Drury, S. A., Kelley, S. P., Berhe, S. M., Collier, R. E., & Abraha, M. (1994). Structures related to Red Sea evolution in northern Eritrea. Tectonics, 13(6), 1371-1380.

Duffield, W. A., Bullen, T. D., Clynne, M. A., Fournier, R. O., Janik, C. J., Lanphere, M. A., Lowenstern, J., Smith J. G., Giorgis, L. W., Kahsai, G., Mariam, K. W., & Tesfai, T. (1996). Geothermal potential of the Alid volcanic center, Danakil Depression, Eritrea. US Department of the Interior, US Geological Survey, 68.

Ebinger, C. (2005). Continental break-up: the East African perspective. Astronomy & Geophysics, 46(2), 2-16.

Eysteinsson, H., Teklesenbet, A., Rosenkjær, G. K., & Karlsdottir, R. (2010). Resistivity Survey in the Alid Geothermal Area, Eritrea, a Joint Interpretation of TEM and MT Data. In Proceedings World Geothermal Congress 2010, Bali, Indonesia, 9.

Farr, T. G., Rosen, P. A., Caro, E., Crippen, R., Duren, R., Hensley, S., Kobrick, M., Paller, M., Rodriguez, E., Roth, L., Seal, D., Shaffer, S., Shimada, J., Umland, J., Werner, M., Oskin, M., Burbank, D., & Alsdorf, D. (2007). The Shuttle Radar Topography Mission. Reviews of geophysics, 45(2).

Fitch, F. J., Hooker, P. J., Miller, J. A., Mitchell, J. G., & Watkins, R. T. (1985). Reconnaissance potassium–argon geochronology of the Suregei–Asille district, northern Kenya. Geological Magazine, 122(06), 609-622.

Fujisada, H. (1994). Overview of ASTER instrument on EOS-AM1 platform. In SPIE's 1994 International Symposium on Optics, Imaging, and Instrumentation, International Society for Optics and Photonics, 14-36.

Habtetsion, S., & Tsighe, Z. (2007). Energy sector reform in Eritrea: initiatives and implications. Journal of Cleaner Production, 15(2), 178-189.

Hayward, N. J., & Ebinger, C. J. (1996). Variations in the along-axis segmentation of the Afar Rift system. Tectonics, 15(2), 244-257.

Hennig, T. A., Kretsch, J. L., Pessagno, C. J., Salamonowicz, P. H., & Stein, W. L. (2001). The shuttle radar topography mission. In Digital Earth Moving (pp. 65-77). Springer Berlin Heidelberg.

Hofmann, C., Courtillot, V., Feraud, G., Rochette, P., Yirgu, G., Ketefo, E., & Pik, R. (1997). Timing of the Ethiopian flood basalt event and implications for plume birth and global change. Nature, 389(6653), 838-841.

Hofstetter, R., & Beyth, M. (2003). The Afar Depression: interpretation of the 1960–2000 earthquakes. Geophysical Journal International, 155(2), 715-732.

Houssein, D. E., & Axelsson, G. (2010). Geothermal resources in the Asal Region, Republic of Djibouti: An update with emphasis on reservoir engineering studies. Geothermics, 39(3), 220-227.

Gersman, R., Ben-Dor, E., Beyth, M., Avigad, D., Abraha, M., & Kibreab, A. (2008). Mapping of hydrothermally altered rocks by the EO-1 Hyperion sensor, Northern Danakil Depression, Eritrea. International Journal of Remote Sensing, 29(13), 3911-3936.

Gibbs, A. D. (1990). Linked fault families in basin formation. Journal of Structural Geology 12 (5/6), 795-803.

Giggenbach, W. F., & Goguel, R. L., (1989). Collection and analysis of geothermal and volcanic water and gas discharges. Report No. CD1390, New Zealand Department of Scientific and Industrial Research, 81.

Gomarasca, M. A. (2009). Basics of geomatics. Springer Science & Business Media, 656.

Hochstein, M. P. (1999). Geothermal systems along the East-African Rift. Bulletin d'Hydrogiologie No. 17, 301-310.

Hughes, G. W., Varol, O., & Beydoun, Z. R. (1991). Evidence for Middle Oligocene rifting of the Gulf of Aden and for Late Oligocene rifting of the southern Red Sea. Marine and Petroleum Geology, 8(3), 354-358.

Irons, J. R., Dwyer, J. L., & Barsi, J. A. (2012). The next Landsat satellite: The Landsat data continuity mission. Remote Sensing of Environment, 122, 11-21.

Jalludin, M. (2010). State of knowledge of the geothermal provinces of the Republic of Djibouti. Short Course V on Exploration for Geothermal Resources" organized by UNUGTP, KenGen and GDC, Lake Naivasha, Kenya.

Kampunzu, A. B., & Mohr, P. (1991). Magmatic evolution and petrogenesis in the East African Rift System. In Magmatism in extensional structural settings (85-136). Springer Berlin Heidelberg.

Kebede, F., & Kulhánek, O. (1992). Recent seismicity of the East African rift system and its implications. Tectonophysics, 209(1), 51-54.

Keir, D., Ebinger, C. J., Stuart, G. W., Daly, E., & Ayele, A. (2006). Strain accommodation by magmatism and faulting as rifting proceeds to breakup: seismicity of the northern Ethiopian rift. Journal of Geophysical Research: Solid Earth (1978–2012), 111(B5).

Keller, G. R., Prodehl, C., Mechie, J., Fuchs, K., Khan, M. A., Maguire, P. K. H., Mooney, W. D., Achauer, U., Davies, P. M., Meyer, R. P., Braile, L. W., yambok, I. O., & Thompson, G. A. (1994). The East African rift system in the light of KRISP 90. Tectonophysics 236, 465-483.

Lowenstern, J. B., Charlier, B. L. A., Clynne, M. A., & Wooden, J. L. (2006). Extreme U–Th disequilibrium in rift-related basalts, rhyolites and granophyric granite and the timescale of rhyolite generation, intrusion and crystallization at Alid volcanic center, Eritrea. Journal of Petrology, 47(11), 2105-2122.

Lowenstern, J. B., Clynne, M. A., & Bullen, T. D. (1997). Comagmatic A-type granophyre and rhyolite from the Alid volcanic center, Eritrea, northeast Africa. Journal of Petrology, 38(12), 1707-1721.

Lowenstern, J. B., Janik, C. J., Fournier, R. O., Tesfai, T., Duffield, W. A., Clynne, M. A., Smith, J. G., Woldegiorgis, L., Weldermariam, K., & Kahsai, G. (1999). A geochemical reconnaissance of the Alid volcanic center and geothermal system, Danakil depression, Eritrea. Geothermics, 28(2), 161-187.

Marini, A. (1938). Il volcano Alid nella colonia Eritrea. L'Universo, volume 19, 51-65 and 131-170.

Matthew, M. W., Adler-Golden, S. M., Berk, A., Richtsmeier, S. C., Levine, R. Y., Bernstein, L. S., Acharya, P. K., Anderson, G. P., Felde, G. W., Hoke, M. P., Ratkowski, A., Burke, H. H., Kaiser R. D., & Miller, D. P. (2000). Status of atmospheric correction using a MODTRAN4-based algorithm. In AeroSense 2000, International Society for Optics and Photonics, 199-207

Mège, D., & Korme, T. (2004). Dyke swarm emplacement in the Ethiopian Large Igneous Province: not only a matter of stress. Journal of Volcanology and Geothermal Research, 132(4), 283-310.

Meyer, D. J., Tachikawa, T., Abrams, M., Tsu, H., Hato, M., Gesch, D. B., & Crippen, R. E. (2011). The ASTER Global Digital Elevation Model version 2.0-Early Validation Results. In AGU Fall Meeting Abstracts (Vol. 1, p. 1442).

Mohr, P. (1992). Nature of the crust beneath magmatically active continental rifts. Tectonophysics, 213(1), 269-284.

Mondeguer, A., Ravenne, C., Masse, P., & Tiercelin, J. J. (1989). Sedimentary basins in an extension and strike-slip background; the" South Tanganyika troughs complex", East African Rift. Bulletin de la Société géologique de France, (3), 501-522.

Mnjokava, T. T., Kabaka, K., & Mayalla, J. (2015). Geothermal Development in Tanzania–A Country Update. In Proceedings, World Geothermal Congress, 6.

Omenda, P. A. (2013). The geology and geothermal activity of the East African rift. Presented at Short Course VII on Exploration for Geothermal Resources, Lake Bogoria and Lake Naivasha, Kenya, Oct. 27 – Nov. 18, 2012, 18.

Omenda, P., & Simiyu, S. (2015). Country Update Report for Kenya 2010-2014. In Proceedings World Geothermal Congress 2015 (pp. 19-24).

Osawa, Y., Hiramatsu, M., & Ichida, K. (1998). PRISM: a panchromatic three-line sensor for mapping onboard ALOS. In Remote Sensing (pp. 173-180). International Society for Optics and Photonics.

Osawa, Y. (2004). Optical and Microwave Sensor on Japanese Mapping Satellite-ALOS. Photogrammetric Engineering and Remote Sensing, 35, 309-312.

Pickford, M. (1982). The tectonics, volcanics and sediments of the Nyanza Rift Valley, Kenya. Z. Geomorphol, 42, 1-33.

Pruess, K., & Narasimhan, T. N. (1982). On fluid reserves and the production of superheated steam from fractured, vapor-dominated geothermal reservoirs. Journal of Geophysical Research: Solid Earth , 87(B11), 9329-9339.

Reuter, D. C., Richardson, C. M., Pellerano, F. A., Irons, J. R., Allen, R. G., Anderson, M., Jhabvala, M. D., Lunsford, A. W., Montanaro, M., Smith, R. L., Tesfaye, Z., & Thome, K. J. (2015). The Thermal Infrared Sensor (TIRS) on Landsat 8: Design overview and pre-launch characterization. Remote Sensing, 7(1), 1135-1153.

Richards, J. A. (1999). Remote sensing digital image analysis (Vol. 3). Berlin et al.: Springer.

Riley, S. J., DeGloria, S. D., & Elliot, R. (1999). A terrain ruggedness index that quantifies topographic heterogeneity. intermountain Journal of sciences, 5(1-4), 23-27.

Rodriguez, E., Morris, C. S., & Belz, J. E. (2006). A global assessment of the SRTM performance. Photogrammetric Engineering & Remote Sensing, 72(3), 249-260.

Roy, D. P., Wulder, M. A., Loveland, T. R., Woodcock, C. E., Allen, R. G., Anderson, M. C., Helder, D., Irons, J. R., Johnson, D. M., Kennedy, R., Scambos, T. A., Schaaf, C. B., Schott, J. R., Sheng, Y., Vermote, E. F., Belward, A. S., Bindschadler, R., Cohen, W. B., Gao, F., Hipple, J. D., Hostert, P., Huntington, J., Justice, C. O., Kilic, A., Kovalskyy, V., Lee, Z. P., Lymburner, L., Masek, J. G., McCorkel, J., Shuai, Y., Trezza, R., Vogelmann, J., Wynne, R. H., & Zhu, Z. (2014). Landsat-8: Science and product vision for terrestrial global change research. Remote Sensing of Environment, 145, 154-172.

Scheidegger, A. E. (2004). Morphotectonics. Berlin etc: Springer.

Schilling, J. G. (1973). Afar mantle plume: rare earth evidence. Nature 242, 2-5.

Schilling, J. G., Kingsley, R., Hanan, B., & McCully, B. (1992). Nd-Sr-Pb isotopic variations along the Gulf of Aden: evidence for Afar mantle plume-continental lithosphere interaction. Journal of the Geophysical Research 97, 10927-10966.

Simiyu, S. M., & Keller, G. R. (1997). An integrated analysis of lithospheric structure across the East African plateau based on gravity anomalies and recent seismic studies. Tectonophysics, 278(1), 291-313.

Tachikawa, T., Hato, M., Kaku, M., & Iwasaki, A. (2011). Characteristics of ASTER GDEM version 2. In Geoscience and Remote Sensing Symposium (IGARSS), 2011 IEEE International (pp. 3657-3660). IEEE.

Tadono, T., Takaku, J., & Shimada, M. (2012). Validation study on ALOS prism DSM mosaic and aster GDEM 2. ISPRS Annals of Photogrammetry, Remote Sensing and Spatial Information Sciences, 1, 193-198.

Tognoli, C. (2014). Geothermal energy in Eritrea: feasibility analysis of the Alid district geothermal project. University of Padua, Master degree Thesis in Energetical Engineering, 178.

Teklemariam, M. (2012). Overview of geothermal resource exploration and development in East African Rift System. Short Course VII on Exploration for Geothermal Resources, UNU-GTP, GDC and KenGen, Kenya, Oct. 27 - Nov. 18, 2012.

Teklesenbet, A. (2012). Multidimensional inversion of MT data from Alid Geothermal area, Eritrea. Comparison with geological structures and identification of a geothermal reservoir, 120.

Teklesenbet, A. (2012). Multidimensional inversion of MT data from Alid Geothermal area, Eritrea; comparison with geological structures and identification of a geothermal reservoir. Reykjavik: Faculty of Earth Sciences, School of Engineering and Natural Sciences.

Tsend-Ayush, N. (2006). resistivity survey in the Hengill area, SW-Iceland.

UNDP (1973). Geology, Geochemistry and hydrology of the East Africa Rift System within Ethiopia. DDSF/ON/116, United Nations New York.

Yamaguchi, Y., Kahle, A. B., Tsu, H., Kawakami, T., & Pniel, M. (1998). Overview of advanced spaceborne thermal emission and reflection radiometer (ASTER). Geoscience and Remote Sensing, IEEE Transactions on, 36(4), 1062-1071.

Yohannes, E. (2015). Geothermal Exploration in Eritrea–Country Update. Proceedings World Geothermal Congress 2015 Melbourne, Australia, 19-25 April 2015.

Yohannes, E. (2010). Structural Significance of the Results of a Resistivity Study in Alid Geothermal Area. Proceedings World Geothermal Congress 2010, Bali, Indonesia, 25-29 April 2010.

Warner, T. A., & Chen, X. (2001). Normalization of Landsat thermal imagery for the effects of solar heating and topography. International Journal of Remote Sensing, 22(5), 773-788.

White, L. P. (1977). Aerial Photography and Remote Sensing for Soil Survey. Oxford, Clarendon Press, 104.

Wolfenden, E., Ebinger, C., Yirgu, G., Deino, A., & Ayalew, D. (2004). Evolution of the northern Main Ethiopian rift: birth of a triple junction. Earth and Planetary Science Letters, 224(1), 213-228.

Zumbo, V., Féraud, G., Vellutini, P., Piguet, P., & Vincent, J. (1995). First $^{40}Ar/^{39}Ar$ dating on early pliocene to plio-pleistocene magmatic events of the Afar-Republic of Djibouti. Journal of volcanology and geothermal research, 65(3), 281-295.

Appendix A

Hydraulic properties of Alid lithologies, resulting from the bibliographic research.

Litology	ρ(g/cm^3)			Source	φ [%]			Source	k (D)			Source	K(m/s)		Source
silt			1,74	Hamilon and Bachman (1982)	34	61	56,2	Hamilon and Bachman (1982)				Schon (2011)			
silt							47,5	Domenico&Schwartz						9,2533E-07	David Todd- Larry Mays
silt							46	David Todd- Larry Mays	0,001	0,1	0,0505	C.W. Fetter	0,00000001	5,05E-07	C.W. Fetter
silt					34	52	48,6	Kresic							
silt unconsolidated					35	50	42,5	Willis D.Weight					1E-09	0,00002	1,0001E-05	Willis D.Weight
silt unconsolidated			1,25	Manger USGS			53,2	Manger USGS							
Silt			**1,495**				**48,05**							**9,26E-07**	
Sandstone	2	2,8	2,4	Wohlenberg (1982)											
Sandstone	2,2	2,7	2,45	Blatt VDI (2010)											
Sandstone			2,64	Clauser 2011											
Sandstone			2,39	Manger USGS	4,5	22,2	10,1	Manger USGS							
Sandstone			2,55	Manger USGS	10,4	11,9	11,2	Manger USGS							
Sandstone					7,7	18,7	13,2	Manger USGS							
Sandstone					33	37	35	David Todd- Larry Mays					2,3148E-06	3,588E-05	1,3097E-05	David Todd- Larry Mays
Sandstone					0	54	16	Kresic							
Sandstone					3	25	15	Custodio- Llamas							
Sandstone					5	30	17,5	Domenico&Schwartz					0,005	1E-10	0,0025	Domenico&Schwartz
sandstone					5	30	17,5	Domenico&Schwartz					0,0025	0,00000005	0,00125003	Domenico&Schwartz
sandstone Ankr																
Sandstone	2,13	2,45	2,3	Manger USGS	8,6	17,3	13,3									
			2,29	Manger USGS	6,1	19,4	12,75	Manger USGS								
sandstone semiconsolidate							11	Heigh USGS								
Bunter Sandstone, GB, triassico				Schopper (1992)	5,8	30,8	18,3									
Bunter Sandstone, GB, triassico					5	35	20	Willis D.Weight					3E-10	0,000006	3,0002E-06	Domenico&Schwartz
bunter standstone			2,09	Manger USGS	5,8	30,8	20,4	Manger USGS								
Gray sandstone Ohio			2,129	Johnson USGS (1983)			20,74	Johnson USGS (1983)			0,013	Johnson USGS (1983)				
Red sandstone NY			2,492	Johnson usgs 1984			6,03	Johnson USGS (1983)			0,00000415	Johnson USGS (1983)				
Argillaceous sandstone			2,493	Johnson usgs 1985			7,7	Johnson USGS (1983)			0,000000915	Johnson USGS (1983)				
micaceous sandstone portland			2,14	Johnson usgs 1986			19,82	Johnson USGS (1983)			0,055	Johnson USGS (1983)				
brown sandstone NY			2,501	Johnson usgs 1987			6,54	Johnson USGS (1983)			0,00000205	Johnson USGS (1983)				
Banded sandstone			2,055	Johnson usgs 1988			23,46	Johnson USGS (1983)								
sandstone santa clara			2,16	Johnson usgs 1989			19,94	Johnson USGS (1983)			0,000926	Johnson USGS (1983)				
coconino sandstone ariz			2,401	Johnson usgs 1990			10,98	johnson USGS 1993			0,0000262	Johnson USGS (1983)				
Bromide formation					1	24	14	Manger USGS								
Blaylock sandstone			2,42	Manger USGS	2,3	17,4	7,3	Manger USGS								
Oriskany Sandstone				Manger USGS	7,1	9	8,3	Manger USGS								
Oriskany Sandstone			2,48	Manger USGS			6,6	Manger USGS								
Sandstone			**2,401**				**13,65**				**0,000505**			**0,000635**		

Appendix A (continued)

Lithology	ρ(gcm^3)			Source	φ [%]		Source	k [D]		Source	K [m/s]		Source
Siltstone	2,4												
Siltstone		2,6											
Siltstone			2,5	Blatt VDI (2010)							1E-11	1,4E-08	7,005E-09	Domenico&Schwartz
Siltstone													
siltstone					21	41							
Siltstone calif			2,119	Johnson usgs 1990			Domenico&Schwartz						
						31	Johnson USGS (1983)			Johnson usgs 1990			
Spraberry siltstone					0,5	19,6	21,34	0,00000455					
Bearpaw shale (siltstone)			1,57	Manger USGS			7,5						
claggat formation (siltstone)			1,81	Manger USGS			41,1						
Lebo shale formation (siltstone)			1,65	Manger USGS			36,3						
siltstone formation 1			1,91	Manger USGS			40,1						
siltstone formation 2			1,92	Manger USGS			26,2						
			1,91				29,8						
Siltstone	2,15	2,5	2,325	libro			Manger USGS						
Rhyolite			2,6	Blatt VDI (2010)									
Rhyolite					7	21	10,2						
Rhyolite Tuff			1,279				Kresic	0,034		Johnson USGS (1983)			
Rhyolite Castle rock			1,924				50,29	0,00029					
Rhyolite			2,125				23,44	0,017145					
Andesite	2,6	3,2	2,9	Blatt VDI (2010)			Johnson USGS (1983)						
Hornblende Andesite porphyry			2,732	Jonson USGS 1983			2,74	0,000000038		Johnson USGS (1983)			
Hornblende andesite			2,43	Jonson USGS 1983			8,47	0,000000065		Johnson USGS (1983)			
Andesite			2,732				5,605	5,15E-08					
Basalt	2,2	3,2	2,7	Sohon (2011)									
Basalt					3	35	19						2E-11
Basalt							Domenico&Schwartz						
Basalt					0	32,5	17						
Basalt					0,1	1	David Todd- Larry Mays						1,157 4E-07
Basalt dense					0,1	5	5,3				1E-11	1E-09	5,05E-10
Basalt dense monolithic							Kresic						
Basalt unfractured							Willis D.Weight						
Basalt permeable							Custodio- Llamas						
Basalt permeable	2,6	3,2	2,9	Blatt VDI (2010)				0,045	10^3	0,045	2E-11	0,00000042	2,100 1E-07
Basalt permeable			2,87	Clauser 2011									
Basalt permeable	2,463	2,945	2,795	Hyndman et al	1,7	24,5	7,8						
pillow lava (Basalt?)							1						
subaerial lava (Basalt?)							Hyndman et al						
vesicular haw aian basalts	0,049	3,06		Robertson and Peck 1974			Buttner et al (2003)	1E-06	10,133	5,06637E-08	Buttner et al (2003)		
Basalt vesicular					5	50	27,5			5,06636946			
Basalt vesicular					5	30	Willis D.Weight				1E-09	0,0000001	5,05E-08
Basalt fractured							12						
Basalt fractured							Custodio- Llamas						
Basalt fractured							10						
interlayered zoned							Willis D.Weight				1E-09	0,0000001	5,005E-06
young basalt							20				0,0000004	0,00001	1,0000002
Amygdaloidal basalt			2,764	Johnson USGS (1983)			Heigh USGS				0,00000011	5,055E-06	Willis D.Weight
Basalt chimney rock			2,93	Johnson USGS (1983)			11	0,0000616		Johnson USGS (1983)			
Olivine basalt			2,82	Johnson USGS (1983)			Johnson USGS (1983)	0,11e-6		Johnson USGS (1983)			
Basalt			**2,82**				**8,9**	0,0000021		Johnson USGS (1983)			
								0,0000616					**1,63E-07**

Appendix A (continued)

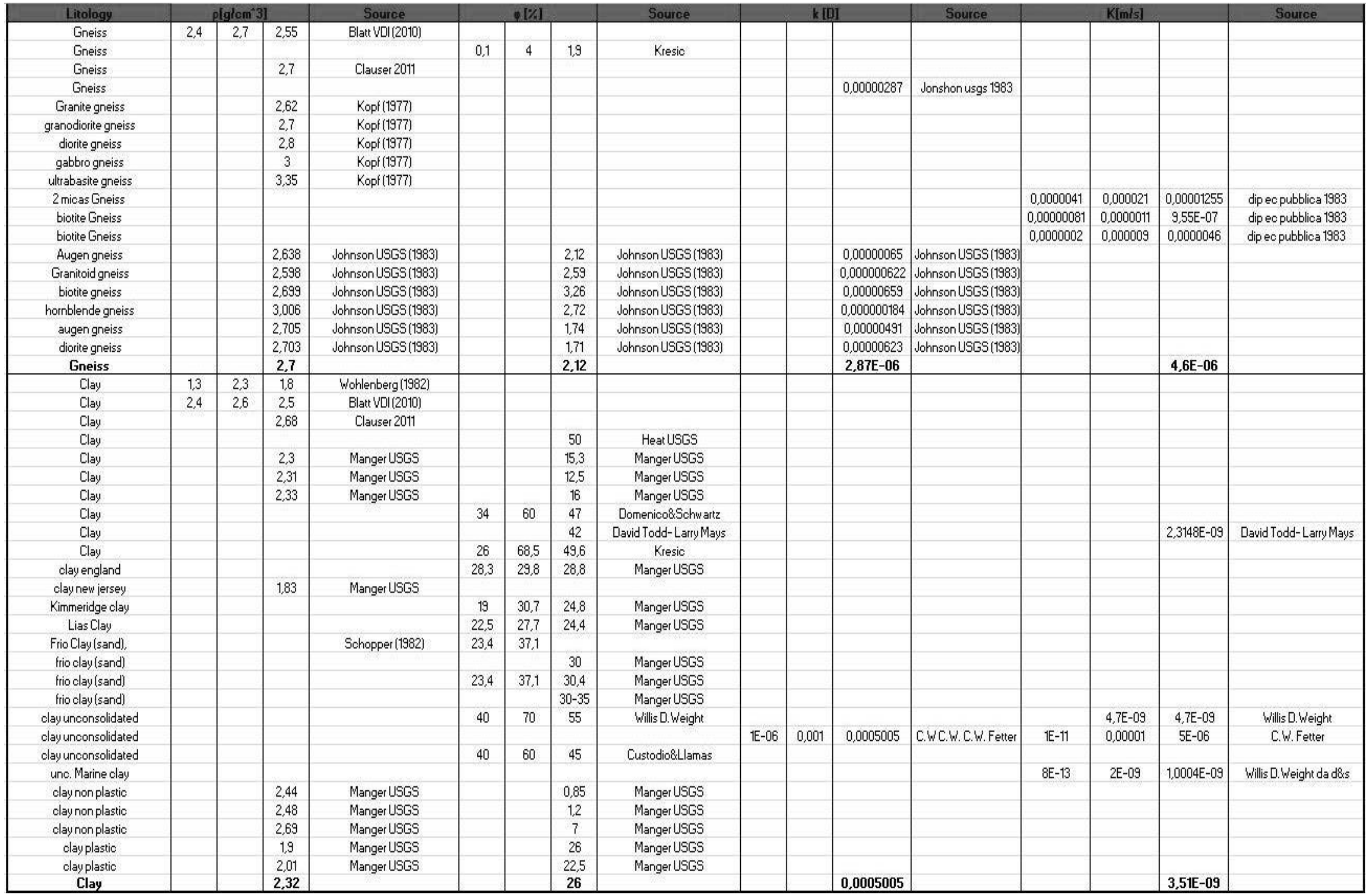

Litology	ρ[g/cm^3]			Source	φ [%]			Source	k [D]			Source	K[m/s]			Source
Gneiss	2,4	2,7	2,55	Blatt VDI (2010)												
Gneiss					0,1	4	1,9	Kresic								
Gneiss			2,7	Clauser 2011												
Gneiss											0,00000287	Jonshon usgs 1983				
Granite gneiss			2,62	Kopf (1977)												
granodiorite gneiss			2,7	Kopf (1977)												
diorite gneiss			2,8	Kopf (1977)												
gabbro gneiss			3	Kopf (1977)												
ultrabasite gneiss			3,35	Kopf (1977)												
2 micas Gneiss													0,0000041	0,000021	0,00001255	dip ec pubblica 1983
biotite Gneiss													0,00000081	0,0000011	9,55E-07	dip ec pubblica 1983
biotite Gneiss													0,0000002	0,000009	0,0000046	dip ec pubblica 1983
Augen gneiss			2,638	Johnson USGS (1983)			2,12	Johnson USGS (1983)			0,00000065	Johnson USGS (1983)				
Granitoid gneiss			2,598	Johnson USGS (1983)			2,59	Johnson USGS (1983)			0,000000622	Johnson USGS (1983)				
biotite gneiss			2,699	Johnson USGS (1983)			3,26	Johnson USGS (1983)			0,00000659	Johnson USGS (1983)				
hornblende gneiss			3,006	Johnson USGS (1983)			2,72	Johnson USGS (1983)			0,000000184	Johnson USGS (1983)				
augen gneiss			2,705	Johnson USGS (1983)			1,74	Johnson USGS (1983)			0,00000491	Johnson USGS (1983)				
diorite gneiss			2,703	Johnson USGS (1983)			1,71	Johnson USGS (1983)			0,00000623	Johnson USGS (1983)				
Gneiss			**2,7**				**2,12**				**2,87E-06**				**4,6E-06**	
Clay	1,3	2,3	1,8	Wohlenberg (1982)												
Clay	2,4	2,6	2,5	Blatt VDI (2010)												
Clay			2,68	Clauser 2011												
Clay							50	Heat USGS								
Clay			2,3	Manger USGS			15,3	Manger USGS								
Clay			2,31	Manger USGS			12,5	Manger USGS								
Clay			2,33	Manger USGS			16	Manger USGS								
Clay					34	60	47	Domenico&Schwartz								
Clay							42	David Todd- Larry Mays							2,3148E-09	David Todd- Larry Mays
Clay					26	68,5	49,6	Kresic								
clay england					28,3	29,8	28,8	Manger USGS								
clay new jersey			1,83	Manger USGS												
Kimmeridge clay					19	30,7	24,8	Manger USGS								
Lias Clay					22,5	27,7	24,4	Manger USGS								
Frio Clay (sand),				Schopper (1982)	23,4	37,1										
frio clay (sand)							30	Manger USGS								
frio clay (sand)					23,4	37,1	30,4	Manger USGS								
frio clay (sand)							30-35	Manger USGS								
clay unconsolidated					40	70	55	Willis D. Weight						4,7E-09	4,7E-09	Willis D. Weight
clay unconsolidated									1E-06	0,001	0,0005005	C.W C.W. C.W. Fetter	1E-11	0,00001	5E-06	C.W. Fetter
clay unconsolidated					40	60	45	Custodio&Llamas								
unc. Marine clay													8E-13	2E-09	1,0004E-09	Willis D. Weight da d&s
clay non plastic			2,44	Manger USGS			0,85	Manger USGS								
clay non plastic			2,48	Manger USGS			1,2	Manger USGS								
clay non plastic			2,69	Manger USGS			7	Manger USGS								
clay plastic			1,9	Manger USGS			26	Manger USGS								
clay plastic			2,01	Manger USGS			22,5	Manger USGS								
Clay			**2,32**				**26**				**0,0005005**				**3,51E-09**	

Appendix A (continued)

Lithology	ρ[g/cm^3]		Source	φ [v/v]		Source	k [D]		Source		Klin[-]		Source
Anhydrite			Schlumberger (1989)										
Anhydrite	2,8	3	Schlumberger (1989)										
Anhydrite	2,8	3	Hearst and Nelson (1985)										
Anhydrite			Gearhart (1978)										
Anhydrite	2,8	3	Blatt VDI (2010)										
Anhydrite										4E-13	0,00000002	1E-08	Willis D.Veight
Anhydrite				0,1	41	6,1			Kresic				
Anhydrite NV	2,87		Johnson USGS 1982			2,31			Johnson USGS (1983)				
Rock Anhydrite	2,936		Johnson USGS (1983)			0,74			Johnson USGS (1983)				
Anhydrite				0,5	5	2,75			Domenico&Schwartz	1E-13	1E-11	5,05E-12	Domenico&Schwartz
Anhydrite				0,5	5	2,75			Domenico&Schwartz	1E-14	1E-12	5,05E-13	Domenico&Schwartz
Anhydrite	**2,9**					**2,75**						**5,05E-12**	
Gypsum	2,32		Dortman (1976)										
Gypsum	2,2	2,35	2,275 Hearst and Nelson (1985)										
Gypsum	2,2	2,35	2,275 Gearhart (1978)										
Gypsum			2,32 Dortman (1976)										
Gypsum	2,2	2,4	2,3 Blatt VDI (2010)										
Gypsum			2,37 Clauser 2011										
Gypsum				1	30,5	8,7			Kresic				
Gypsum Utah			2,123 Johnson USGS (1983)			8,1			Johnson USGS (1983)				
Rock Gypsum			2,235 Johnson USGS 1984			5,78			Johnson USGS (1983)				
Gypsum			**2,288**			**8,1**							
micaschist	2,4	2,7	2,55 Blatt VDI (2010)	0	8,5	1,6							
quarzo micaSchist			2,779 Xiao et al 2011	5	15	2			Custodio-Llamas				
Schist GB			2,73 Manger USGS	1,2	2,3	1,8			Manger USGS				
Schist	2,77	2,9	2,835 Clauser 2011			1,31			Xiao et al (2011)				
hornblende schist			3,086 Johnson USGS (1983)			1,94			Johnson USGS (1983)				
glaucophane schist			3,073 Johnson USGS (1983)			5,42			Johnson USGS (1983)				
albite-muscovite schist			2,763 Johnson USGS (1983)			1,64			Johnson USGS (1983)				
vishnu schist			2,63 Jonshon USGS 1983			1,83			Johnson USGS (1983)				
Mica schist Manhattan			2,652 Jonshon USGS 1983			5,45			Johnson USGS (1983)				
Quarz sericite schist			2,64 Jonshon USGS 1983			3,23			Johnson USGS (1983)				
chlorite schist			2,704 Jonshon USGS 1983			1,21			Johnson USGS (1983)				
chlorite schist chester			2,921 Johnson USGS (1983)			3,69			Johnson USGS (1983)				
Schist			**2,747**			**1,94**						**2,31E-06**	
hyaloclastites	2,6	3,1	**2,85** Buttner 2003 (a spanne)			**12**	Buttner 2003						
Fractured igneous and met rocks							0,0001	5E+10	**7,09E-04**				
Fractured igneous and met rocks							0,0005	10	2500000000	8E-09	0,0003	0,00015	Willis D.Weight da d&s
fractured crystalline rocks				0	10	5	Domenico&Schwartz		5,00025 Freeze-Cherry	0,00000005	0,0001	5,0025E-05	Freeze-Cherry
dense cryst rocks				0	5	2,5	Domenico&Schwartz			3E-14	0,00000002	1E-08	Willis D.Weight da d&s
unfractured ig&met rocks									2,50005E-05 Freeze-Cherry	1E-14	1E-10	5,0005E-11	Freeze-Cherry
unfractured ig&met rocks							1E-09	5E-05					
Pumice Utah			0,852 Johnson USGS (1983)	50	72,44	Johnson USGS (1983)			0,14 Johnson USGS (1983)				
Pumice				90	85	Custodio&Llamas							
Pumice				75	75								
Pumice Calif			0,433 Johnson USGS (1983)		81,63	Johnson USGS (1983)			12,2 Johnson USGS (1983)				
Pumice			**0,543**		**75**				**6,17**				

Appendix B

Thermal properties of Alid lithologies, resulting from the bibliographic research.

Lithology	SCHON			CERMAK & RYBACH, 1982			JESSOP, 1990			DORTMAN, 1976			BLACKWELL & STEELE, 1989			KOBRANOVA, 1989			DORTMAN-KOBRANOVA		
	Min	Max	Mean	Min	Max	Mean	Min	Max	Mean	Min	Max	Mean	Min	Max	Mean	Min	Max	Mean	Min	Max	Mean
Greanite, syenite	2	4,5		1,25	4,45	3,05	2,3	3,6	3,43	1,34	3,69	2,4				1,12	3,85				
Gneiss, Schist	1,5	5																			
Sandstone	1,5	6		0,9	6,5	2,47	1,88	4,98	3,72				2,5	4,2		0,67	6,49		0,38	5,17	1,66
Argillite				0,8	3,7	2,09										1,1	7,41		0,25	3,01	1,21
Clay				0,6	2,6	1,53													0,38	3,02	1,49
Siltstone	1,5	4		2,47	2,84	2,68															
Riolite																					
Andesite				1,55	4,65	3,2	1,35	4,86	2,26							1,42	2,79				
Basalt				1,4	5,33	1,95	1,12	2,38	1,69	0,51	2,03	1,45				0,44	3,49				
Subaerial lava																					
Subaerial high perm																					
Subaerial low perm																					
Pillow lava																					
Low perm. Pillow																					
Hyaloclastite																					
Pumix																0,25					
																0,5					
Lava				0,2	4,6	2,5													0,25	0,73	0,49
Gneiss				1,16	4,75	2,44															
a perpendicular				1,2a	2,6a	2,74															
b parallel				1,2b	3,1b	2,12															
Gneiss e Micaschist										0,94	4,86	2,02									
a perpendicular												2,77a									
b parallel												3,61b									
a perpendicular												2,31a									
b parallel												1,30b									
Schist			1	5,2	3,14				1,03	4,93	2,46					0,65	4,76				
a perpendicular			1,0a	3,1a	2,05																
b parallel			1,7b	4,1b	2,88																
Anhydrite			1	6,05	4	4,89	5,73	5,43	4,9	5,75		4,9	5,8		2,5	5,8					
Gypsum																0,6	1,67				

Appendix B (continued)

Lithology	WENK & WENK, 1969			RICHARDSON ET AL., 197			BUTTNER ET AL., 2003			HORAI, 1991			HYNDMAN ET AL., 2007			VDI BLATT, 2010			YASAR ET AL., 2008			MEDIAN VALUE
	Min	Max	Mean	Min	Max	Mean	Min	Max	Mean	Min	Max	Mean	Min	Max	Mean	Min	Max	Mean	Min	Max	Mean	
Granite, syenite																1,1	3,4	2,2				3,05
Gneiss, Schist																3,1	3,4	3,3				2,54
Sandstone																1,3	2,3	1,7			0,64	4,9
Clay																1,3	2,3	1,7			0,72	2,5
Siltstone																1,1	3,4	2,2			0,59/0,63	1,51
Riolite																3,1	3,4	3,3				2,335
Andesite																1,3	2,3	1,7				3,3
Basalt																1,3	2,3	1,7			2,34	4,9
Subaerial lava									1,87	Maxwell formula		1,47	DSDP leg 37 basalt		1,66						1,74	1,87
Subaerial high perm									1,87	Fricke-Zimmermann		1,77	DSDP leg 26 basalt		1,54						1,45	
Subaerial low perm									1,87			1,82										
Pillow lava									2	Schulz		1,82										
Low perm. Pillow									2			1,82									0,25	
Hyaloclastite									1,8													1,8
Pumix																						0,25
Lava																						
Gneiss																1,9	4	2,9				2,44
a perpendicular																						
b parallel																						
Gneiss e Micaschist																						2,54
a perpendicular			2,05a																			
b parallel			2,88b																			
a perpendicular						2,86a																
b parallel						3,84b																
Schist															3	1,5	3,1	2,2				3
a perpendicular																						
b parallel																						
Anhydrite																1,5	7,7	4,1				4,9
Gypsum																1,3	2,8	1,6				1,6

Appendix B (continued)

Lithology	CERMAK & RYBACH, 1982			DORTMAN, 1976			KOBRANOVA, 1989			DORTMAN-KOBRANOVA			WAPLES & WAPLES, PETRUNIN ET AL., 2011			MEDIAN VALUE
	Min	Max	Mean	Min	Max	Mean	Min	Max	Mean	Min	Max	Mean	Min	Max	Mean	
Granite, syenite	0,670	1,550	0,958	0,74	1,55	0,946	0,25	1,55					0,6	1172,000		0,952
Gneiss, Schist													0,77	0,979		0,870
Sandstone	0,750	3,350	1,64							0,67	3,35	0,97			0,775	1,305
Siltstone																
Shale										0,74	0,99	0,87				0,870
Andesite							0,81	0,82								0,815
Basalt	0,880	0,890		0,76	2,14	1,23	0,54	0,82					0,88	0,9		0,880
Pumix																
Lava	0,670	1,380	1,08							0,67	1,38	1,12				
Gneiss	0,460	0,920	0,75	0,75	1,18	0,979							0,79	1,096		0,835
Schist	0,670	1,500	0,8	0,75	1,73	1,096	0,7	1,64					0,59	0,94		0,948
Anhydrite	0,810	0,940	0,98				0,58	0,61							1,010	0,810
Gypsum							0,9	1,1								1,000

Appendix C

Location and elevation of the TEM soundings, assumed as GCPs, and height differences between points DEMs and points.

	TEM SOUNDINGS										
	UTM COORDINATES (m)		HEIGHTS (m)								
	X	Y	Z GCPs	Z DSM	Z SRTM	Z GDEM	Z ERITREA	DSM-GCPs	SRTM-GCPs	GDEM-GCPs	ERITREA-GCPs
ALI001	593004	1643999	163	171	173	150	185	8	10	-13	22
ALI002	592992	1645003	152	156	158	149	171	4	6	-3	19
ALI003	593016	1645982	140	143	145	127	162	3	5	-13	22
ALI004	594056	1642001	218	240	212	226	219	22	-6	8	1
ALI005	593980	1643000	227	214	206	213	192	-13	-21	-14	-35
ALI006	593980	1643988	178	181	184	166	190	3	6	-12	12
ALI007	593996	1645003	165	166	172	133	186	1	7	-32	21
ALI008	593998	1646005	157	157	160	143	185	0	3	-14	28
ALI009	593948	1646857	155	156	159	130	192	1	4	-25	37
ALI010	595008	1641001	174	180	181	182	193	6	7	8	19
ALI011	595008	1641987	148	176	177	165	204	28	29	17	56
ALI012	595012	1643005	232	236	235	222	342	4	3	-10	110
ALI013	594988	1644013	237	253	248	246	320	16	11	9	83
ALI014	594840	1645050	217	224	223	224	300	7	6	7	83
ALI015	594964	1645995	202	204	206	206	256	2	4	4	54
ALI016	594944	1646992	195	195	199	175	206	0	4	-20	11
ALI018	596000	1640000	165	169	170	169	179	4	5	4	14
ALI019	596012	1641014	166	170	165	166	179	4	-1	0	13
ALI020	596000	1642007	176	196	191	167	256	20	15	-9	80
ALI022	595704	1645939	244	243	261	236	356	-1	17	-8	112
ALI023	595932	1646963	204	206	213	191	188	2	9	-13	-16
ALI026	596936	1639915	163	159	160	151	170	-4	-3	-12	7
ALI027	596960	1640712	167	172	176	156	168	5	9	-11	1
ALI028	596972	1641885	188	189	186	176	193	1	-2	-12	5
ALI029	597528	1644206	560	570	575	554	703	10	15	-6	143
ALI030	596752	1643806	651	654	658	657	696	3	7	6	45
ALI031	597080	1646798	218	214	216	214	280	-4	-2	-4	62
ALI035	597976	1640002	166	162	154	146	166	-4	-12	-20	0
ALI036	597993	1640984	124	130	129	108	159	6	5	-16	35
ALI037	598058	1641808	115	127	127	102	184	12	12	-13	69
ALI038	598356	1644156	619	608	622	621	678	-11	3	2	59
ALI039	598432	1644983	587	599	594	589	709	12	7	2	122
ALI040	597644	1644986	595	596	602	592	754	1	7	-3	159
ALI046	599004	1641873	134	134	131	118	155	0	-3	-16	21
ALI047	599192	1644217	618	603	621	584	646	-15	3	-34	28
ALI048	599176	1645008	597	602	595	598	585	5	-2	1	-12
ALI054	599968	1641947	117	108	107	92	147	-9	-10	-25	30
ALI060	600868	1642173	71	78	80	61	137	7	9	-10	66
ALI061	601116	1642980	76	85	81	91	151	9	5	15	75
ALI068	602012	1643015	82	87	88	59	133	5	6	-23	51
ALI069	601992	1643995	122	121	123	96	157	-1	1	-26	35
ALI074	593008	1642994	190	200	210	208	198	10	20	18	8
ALI075	603040	1643913	86	84	83	70	156	-2	-3	-16	70
ALI076	603000	1643000	79	72	76	40	135	-7	-3	-39	56
ALI077	592000	1645001	161	157	161	168	173	-4	0	7	12
ALI078	591016	1645015	181	180	183	192	176	-1	2	11	-5
ALI079	589996	1645093	197	196	194	192	197	-1	-3	-5	0
ALI080	589160	1645264	190	186	192	170	196	-4	2	-20	6
ALI081	588004	1645579	214	221	222	210	255	7	8	-4	41
ALI082	591984	1646019	163	157	160	130	164	-6	-3	-33	1
ALI083	596964	1638991	160	156	156	128	170	-4	-4	-32	10
ALI084	597632	1637979	150	147	146	135	156	-3	-4	-15	6
ALI085	598456	1637024	106	104	109	92	162	-2	3	-14	56
ALI086	599028	1636086	103	99	104	88	87	-4	1	-15	-16
ALI088	600712	1634086	62	n.a.	67	37	68	n.a.	5	-25	6
ALI089	601012	1633080	53	n.a.	45	-1	52	n.a.	-8	-54	-1
ALI090	601528	1631624	20	n.a.	17	13	-5	n.a.	-3	-7	-25
ALI091	591172	1647070	138	139	144	111	160	1	6	-27	22
ALI092	590424	1648286	122	123	125	117	145	1	3	-5	23
ALI093	589716	1649497	118	123	127	113	141	5	9	-5	23
ALI094	589048	1650805	115	113	117	103	123	-2	2	-12	8
ALI095	594028	1640794	220	221	215	206	216	1	-5	-14	-4
ALI097	592992	1641935	260	256	252	250	233	-4	-8	-10	-27
ALI098	593024	1640863	218	218	238	220	243	0	20	2	25
ALI099	595028	1639880	182	182	184	182	193	0	2	0	11
ALI101	588480	1651899	83	94	96	81	100	11	13	-2	17

Appendix D

Location and elevation of MT soundings, assumed as GCPs, and height differences between DEMs and points

	MT SOUNDINGS										
	UTM COORDINATES		HEIGHTS (m)								
	X	Y	Z GCPs	Z DSM	Z SRTM	Z GDEM	Z ERITREA	DSM-GCPs	SRTM-GCPs	GDEM-GCPs	ERITREA-GCPs
013	592980	1643986	169	170	174	151	185	1	5	-18	16
002	593044	1645028	156	156	158	147	171	0	2	-9	15
003	593016	1645989	140	142	145	127	162	2	5	-13	22
004	593920	1641977	203	208	211	206	218	5	8	3	15
005	594128	1642847	204	203	208	208	215	-1	4	4	11
006	594076	1644055	194	191	183	182	192	-3	-11	-12	-2
007	593996	1645001	167	165	172	133	186	-2	5	-34	19
008	593992	1646002	156	158	158	143	185	2	2	-13	29
009	594084	1646679	155	153	155	143	194	-2	0	-12	39
010	595000	1640979	175	180	182	171	194	5	7	-4	19
011	595064	1642000	175	176	179	154	214	1	4	-21	39
012	594852	1643093	228	228	231	230	327	0	3	2	99
001	594876	1643947	250	251	248	243	300	1	-2	-7	50
014	594956	1644986	219	228	231	226	331	9	12	7	112
015	595008	1646000	200	206	211	199	265	6	11	-1	65
016	594896	1646940	195	196	199	177	208	1	4	-18	13
018	596004	1639969	165	170	169	170	179	5	4	5	14
019	595936	1641004	167	171	169	167	180	4	2	0	13
020	595988	1641914	177	172	181	159	240	-5	4	-18	63
022	595720	1645972	245	246	261	232	353	1	16	-13	108
023	595888	1646898	205	208	210	185	194	3	5	-20	-11
026	596700	1639837	162	160	165	130	172	-2	3	-32	10
027	596872	1640956	165	168	171	144	169	3	6	-21	4
028	597020	1641866	188	186	185	153	193	-2	-3	-35	5
029	597468	1644274	570	569	585	567	706	-1	15	-3	136
030	596716	1643831	651	652	652	650	680	1	1	-1	29
031	597072	1646813	209	213	216	214	240	4	7	5	31
035	598036	1639965	156	158	157	154	168	2	1	-2	12
036	597828	1640975	130	127	139	102	159	-3	9	-28	29
037	597988	1641941	123	131	133	117	191	8	10	-6	68
038	598328	1644259	603	605	616	585	680	2	13	-18	77
039	598416	1644926	589	591	594	578	705	2	5	-11	116
040	597612	1644797	573	575	577	560	728	2	4	-13	155
046	599132	1641991	122	120	122	130	164	-2	0	8	42
047	599200	1644229	601	603	621	584	646	2	20	-17	45
048	599080	1645006	597	598	596	589	600	1	-1	-8	3
054	600024	1641974	108	107	107	79	148	-1	-1	-29	40
060	600916	1642232	80	79	78	62	137	-1	-2	-18	57
061	601012	1642900	90	81	81	90	153	-9	-9	0	63
068	601992	1643045	86	89	88	67	133	3	2	-19	47
069	602040	1643933	114	116	123	94	156	2	9	-20	42
074	592972	1643055	190	190	196	201	197	0	6	11	7
076	603024	1643013	71	74	70	41	135	3	-1	-30	64
077	591984	1644956	161	158	161	165	174	-3	0	4	13
078	590984	1644964	187	182	183	192	177	-5	-4	5	-10
079	590012	1645096	198	195	194	192	197	-3	-4	-6	-1
080	589132	1645262	183	185	198	171	200	2	15	-12	17
081	588076	1645792	194	196	198	191	240	2	4	-3	46
084	597564	1637957	146	145	146	135	155	-1	0	-11	9
085	598520	1637005	103	103	105	93	160	0	2	-10	57
000	601464	1631600	27		25	13	-5	n.a.	-2	-14	-32

Appendix E

Geological map of the Alid geothermal area